

Compositional Engineering and Post-treatment of Caesium-based Halide Perovskite Materials for Perovskite Solar Cells



A dissertation submitted to the Department of Chemistry, Quaid-i-Azam University, Islamabad, in partial fulfillment of the requirements for the degree of

Doctor of Philosophy

in

Analytical /Inorganic Chemistry

By

Kalsoom Fatima

**Department of Chemistry
Quaid-i-Azam University Islamabad,
Pakistan**

2024

Compositional Engineering and Post-treatment of Caesium-based Halide Perovskite Materials for Perovskite Solar Cells



Submitted by:

Kalsoom Fatima

Supervised by:

Prof. Dr. Zareen Akhter

**Department of Chemistry
Quaid-i-Azam University Islamabad
Pakistan
2024**



*In the Name of Allah,
the Most Gracious and the
Most Merciful*





Dedicated to,

*my Beloved Parents and Esteemed
Teachers*

*Whose prayers and unwavering support not only provide
me with strength but also serve as a symbol of success
for my future endeavors.*

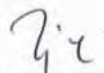
May ALLAH Almighty bless them. Ameen!!



DECLARATION

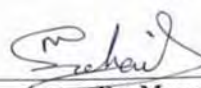
This is to certify that this dissertation entitled "*Compositional Engineering and Post-treatment of Caesium-based Halide Perovskite Materials for Perovskite Solar Cells*" submitted by *Ms. Kalsoom Fatima*, is accepted in its present form by the Department of Chemistry, Quaid-i-Azam University, Islamabad, Pakistan, as satisfying the partial requirement for the award of degree of *Doctor of Philosophy in Inorganic/Analytical Chemistry*.

External Examiner (I):



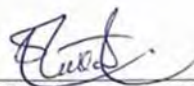
Prof. Dr. Tariq Yasin
Registrar
Pakistan Institute of Engineering &
Applied Sciences, P.O Nilore
Islamabad

External Examiner (II):



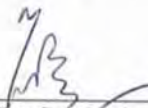
Dr. Manzar Sohail
Professor
SNS, NUST
H-12 Islamabad

Co-Supervisor :



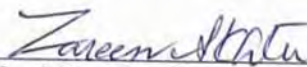
Prof. Dr. Muhammad Sultan
Pro Vice Chancellor
Kohsar University Murree.

Head of Section:



Prof. Dr. Syed Munir Hussain Shah
Department of Chemistry
Quaid-i-Azam University
Islamabad.

Supervisor & Chairman:



Prof. Dr. Mrs. Zareen Akhter
Department of Chemistry
Quaid-i-Azam University
Islamabad.

Certificate of Approval

This is to certify that the research work presented in this thesis, entitled "Compositional Engineering and Post-treatment of Caesium-based Halide Perovskite Materials for Perovskite Solar Cells" was conducted by Ms. Kalsoom Fatima under the supervision of Prof. Dr. Mrs. Zareen Akhter

No part of this thesis has been submitted anywhere else for any other degree. This thesis, is submitted to the Department of Chemistry Quaid-i-Azam University Islamabad in partial fulfillment of the requirements for the Doctor of Philosophy in Field of Analytical/Inorganic Chemistry, Department of Chemistry, Quaid-i-Azam University, Islamabad.

Student Name Ms. Kalsoom Fatima Signature: KHif

Examination Committee:

1. External Examiner: **Prof. Dr. Tariq Yasin** Signature: Tariq
Registrar
Pakistan Institute of Engineering &
Applied Sciences, P.O. Nilore
Islamabad.

2. External Examiner: **Dr. Manzar Sohail** Signature: Manzar Sohail
Professor
SNS, NUST
H-12 Islamabad

3. Internal Examiner: **Prof. Dr. Syed Munir Hussain Shah** Signature: Syed Munir Hussain Shah
Department of Chemistry
Quaid-i-Azam University
Islamabad.

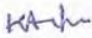
Co-Supervisor: **Prof. Dr. Muhammad Sultan** Signature: Muhammad Sultan

Supervisor & Head of Department: **Prof. Dr. Zareen Akhter** Signature: Zareen Akhter

AUTHOR'S DECLARATION

I, Ms. Kalsoom Fatima hereby state that my Ph.D. thesis titled "Compositional Engineering and Post-treatment of Caesium-based Halide Perovskite Materials for Perovskite Solar Cells" is my own work and has not been submitted previously by me for taking any degree from this University (Quaid-i-Azam University Islamabad) or anywhere else in the country/world.

At anytime if my statement is found to be incorrect even after my Graduation the University has the right to withdraw my Ph.D. degree.


Name of student: Ms. Kalsoom Fatima

PLAGIARISM UNDERTAKING

I solemnly declare that, the research work presented in the thesis titled "Compositional Engineering and Post-treatment of Caesium-based Halide Perovskite Materials for Perovskite Solar Cells" is solely my research work with no significant contribution from any other person. Small contribution/help wherever taken has been duly acknowledged and that complete thesis has been written by me.

I understand the zero tolerance policy of the HEC and Quaid-i-Azam University Islamabad towards plagiarism. Therefore, I as an Author of the above titled thesis declare that no portion of my thesis has been plagiarized and any material used as reference is properly referred/cited.

I undertake that if I am found guilty of any formal plagiarism in the above titled thesis even after award of Ph.D. degree, the university reserves the rights to withdraw/revoke my Ph.D. degree and that HEC and the University has the right to publish my name on the HEC/University website on which names of students are placed who submitted plagiarized thesis.

Student/Author Signature: KAifun

Name: Ms. Kalsoom Fatima

PhD thesis Evaluation by Foreign Examiners

This thesis was evaluated by following foreign examiners:

1. A/Prof. John A. Stride

School of Chemistry

University of New South Wales,

Sydney, Australia

2. Professor Sheng Dai

School of Chemical and processing Engineering

University of Leeds, UK

List of Publications from this Thesis

1. **Fatima, Kalsoom,** Muhammad Irfan Haider, Azhar Fakharuddin, Zareen Akhter, Muhammad Sultan, and Lukas Schmidt-Mende. "Performance enhancement of CsPbI₂Br perovskite solar cells via stoichiometric control and interface engineering." *Solar Energy* 211 (2020): 654-660.
2. **Fatima, Kalsoom,** Muhammad Irfan Haider, Amna Bashir, Samina Qamar, Akbar Ali Qureshi, Zareen Akhter, and Muhammad Sultan. "Surface modification of CsPbI₂Br for improved performance of inorganic perovskite solar cells." *Physica E: Low-dimensional Systems and Nanostructures* 142 (2022): 115265.

Acknowledgments

My first and foremost thanks to **Almighty Allah** the most beneficent and the most merciful without his blessing it would have been impossible for me to complete this dissertation. Peace and blessings of Allah be upon **His Prophet Muhammad (P.B.U.H)** who guided mankind to the path of rightness, who is the true source of wisdom and knowledge.

I would like to express my heartfelt appreciation to my esteemed and respected supervisor, **Prof. Dr. Zareen Akhter**, Chairman Department of Chemistry, **Quaid-i-Azam University Islamabad Pakistan**, whose invaluable guidance, constant encouragement and generous cooperation motivated me to work diligently to accomplish my goals. I am also obliged to her for providing me research facilities and conducive environment in the department. I am sincerely grateful to my co-supervisor **Prof. Dr. Muhammad Sultan**, Kohsar University Murree, for his guidance at each step of my research. Due to his support and cooperation, I was able to complete my research work. I am also grateful to all my teachers who have played a fundamental role in my educational journey. They are the strong pillars upon which my academic foundation stands.

I am highly thankful to **Prof. Dr. Lukas Schmidt Mende** University of Konstanz, Germany, for his cooperation, support and research facilities. I also express my sincere gratitude to **Prof. Dr. Joe Briscoe**, Queen Mary University of London UK, for his encouragement, lab facilities, valuable time and suggestions. A special thanks to my colleagues at the University of Konstanz, Germany and Queen Mary University of London for their cooperation and help. I am grateful to DAAD Germany and the Higher Education Commission of Pakistan for providing me financial support for my visit to the University of Konstanz, Germany and Queen Mary University of London, UK.

I owe my deepest gratitude to my lab fellows especially **Samina Qamar** for their support during my research work. The time spent in the company of these people has become a memorable part of my life. I would like to apprehend the cooperation of all employees of the Department of Chemistry.

A special thanks to my friends **Aalia Manzoor** and **Umama Bint-e-Irshad** for their pleasant company, unconditional support and caring attitude which made my journey more pleasant, memorable and fruitful.

Last, but not the least, my heartiest gratitude and appreciation goes to my unconditionally loving family. I am most indebted to my father **Muhammad Shafiq Jaral**, and my mother **Nasreen Akhter**, for their endless prayers, matchless love and care. Words become meaningless when I have to say thanks to my parents; their prayers gave me strength and hope to accomplish this task and pursue my goals.

Kalsoom Fatima

kalsoomfatima@chem.qau.edu.pk

Table of Contents

Index of Figures	xviii
Index of Tables	xxiii
List of Abbreviations	xxiv
Abstract	xxvi
1. Introduction	1
1.1. Renewables as a Source of Sustainable Energy	1
1.1.1. The Sun and Solar Radiations	2
1.2. Solar Photovoltaic	3
1.2.1. Evolution of Solar Cells	3
1.2.1.1. First-Generation Solar Cells	3
1.2.1.2. Second-Generation Solar Cells	4
1.2.1.3. Third-Generation Solar Cells	5
1.3. Origin of Perovskite Semiconductor	6
1.3.1. Benign Properties of Perovskite Semiconductors	9
1.3.1.1. High Absorption Coefficient and Small Urbach Energy	9
1.3.1.2. Long Charge Carrier Diffusion Length.....	9
1.3.1.3. Unique Defects Physics	10
1.3.1.4. Low Costs	10
1.3.2. Perovskite Film Deposition Techniques.....	10
1.3.2.1. One-Step Deposition.....	11
1.3.2.2. Two-Step Deposition	11
1.3.2.3. In-Situ Dipping Method.....	12
1.3.2.4. Vapor-Assisted Deposition.....	12
1.4. PSCs Architectures:.....	12
1.4.1. Mesoporous Architecture	13
1.4.2. Planar Architecture	14
1.4.3. Charge Transport Materials	14
1.4.3.1. Hole Transport Materials (HTMs)	14
1.4.3.2. Electron Transport Materials (ETMs).....	14
1.5. Working Principle of Perovskite Solar Cells	16
1.5.1. Charge Generation	17
1.5.2. Charge Transport and Recombination.....	17

1.5.3. Charge Extraction	18
1.6. Solar Cell Characteristic Parameters	18
1.6.1. Open Circuit Voltage (V_{OC})	19
1.6.2. Short Circuit Current (I_{SC})	19
1.6.3. Maximum Power Point (P_{max})	20
1.6.4. Fill Factor (FF)	20
1.6.5. Power Conversion Efficiency (PCE)	20
1.6.6. Incident Photon Conversion Efficiency (IPCE)	21
1.6.7. Series Resistance (R_S)	21
1.6.8. Shunt Resistance (R_{sh})	21
1.7. Inorganic Caesium Lead Halide Perovskites for PSCs	22
1.8. Properties of Caesium Lead Halide Perovskite Materials	24
1.9. Stability of Caesium Lead Halide Perovskite Materials	26
1.9.1. Phase Stability	26
1.9.2. Light Stability	28
1.9.2.1. Photoinduced Halide Segregation	28
1.9.2.2. Polaron Formation	29
1.9.3. Thermal Stability	30
1.10. Energetics of Caesium Lead Halide PSCs	31
1.10.1. Interface Engineering	31
1.10.2. Defect Passivation	33
1.11. Challenges Regarding All-Inorganic PSC Phase Stability and High PCE	34
1.12. Piezoelectric Nanogenerator (PENG)	34
1.12.1. Piezoelectric Mechanism	35
1.13. Hybrid Devices for Harvesting Multi-Type Energies	37
1.14. Problem Statement	37
1.15. Aims of Research	38
1.16. Plan of Work	38
2. Materials and Methodology	40
2.1. Materials	40
2.2. Deposition Techniques for PSCs Fabrication	40
2.2.1. Spin Coating Method	40
2.2.2. Thermal Evaporation	41
2.3. Fabrication of PSC Devices	42
2.3.1. Fabrication of Inverted PSC Devices	42

2.3.1.1. Substrate Cleaning Procedure	42
2.3.1.2. Preparation of NiO _x Films	43
2.3.1.2.1. Surface Treatment of NiO _x Films.....	43
2.3.1.3. General Procedure for the Fabrication of Perovskite Films.....	44
2.3.1.3.1. Preparation of CsPbI ₂ Br Perovskite Films	45
2.3.1.3.2. Preparation of Non-Stoichiometric CsPb _{1-x} I _{2-x} Br Perovskite Films	45
2.3.1.3.3. Preparation of Cu Doped CsPb _{1-x} I _{2-x} Br Perovskite Films.....	45
2.3.1.4. Isopropanol Post-treatment of CsPbI ₂ Br Perovskite Films.....	45
2.3.1.5. Ethylene Diamine Treated CsPbI ₂ Br Perovskite Films	45
2.3.1.6. Preparation of C ₆₀ , LiF Layers and Cu Contacts	46
2.3.2. Fabrication of Normal PSC Devices	46
2.3.2.1. Substrate Cleaning Procedure	46
2.3.2.2. ZnO Nanorods Synthesis	46
2.3.2.2.1. Surface Treatment of ZnO Nanorods	47
2.3.2.3. Preparation of Perovskite Films.....	48
2.3.2.4. Preparation of Spiro Layer, Au Contacts and Device Encapsulation ..	48
2.4. Characterization Techniques	49
2.4.1. Techniques for Perovskite Film Characterizations.....	49
2.4.1.1. X-ray Diffraction (XRD)	49
2.4.1.2. X-ray Photoelectron Spectroscopy (XPS)	49
2.4.1.3. Photoluminescence (PL) Spectroscopy	50
2.4.1.4. Scanning Electron Microscopy (SEM)	50
2.4.1.5. Photoelectron Spectroscopy in Air (PESA).....	50
2.4.1.6. Ultraviolet-Visible (UV-Vis) Spectroscopy	50
2.4.1.7. Contact Angle Measurement.....	50
2.4.1.8. Atomic Force Microscopy (AFM)	51
2.4.2. Characterization Methods for PSCs	51
2.4.2.1. Current Density Voltage (J-V) Characteristics.....	51
2.4.2.2. External Quantum Efficiency (EQE)	51
2.4.3. Nanogenerator Performance Measurements.....	52
3. Results and Discussion.....	53
3.1. Compositional Engineering of CsPbI ₂ Br Perovskite	53
3.1.1. Performance Enhancement of CsPbI ₂ Br Perovskite Solar Cells via Stoichiometric Control	53

3.1.1.1. Structural Analysis and Stability Measurement.....	54
3.1.1.2. Photophysical Properties.....	55
3.1.1.3. Morphological Studies of Stoichiometric and Non-Stoichiometric Perovskite.....	57
3.1.1.4. X-ray Photoelectron Spectroscopic (XPS) Analysis.....	58
3.1.1.5. Photovoltaic Performance and Stability of Perovskite Solar Cells.....	59
3.1.1.6. Optimization of Hole Transport/Extraction Layer.....	61
3.1.1.7. Influence of C ₆₀ Layer Thickness on the Device Performance.....	64
3.1.1.8. EQE Measurement, MPP Tracking and Stability Test of Champion Device	66
3.1.2. Bivalent Copper Cation Doping Strategy Enables Reduced Defect Density and Improved Performance of Non-Stoichiometric CsPb _{1-x} I _{2-x} Br PSCs.....	67
3.1.2.1. Dopant Optimization and Device Performance	67
3.1.2.2. Structural Analysis	69
3.1.2.3. SEM and AFM Analysis	70
3.1.2.4. Optoelectronic Properties of IP and IPCu Perovskites	70
3.1.2.5. Photovoltaic Performance, MPPT and EQE Measurement of Champion PSC Device	73
3.2. Surface Treatment of CsPbI ₂ Br Perovskite.....	74
3.2.1. Surface Modification of CsPbI ₂ Br for Improved Performance of Inorganic Perovskite Solar Cells	74
3.2.1.1. Structural and Morphological Studies	75
3.2.1.2. Process Optimization and Device Performance.....	77
3.2.1.3. Photophysical Properties and their Impact on Device Performance....	78
3.2.1.4. Photovoltaic Performance and EQE Measurement	81
3.2.1.5. Device Stability.....	82
3.2.2. Amine-based Passivating Material to Improve the Performance of CsPbI ₂ Br Based Perovskite Solar Cells.....	84
3.2.2.1. Structural Analysis	84
3.2.2.2. Morphological Studies	85
3.2.2.3. X-ray Photoelectron Spectroscopic (XPS) Analysis.....	86
3.2.2.4. Photophysical Properties.....	87
3.2.2.5. Device Performance and Process Optimization.....	88
3.2.2.6. Transient Photocurrent (TPC) Measurements.....	90
3.2.2.7. Maximum Power-Point (MPP) Tracking	91

3.3. Hybrid Harvester Device: Synergistic Solar and Mechanical Energy Conversion for Sustainable Energy Harvesting	91
3.3.1. Stability Measurements of Perovskite Films	92
3.3.2. X-ray Diffraction (XRD) analysis	93
3.3.3. UV-Visible Absorption and SEM Studies.....	93
3.3.4. X-ray Photoelectron Spectroscopic (XPS) Analysis	95
3.3.5. Hybrid Device Performance	96
Conclusions.....	99
Future Recommendations	101
References.....	102

Index of Figures

- Figure 1.1:** (a) Comparison of total reserves available for nonrenewable energy resources to the yearly potential of renewables. (b) The solar radiation spectrum from 250 to 2500 nm. (c) The wide-ranging spectrum of electromagnetic radiation..... 2
- Figure 1.2:** Classification of solar cells into different generations. 4
- Figure 1.3:** Cubic crystal structure of ABX_3 metal halide perovskites. 6
- Figure 1.4:** (a) Structural designs for metal halide perovskites stated with tentative tolerance factor (t) value. (b) t value of different ABX_3 perovskite. 7
- Figure 1.5:** Outstanding characteristics of the halide perovskite material..... 9
- Figure 1.6:** Different techniques for the deposition of perovskite layer, (a) one-step deposition, (b) two-step deposition, (c) in-situ dipping method, (d) dual source thermal evaporation process and (e) vapor assisted deposition.. .. 11
- Figure 1.7:** Different architecture of PSC device, normal (a) mesoscopic and (b) planar, inverted (c) planar and (d) mesoscopic..... 13
- Figure 1.8:** The charge transport and recombination processes in PSC and the corresponding timeframe. 16
- Figure 1.9:** (a) Schematic of charge generation, relaxation, and sub-band transition in the perovskite absorber material. (b) Schematic illustration of three different recombination processes in perovskite. 18
- Figure 1.10:** (a) Solar Cell characteristic J-V Curve. (b) Equivalent circuit diagram ideal (c) typical solar cells. 19
- Figure 1.11:** The impact of shunt and series resistance on the I-V curve of a solar cell. 21
- Figure 1.12:** a) Structure and b) absorbance spectra of $CsPbI_3$ perovskite thin films. (c) Possible mechanism for HI or Bi^{3+} addition to stabilize the cubic phase of $CsPbI_3$ 23
- Figure 1.13:** (a-c) Transmission-spectra of $CsPbX_3$ as a function of temperatures vs bandgap absorption energies. (d) I_s transition energy vs temperature. (e) Dielectric constant (ϵ_{eff}), effective mass (μ), and binding energy R^* and vs bandgap while green spheres represent another experimental result. .. 25
- Figure 1.14:** Schematic representation showing Pb^{2+} substitution by several metal ions, which results in (a) stabilization of $CsPbI_3$ α - phase at ambient conditions by improving the tolerance factor and by increasing the formation energy, orthorhombic $CsPbBr_3$ thermal stability was improved. (b) Histograms represent the formation energy change (ΔE_{form}) for undoped and doped $CsPbBr_3$, (results based on first principle calculations). (c) Schematic illustration showing the perovskite phase stability in relation to I/Br ratio 27
- Figure 1.15:** PL-spectra of (a) $CsPbI_2Br$ (b) $MAPb(I_{0.5}Br_{0.5})_3$ (c) MPPT of the $CsPbI_2Br$ and $MAPbI_3$ based encapsulated PSCs for more than 1500 h. 29

Figure 1.16: Absorption spectra for perovskite absorber layer (a) CsPbI ₂ Br (b) MAPbI ₂ Br heated at 85°C for different times. Arrows depict the increase in heating time. Insets show the absorption intensity vs heating time. XRD-spectra for (c) CsPbI ₂ Br and d) MAPbI ₂ Br. The peak of PbI _{2-x} Br _x is represented by a diamond symbol.	30
Figure 1.17: Schematics of energy barriers at perovskite/CTL interface.	32
Figure 1.18: (a) Device architecture of fabricated PSC of CsPbI ₂ Br QDs film post-treated FAI. (b) corresponding energy level diagram.	32
Figure 1.19: (a) Schematic diagram of crack-filling using choline iodide (CHI). Corresponding energy diagram of the fabricated device (e) Pristine and (f) CHI treated.....	34
Figure 1.20: Operational mechanism of PENGs.	35
Figure 1.21: (a) Wurtzite-structured ZnO (atomic model). (b) Piezoelectric characteristics and different piezopotentials in the material's tension and compression modes. (c) Theoretical calculation of the distribution of piezoelectric potential under axial strain in a ZnO nanowire.	36
Figure 2.1: Schematic diagram of the spin-coating process.	41
Figure 2.2: Schematic of thermal evaporation deposition technique.....	42
Figure 2.3: (a) Diagrammatic representation (side view) of fabricated inverted PSC showing different layers. (b) Fabricated PSC devices. (c) Top view showing top and bottom contact with active area.	42
Figure 2.4: Steps for the preparation of the substrate.	43
Figure 2.5: Steps showing the preparation and post-treatment of NiO _x films.....	44
Figure 2.6: Schematics showing the preparation of perovskite films.....	44
Figure 2.7: Steps showing the synthesis of ZnO nanorods.....	47
Figure 2.8: Perovskite film fabricated on ZnO nanorods.....	48
Figure 2.9: (a)Thermal evaporation of Au and Cu strips attached to ITO and Au electrode. (b) Diagrammatic representation of side view of fabricated hybrid device showing different layers. (c) Top view of fabricated hybrid device.	49
Figure 3.1: (a,b) XRD patterns of perovskite thin films. (c) Comparison of the air stability of the stoichiometric and non-stoichiometric CsPbI ₂ Br perovskite films. (d) Contact angle measurement.	54
Figure 3.2: (a) UV-visible absorption spectra. (b) Tauc plot (c) SSPL and (d) TRPL spectra of the two perovskite films on a glass substrate. The films were excited using a 485 nm pulsed laser.	56
Figure 3.3: PESA measurements of (a) stoichiometric and (b) non-stoichiometric CsPbI ₂ Br perovskite. c) Energy level diagram of different layers used for the fabrication of PSC.....	57
Figure 3.4: (a) Top-down SEM images. (b) EDX elemental mapping stoichiometric (c) non-stoichiometric perovskite. (c) AFM images of the perovskites.....	58

- Figure 3.5:** (a) XPS survey spectrum of non-stoichiometric CsPbI₂Br thin film, high resolution (b) Cs 3d, (c) Pb 4f, (d) I 3d and (e) Br 3d core level spectra. **58**
- Figure 3.6:** Statistical distribution of the photovoltaic parameters of nine devices of each type stoichiometric and non-stoichiometric devices. **59**
- Figure 3.7:** (a) J-V curves of the champion stoichiometric and non-stoichiometric devices with an active area of 0.133cm² under 1 Sun (100 mW/cm²) illumination. (b) J-V curves of representative stoichiometric and non-stoichiometric devices showing their ambient stability. The devices were kept at ambient (un-encapsulated) for 24 hours and the J-V performance was measured before and after storage. (c) Photographs showing the comparison of the air stability of the stoichiometric and non-stoichiometric CsPbI₂Br devices. **60**
- Figure 3.8:** Statistical distribution of the photovoltaic parameters of three devices of each type for different types of NiO_x layers in PSCs. **62**
- Figure 3.9:** J-V curves of the champion solar cell with 20 nm sputtered and solution-processed NiO_x. **63**
- Figure 3.10:** Statistical distribution of photovoltaic parameters of ten devices for different thickness of C₆₀ layer in a device configuration ITO/NiO_x/perovskite/C₆₀/LiF/Cu..... **65**
- Figure 3.11:** (a) J-V curves of the best-performing cell (active area of 0.133 cm²) measured under 1 Sun (100 mW/cm²) illumination. (b) EQE spectrum of the champion cell. (c) Stabilized J_{sc} and PCE at maximum power point (held at 0.74 V). (d) Normalized PCEs as a function of storage time in the glovebox. **66**
- Figure 3.12:** Statistical distribution of photovoltaic parameters (six devices of each type) for pristine and with different percentage CuBr₂ devices..... **68**
- Figure 3.13:** (a) The photographs of IP and IPCu precursor solutions and fabricated perovskite films. (b) XRD patterns of IP and IPCu thin films. **69**
- Figure 3.14:** Top-down SEM images of the (a) IP and (b) IPCu films. (c) EDX mapping images of IPCu perovskite film. AFM image of the (d) IP and (e) IPCu films. **71**
- Figure 3.15:** (a) UV-Vis absorption spectra. (b) Optical band gap calculated by using Tauc plot. (c) PESA measurements of IPCu thin film. (d) Energy level diagram of the fabricated PSC..... **72**
- Figure 3.16:** (a) PL steady state and (d) TRPL spectra of IP and IPCu films on glass. **73**
- Figure 3.17:** (a) J-V curves of the best-performing IPCu device (active area of 0.133 cm²) measured under 1 Sun (100 mW/cm²) illumination. (b) Stabilized PCE at maximum power point (held at 0.77 V). (c) EQE spectrum of the champion cell..... **74**
- Figure 3.18:** (a) Schematic representation of the process for the preparation of the IPA treated CsPbI₂Br film. (b) XRD spectrum of the IPA-treated CsPbI₂Br film. (c) High-resolution XPS spectra of the Pb 4f_{7/2}, I 3d_{5/2} and C 1s from the

perovskite film surface (upper panel) and with IPA treatment (lower panel).	76
Figure 3.19: (a) Top-down SEM image of pristine and IPA treated film. (b) AFM images of pristine and IPA treated perovskite films.	76
Figure 3.20: Statistical distribution of photovoltaic parameters (eleven devices of each type) for IPA post-treatment for different times.	77
Figure 3.21: (a) UV-Vis absorption spectra. (b) SSPL spectra of pristine and IPA-treated perovskite on glass. (c) TPC measurements of pristine and IPA-treated devices. (d) Energy level diagram of each layer in the fabricated PSC stack.	79
Figure 3.22: (a) SSPL and (b) TRPL spectra of the pristine and IPA-treated perovskite films on ITO/NiO _x . (c) PESA measurements of pristine and (d) IPA-treated thin films.	80
Figure 3.23: (a) Current density-voltage curves of the champion pristine and IPA treated cells measured at 1 Sun (100 mW/cm ²) illumination. (b) EQE spectra of the best performing cells.	82
Figure 3.24: (a) Stabilized J _{SC} and PCE at MPP. (b) J-V curves of devices after MPPT. (c) Normalized PCEs of the pristine and IPA-treated PSCs as a function of storage time in the glovebox.	83
Figure 3.25: XRD spectrum of the pristine and EDA treated CsPbI ₂ Br thin films. ...	84
Figure 3.26: (a) Top-down SEM image (b) EDX elemental mapping of EDA treated film. (c) AFM images of pristine and EDA treated film.....	85
Figure 3.27: (a) XPS survey spectra of pristine and EDA-treated CsPbI ₂ Br films. (b-f) Corresponding high-resolution XPS spectra at the N 1s, Cs 3d, Pb 4f, I 3d and Br 3d regions respectively.....	86
Figure 3.28: (a) UV-Visible absorption spectra (b) SSPL (c) TRPL spectra of perovskite films on glass. (d) PESA measurements of pristine and (e) EDA treated thin films.	87
Figure 3.29: Statistical distribution of photovoltaic parameters (six devices of each type) for EDA treatment for different times.	89
Figure 3.30: (a) Energy level diagram for fabricated PSCs. (b) J-V curves of the champion pristine and EDA treated cells measured at 1 Sun illumination. (c) TPC measurements of devices. (d) Stabilized PCE at MPP.....	90
Figure 3.31: (a) Comparison of the air stability of the IP and IPPVP perovskite films. (b) XRD patterns of perovskite thin films.	93
Figure 3.32: (a) UV-Visible absorption spectra. (b) Optical band gap spectra of IP and PVP incorporated perovskite thin films.	94
Figure 3.33: Top view SEM images on glass/ITO substrate (a) IPPVP 1.5% (b) IPPVP 2%. (c) Top view and (d) Side view SEM image of IPPVP 1.5% on PET/ITO/ZnO nanorods. (e) EDX elemental mapping of IPPVP 1.5% perovskite film on glass/ITO substrate.	95

-
- Figure 3.34:** (a) XPS survey spectra of IP and IPPVP 1.5% perovskite thin films, (b) N 1s, (c) O 1s, (d) Pb 4f, (e) Cs 3d, (f) I 3d, (g) Br 3d and (h) C 1s spectra. **96**
- Figure 3.35:** (a) Architecture of the fabricated hybrid device. (b) J-V curves of the PSC (active area of 0.25 cm²) measured under 1 Sun (100 mW/cm²) illumination. **97**
- Figure 3.36:** (a) Magnetic shaker to test PENG performance. (b) Voltage-time scan of PENG nanogenerator by shaking at 27 Hz, 30 Hz and 33 Hz. (c) Voltage-time scan of PENG by shaking at 31 Hz on a cantilever. (d) The output power of device shaking and shaking + tapping at 31 Hz. **98**

Index of Tables

Table 1.1. Summary of notable ETMs and HTMs in PSCs.	15
Table 3.1. Photovoltaic parameters (average \pm std Deviation) of stoichiometric and non-stoichiometric device (nine devices of each type) with an active area of 0.133 cm^2 under 1 Sun (100 mW/cm^2) illumination.	60
Table 3.2. Photovoltaic parameters of the stoichiometric and non-stoichiometric device before and after air exposure for 24 hours.	61
Table 3.3. Photovoltaic parameters (average \pm std Deviation) of devices with different thickness of NiO_x for three devices per data point with an active area of 0.133 cm^2 , under 1 Sun (100 mW/cm^2) light illumination.	62
Table 3.4. Photovoltaic parameters of 20 nm sputtered and solution-processed NiO_x based champion devices under 1 Sun (100 mW/cm^2) illumination.	64
Table 3.5. Photovoltaic parameters (average \pm std Deviation) of devices with different C_{60} layer thickness for ten devices per data point (row 1) and champion device (row 2) under 1 Sun (100 mW/cm^2) illumination.	65
Table 3.6. Photovoltaic parameters (average \pm std Deviation) of PSCs with different percentage of CuBr_2 for six devices of each type with an active area of 0.133 cm^2 extracted from J-V measurements under 1 Sun (100 mW/cm^2) illumination.	68
Table 3.7. The fitting parameters for TRPL decay curves, band gap and VBM values obtained for IP and IPCu perovskite.	73
Table 3.8. Photovoltaic parameters (average \pm std Deviation) of devices with IPA treatment for different time for eleven devices per data point (row 1) and champion device (row 2) under 1 Sun (100 mW/cm^2) illumination.	78
Table 3.9. Photovoltaic parameters of forward (F) and reverse (R) scan of champion pristine and IPA treated device measured before and after MPPT.	83
Table 3.10: TRPL fitting parameters obtained by fitting the TRPL curve through the bi-exponential decay function.	88
Table 3.11. Photovoltaic parameters (average \pm std Deviation) of EDA treated devices for six devices per data point (row 1) and champion device (row 2) extracted from J-V measurements under 1 Sun (100 mW/cm^2) illumination.	89

List of Abbreviations

a-Si	Amorphous silicon
AFM	Atomic force microscopy
CdTe	Cadmium telluride
CIGS	Copper indium gallium selenide
CTL	Charge transport layer
CBM	Conduction band minimum
CsPbX ₃	Caesium lead halide perovskite
C60	[6,6]-C ₆₁ -butyric acid methyl ester
DSSCs	Dye-sensitized solar cells
DMSO	Dimethyl sulfoxide
ETL	Electron transport layer
EQE	External quantum efficiency
EDA	Ethylene diamine
HOMO	Highest occupied molecular orbital
HTL	Hole transport layer
hrs.	Hours
HI	Hysteresis index
FF	Fill factor
i-layer	Absorber layer
IPCE	Incident photon conversion efficiency
ITO	Indium tin oxide coated glass substrate
IPA	Isopropanol
IP	Non-stoichiometric CsPbI ₂ Br
IPCu	2% CuBr ₂ doped IP
IPPVP	PVP-incorporated perovskites
J-V	Current density-voltage
LUMO	Lowest unoccupied molecular orbital
MPP	Maximum powerpoint
MPPT	Maximum powerpoint tracking
NG	Nanogenerator
OIH	Organic inorganic hybrid
PV	Photovoltaic

PCE	Power conversion efficiency
PSCs	Perovskite solar cells
P _{max}	Maximum power output
PL	Photoluminescence
PENG	Piezoelectric nanogenerator
PVP	Polyvinylpyrrolidone
PESA	Photoelectron spectroscopy in air
R _s	Series resistance
R _{sh}	Shunt resistance
RMS	Root mean surface roughness
Spiro	Spiro-O-MeTAD
SSPL	Steady state photoluminescence
SEM	Scanning electron microscopy
t	Tolerance factor
TCO	Transparent conducting oxide
TRPL	Time-resolved photoluminescence
TPC	Transient Photocurrent
μ	Octahedral factor
UV-Vis	Ultraviolet-visible
VOC	Open circuit voltage
VBM	Valence band maxima
XRD	X-ray diffraction
XPS	X-ray photoelectron spectroscopy

Abstract

Organic-inorganic hybrid perovskite solar cells (PSCs) are considered an excellent replacement for high-cost conventional silicon solar cells. The unique optical and electrical properties of the perovskite materials, low-cost fabrication techniques and potential for solution processing make PSCs economically viable and scalable for large-scale production. However, the instability of organic cations in organic-inorganic hybrid perovskite materials presents a challenge that needs to be addressed for the commercialization of PSCs. To overcome this, caesium (Cs) based all-inorganic perovskite (CsPbX_3 where $X = \text{Cl, Br, and I}$) has emerged as a more suitable alternative due to its excellent stability under various environmental conditions and excellent optoelectronic properties.

However, various imperfections in perovskite absorber material and its interfaces greatly reduce the efficiency and stability of perovskite solar cells (PSCs) and retard the practical applicability of inorganic halide perovskite. This thesis offers strategies to overcome these issues. Two different methodologies were adopted which include the compositional engineering and surface or post-treatment of CsPbI_2Br perovskite. The structural analysis of modified perovskite material was done by XRD and photophysical properties were investigated by UV-Visible and photoluminescence (PL) spectroscopy. Photoelectron spectroscopy in air (PESA) measurements were used to analyze the valence band structure of the materials. Morphological analysis of perovskite material was done by SEM and AFM images. XPS measurements were performed to study the details of changes at an atomic level and bonding information. Further, the modified perovskite material was also applied to PSC devices to see the effects of different modifications on the photovoltaic performance of fabricated devices. Current density voltage (J-V) measurements were performed to acquire data for the characterization of the devices.

The compositional engineering of CsPbI_2Br perovskite was done by altering the stoichiometry of CsPbI_2Br referred as non-stoichiometric perovskite. The non-stoichiometric perovskite material demonstrated improved stability and better photovoltaic characteristics compared to its stoichiometric counterpart. Afterward, the B-site doping of non-stoichiometric perovskite was done using CuBr_2 . The structural, photophysical and morphological analysis confirmed the presence of Cu^{2+} and

demonstrated that an optimal quantity of Cu^{2+} can significantly improve the optoelectronic properties of the perovskites. The PSC devices were prepared which showed 15% improvement in the performance.

For post-treatment two different strategies were used, one was the surface treatment of the CsPbI_2Br perovskite film with isopropanol (IPA) while another was the defect passivation via Lewis acid base post-passivation method. The IPA treated CsPbI_2Br absorber layer showed reduced defect density and showed energetically more favorable band alignment with the electron transport layer (ETL). The resultant PSC led to a 30% improvement in the photovoltaic performance with reduced hysteresis. In case of Lewis acid base passivation, the simplest amine ethylene diamine (EDA) was used. This passivation reduced the surface trap states and prolonged the charge carrier lifetime within the device. Consequently, the PSC fabricated with EDA passivation exhibited significantly improved PCE (9.4%) as compared to the reference device (7.3%) under 100 mWcm^{-2} illumination.

In addition, the concept of a hybrid energy harvester (HEH) device was also demonstrated to collectively harvest outdoor solar and mechanical energies by a single device. For that, perovskite solar cell with normal architecture was chosen, wherein the perovskite absorber layer converts solar energy, while the piezoelectric properties of ZnO nanorods served as a unit for harvesting mechanical energy. The active response of HEH to both solar and mechanical energies demonstrates strong potential of the proposed device and as future ubiquitous energy harvester.

1. Introduction

This chapter introduces solar cell technology, the fundamentals of perovskite material and perovskite solar cells and their characteristic parameters. Moreover, the literature review on caesium based lead halide perovskite as an absorber material in perovskite solar cells, their properties, energetics, key challenges and strategies towards commercialization are also briefly discussed in this chapter. Along with this a brief introduction on piezoelectric nanogenerator and hybrid harvester device is also given at the end of this chapter.

1.1. Renewables as a Source of Sustainable Energy

Global population growth and rapid urbanization have increased the global energy demand. It is anticipated that between 2017 and 2040, the world's power demand will rise by 58%.¹ A vast majority of the growing demand is coming from developing nations, where millions of people will be lifted above low-income categories by rapidly increasing emerging economies.² Hence, in this situation the key challenge is how to satisfy energy demand without endangering the environment. In the past, fossil fuels have been most widely employed for energy generation. These natural resources are, however, finite and only available in specific regions of the world. The main concern related to fossil fuels is global warming due to the emission of greenhouse gases like CO₂ and methane. Therefore, the growing need for energy, rising CO₂ emissions and exhaustion of conventional energy sources by human society demands a safe, inexpensive, inexhaustible, omnipresent and renewable source of energy. Until now, many renewable energy sources including geothermal, hydrothermal, wind, tidal and solar have been extensively used as a savior in the energy crises over a few decades.³

Among various energy sources, solar energy is considered as the most efficient and promising one owing to its small environmental impact, low cost, and plenty of the availability. Therefore, harnessing the power of the Sun is the most viable option to resolve the foreseeable world's energy crises. The solar energy released by the Sun comprises almost 99% of the total energy on the earth.⁴ **Fig. 1.1(a)** demonstrates the comparison of renewable and conventional energy sources in which solar energy surpasses by order of magnitude the potential of all other renewable alternatives combined. The uniqueness of solar energy can also be estimated from the fact that approximately one hour of continuous irradiance of solar energy can fulfill the annual

world's energy requirements. Additionally, in three days, the Sun provides energy that is equal to energy stored in all the fossil fuel energy sources.

1.1.1. The Sun and Solar Radiations

A model of the Sun and its radiations assumes that the Sun is spherical and the spectrum of its radiation is approximately equivalent to the spectrum of a black body. Its surface has a temperature of about 6000 K due to energy produced by the nuclear fusion of hydrogen and helium inside the blackbody. Anything with a temperature greater than zero degree Kelvin emits electromagnetic radiation. So, the Sun lies in the middle of the solar system and radiates electromagnetic radiation constantly. When sunlight reaches Earth, its intensity is reduced due to the dispersion with particles and gases which leads to a change in the spectrum.⁵

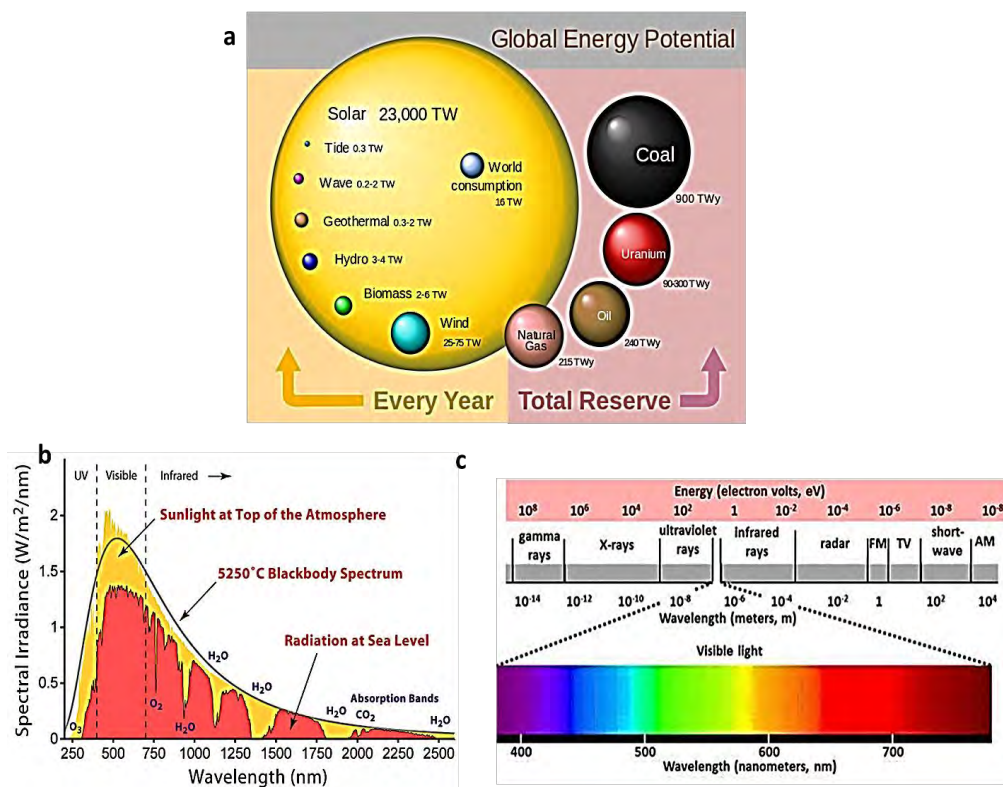


Figure 1.1: (a) Comparison of total reserves available for nonrenewable energy resources to the yearly potential of renewables.⁶ (b) The solar radiation spectrum from 250 to 2500 nm. (c) The wide-ranging spectrum of electromagnetic radiation.⁵

The Sun emits radiation, including gamma rays, x-rays, ultraviolet, visible light, infrared, and radio waves. These radiations are classified based on their energy and wavelengths. These are called spectral regions as shown in **Fig. 1.1(b and c)**. The term used to describe the rate at which solar energy reaches a unit area on the Earth is called

“insolation” or “solar irradiance”. It is measured in watts per square meter (W/m^2).

Solar energy can be used in two main ways one is to heat water and the other is to generate electricity. The first method, solar thermal technologies encompass heating liquids or water either to produce steam to drive a turbine for electricity production or to produce hot water for domestic purpose.⁷ But this process requires a lot of heat to generate electricity. The second method is to produce electricity via solar photovoltaics. This method involves a direct conversion of sunlight into electricity thus resulting in a more effective energy storage and transportation step. Therefore, the use of energy conversion devices (i.e., solar cells or photovoltaics) to harvest the solar energy seems to be a favorable solution to solve the world’s energy and environmental problems.⁸

1.2. Solar Photovoltaic

Experimentally, in 1839 French physicist E. Becquerel was the first to convert solar energy into electricity, he demonstrated the photovoltaic (PV) activity by observing the voltage develops between oppositely charged electrodes dipped in an electrolytic solution, on exposure to light.⁹ In 1873 a similar effect (photoconductivity) was observed in selenium by Willoughby Smith and the first design of a cell based on selenium wafer was proposed by Charles Fritts in 1883. Afterward, Albert Einstein proposed the theory of the photoelectric effect in 1905 which explains how the electrons are knocked out from the metal surface by light. In 1918, Jan Czochralski develops a method for the growth of single-crystal silicon (Si) and set the foundation of Si-based solar cells. While the birth of PV occurred in 1954 after the fabrication of crystalline Si-based solar cell in Bell lab, USA with a power conversion efficiency (PCE) of 4.5%. They found that silicon is a more efficient absorber material compared to selenium.⁸

1.2.1. Evolution of Solar Cells

Since the discovery of solar cells in Bell Labs, scientists have been enthusiastically investigating low-cost materials and device technologies exhibiting the PV effect and hence opening up new perspectives for the commercialization of solar cells. Several solar cell technologies exist today and can be categorized based on absorber material (**Fig. 1.2**) and cost as well. The solar cells are traditionally categorized into three generations as given below:

1.2.1.1. First-Generation Solar Cells

The first-generation solar cells are well-developed in terms of their fabrication process

and technology. These are the oldest commercially available PV technologies and are based on silicon wafers. The device is typically a p-n junction. The first generation is further subdivided into two categories:

- i. Mono crystalline silicon solar cells
- ii. Poly crystalline silicon solar cells

Mono crystalline silicon solar cells achieve an efficiency of 21-22% in real-world modules. Although these solar cells have high efficiency and lifetime, but the fabrication process requires high-budget, labor input and sophisticated technology. So, the high production cost gives rise to the use of poly-crystalline silicon solar cells in which many silicon crystals are connected to form a single device. Moreover, silicon is an indirect bandgap material, so a thick layer of silicon is required to absorb sunlight.¹⁰

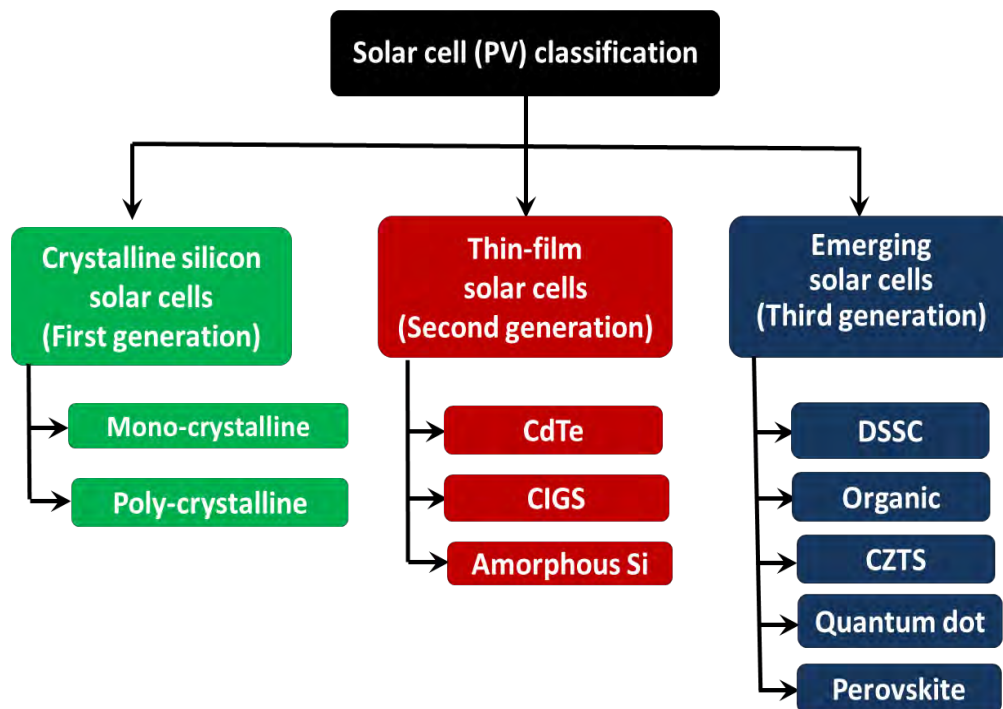


Figure 1.2: Classification of solar cells into different generations.

1.2.1.2. Second-Generation Solar Cells

The low absorption coefficient and indirect band gap of silicon solar cells led to the development of second-generation solar cells. These are thin film solar cells and are further classified as:

- i. Amorphous silicon (a-Si) solar cells
- ii. Cadmium telluride (CdTe) solar cells
- iii. Copper indium gallium selenide (CIGS) solar cells

These materials have excellent PV properties thus viable to use 1 μm thick film compared to ~ 300 μm of crystalline silicon thus it's a low-cost technology. Moreover, low temperature for fabrication offers the potential of utilizing flexible substrates. A commercial PV module made from silicon with an efficiency of $\sim 4 - 8\%$ is unstable while in the case of CIGS type solar cells efficiency is $\sim 21\%$ but it's limited lifetime and complicated module technology made its commercialization difficult.¹¹ Whereas the second largest commercial technology after silicon is CdTe having an efficiency of $\sim 14\%$. However environmental hazards and toxicity associated with Cd are the main issues related to this type of solar cell. Thus second-generation solar cells could not partake profitable market owing to instability and technological faults.¹²

1.2.1.3. Third-Generation Solar Cells

The early 1990s came up with the evolution of the third generation of solar cells, a potential replacement for 1st and 2nd generations but have limited commercial success. This technology uses organic materials such as dyes, conjugated polymers as a light absorber and charge transport material and embrace a wide range of different generations i.e.

- i. Organic solar cells
- ii. Dye-sensitized solar cells (DSSCs)

Organic and DSSCs with an efficiency approaching 20% and 11.9% respectively use inexpensive materials and offer large-scale production. Although these solar cells have low efficiency, but their low production cost and plausible real word applications such as portable electronics and clothes make them more appealing.¹¹

Even though these solar cells have many advantages, their low stability and poor efficiency urge scientists to find new PV technology that has a combination of low cost and high efficiency. With substantial efforts of researchers in developing novel perovskite materials and improved device design the PCE of perovskite solar cells (PSCs) has shown an appreciable rise from 3.8% in 2009 to 25.8% in 2022 in single junction solar cells.¹³ This improvement can be attributed to the favorable characteristics of PSCs, such as a high absorption coefficient, direct bandgap, long charge carrier diffusion length, and a high defect tolerance. Subsequently among all these technologies, organic inorganic hybrid (OIH) PSCs are the most promising and reliable for third-generation technology having an efficiency of 25.8% and are expected

to reach 50% in the future.^{14,15} These findings became even more exciting by considering their rapid progress in comparison to other PV technologies.¹⁶

1.3. Origin of Perovskite Semiconductor

Gustav Rose in 1839 first discovered this mineral and is named after Russian mineralogist Count Lav Aleseevich Perovski. Perovskite has a general formula of ABX_3 with a crystalline structure similar to calcium titanium oxide ($CaTiO_3$) shown in **Fig. 1.3**. The structure comprises of cubes, with A representing the larger cation positioned at the middle of the cube, B representing the metal cation occupying the corners, and X representing the halide anion situated at the center of the edges. Even though perovskite material was first reported in the nineteenth century, only in the last decade these materials have been successfully utilized in solar cells.

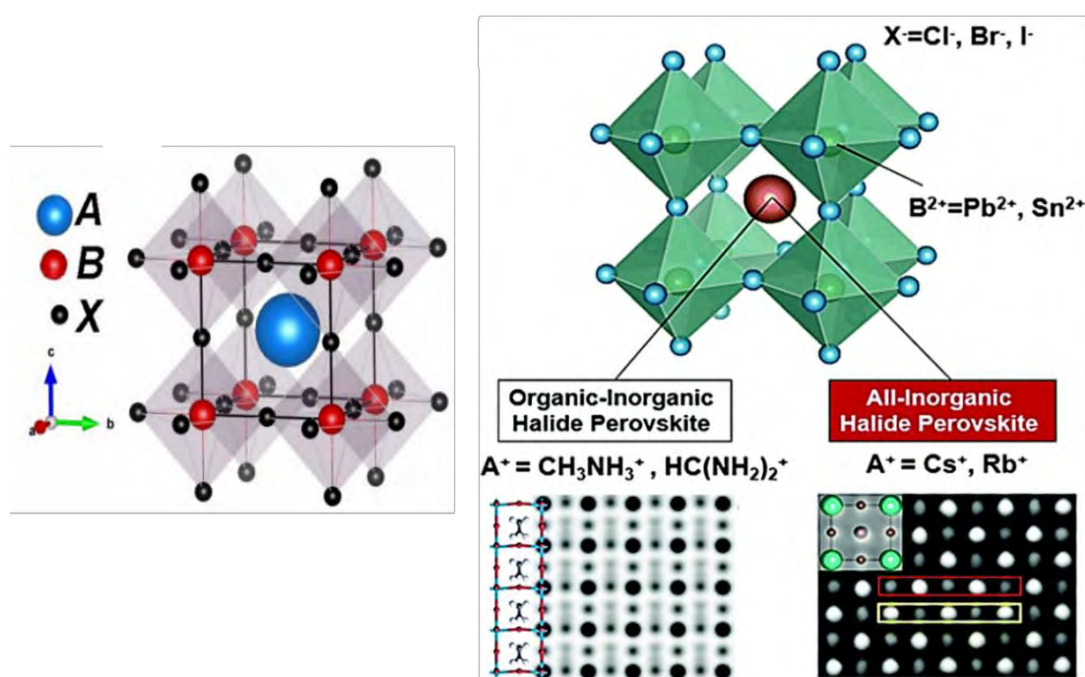


Figure 1.3: Cubic crystal structure of ABX_3 metal halide perovskites.¹⁷

The flexibility in composition allows all elements from the periodic table to be used in perovskite compounds and results in a wide range of optical, electronic, and magnetic properties. Perovskite material used in solar cells usually has methylammonium (MA), formamidinium (FA), ethylammonium (EA) or caesium (Cs) as an A cation. B^{2+} is a bivalent metallic cation (Sn^{2+} , Pb^{2+} , etc.) and X^- is a monovalent halide anion (Cl^- , Br^- , I^-). Generally, the “B” cation is surrounded by six X^- forming a BX_6 octahedra, creating a three-dimensional framework. “A” cation, typically bigger than “B”, balances the charges and fills the interstitial sites between the octahedra.

The structural diversity of perovskite material helps us to alter the electrical and optical properties as well as the bandgap of the material.¹⁷ The ability of the dynamic octahedra to tilt within its corner-sharing network causes perovskites to consistently display a rich structural diversity. Usually, a perovskite material exhibits three different phases, cubic, orthorhombic and tetragonal.

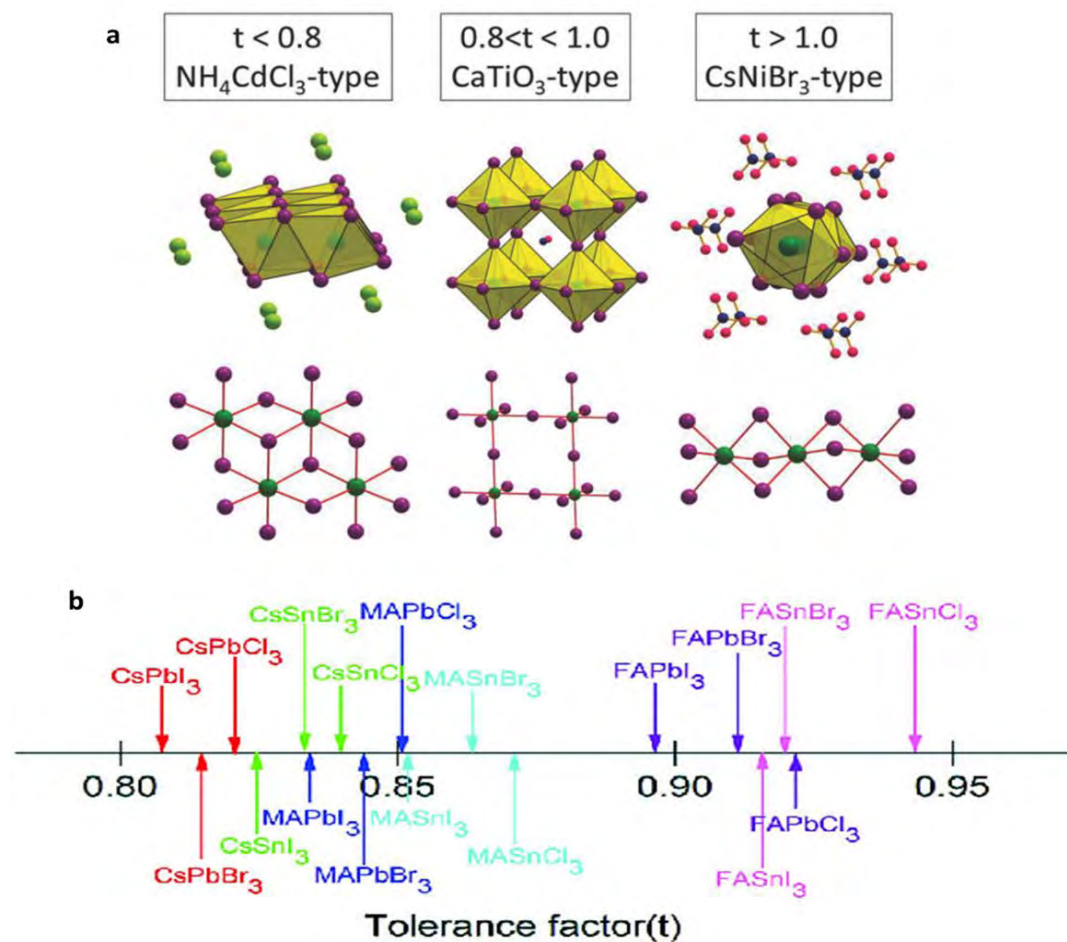


Figure 1.4: (a) Structural designs for metal halide perovskites stated with tentative tolerance factor (t) value.¹⁸ (b) t value of different ABX₃ perovskite.¹⁹

The crystal structure of perovskite can also be determined by tolerance factor (t) introduced by Goldschmidt in 1926²⁰ that is:

$$t = \frac{r_A + r_X}{\sqrt{2}(r_B + r_X)} \quad (1.1)$$

Here r_A , r_B , and r_X represents the ionic radii of monovalent cation (organic/inorganic), bivalent metallic cation, and monovalent halide anion respectively.²¹

The perovskite crystal structure stability depends upon the size of monovalent cation A^+ and the correlation between cation A^+ and corner-sharing atom BX_6^{4-} . The t value

predicts the stability and phase of perovskite crystal. If the t value is between 0.8 and 1.0 the resulting phase will be cubic, also known as the black or α -phase. When t exceeds 1, a non-perovskite phase with a hexagonal structure will form. On the other hand, if t is greater than 0.7 but less than 0.8, the resulting phase will be either orthorhombic or rhombohedral, also referred as the yellow or δ -phase.^{16,22–24} **Fig. 1.4** is showing structural designs for metal halide perovskites with their tentative tolerance factor (t) value and t value of different ABX_3 perovskite.

Likewise, the thermal expansion in perovskite crystal will cause the internal bond lengths to change at different rates, which will force a continual change in the volume of a unit cell. This thermal response results in a constrained temperature range wherein a stable perovskite phase might form for each particular composition. For instance, the typical non-perovskite to perovskite phase transition temperatures of $CsPbI_3$ and $FAPbI_3$ perovskites are higher than RT; >315 °C for $CsPbI_3$ and >125 °C for $FAPbI_3$. On the contrary, the $MAPbI_3$ is stable at room temperature owing to its appropriate tolerance factor. The comparatively high phase transition temperatures of $CsPbI_3$ and $FAPbI_3$ make the stabilization of optically active cubic phase a significant ongoing problem in the field.^{25,26} Alternately, adding smaller cations to the B-site alloy, such as Sn^{2+} or Mn^{2+} , can help in lowering the tolerance factor and developing a room temperature stable perovskite crystal.²⁷

Moreover, the octahedral factor (μ) was introduced to access the adjustment of bivalent metallic cation B into octahedron X_6 .²⁸ The octahedron factor (μ) is:

$$\mu = \frac{r_B}{r_X} \quad (1.2)$$

Here r_B and r_X are the ionic radii of the bivalent cation B and monovalent halide X. The t and μ define different arrangements of the A, B, and X for perovskite. For a stable perovskite structure, the t and μ should be in the range of $0.81 < t < 1.11$ and $0.41 < \mu < 0.90$ respectively. To date, the discovered perovskite, exhibit a wide variety of band gap from $MAPbCl_3$ (3.1 eV), $MAPbBr_3$ (2.3 eV), $MAPbI_3$ (1.6 eV) and $MASnI_3$ (1.1 eV). Likewise, by altering the chemical composition of A (MA^+ , FA^+ , Rb^+ , Cs^+ etc.) cations and X (I^- , Br^- , Cl^- etc.), anions it is possible to tune the band gap.²⁹ Moreover, by preserving the composition of perovskite but varying quantum confinement, one can also accomplish the same objective. All these adjustability and flexibility make this

semiconductor material suitable for PV and other sophisticated optoelectronic devices such as photo detector³⁰, light-emitting diode³¹ and laser³² etc.

1.3.1. Benign Properties of Perovskite Semiconductors

Halide perovskites exhibit a variety of unique properties shown in **Fig. 1.5** that distinguish them from other materials. These properties include high absorption coefficient and small Urbach energy, long charge carrier diffusion length, significant defects tolerance and low cost. These unique properties make halide perovskites highly promising for a wide variety of applications in optoelectronics and other fields. A brief description of these properties is given below:



Figure 1.5: Outstanding characteristics of the halide perovskite material.³³

1.3.1.1. High Absorption Coefficient and Small Urbach Energy

Perovskites have an absorption coefficient that is even higher than the conventional semiconductors, which drastically minimizes the thickness of the absorber layer to 500 nm. Besides that, a small Urbach energy for perovskite also implies that it is an excellent semiconductor having negligible deep trap states.³⁴ All these unique characteristics of perovskites empower the excellent performance of PSCs.

1.3.1.2. Long Charge Carrier Diffusion Length

Perovskite exhibits a significantly longer charge carrier diffusion length compared to

other semiconductors, which make it an excellent choice for use in high-performance devices. Contrary to organic semiconductors, long charge carrier diffusion length of perovskites makes them suitable for a planar hetero-junction with selective charge transport layers. This allows the direct integration of the perovskites between an n-type and p-type layer, results into the development of planar p-i-n or n-i-p architecture with an efficiency equivalent to the mesoporous architecture, along with the benefit of low-temperature fabrication. Thus, the triumph of a planar architecture PSC is not only due to high absorption coefficient of perovskite but also due to excellent charge carrier transport.

1.3.1.3. Unique Defects Physics

One of the numerous distinctive characteristics of perovskite is its significant tolerance to defects. According to theoretical calculations, the intrinsic defects in perovskite generate only in shallow levels, which is in accordance with the small open circuit voltage (V_{OC}) loss and long charge carrier diffusion length in PSCs.³⁵ These shallow level defects also offers the opportunity to use the material as an effective material for solar cells since these defect slightly contribute in non-radiative recombination.

1.3.1.4. Low Costs

At low temperature, high-quality perovskite crystals could be synthesized because of the low energetic barrier for crystal growth. The ability to process perovskite materials at low temperatures guarantees the scalability of the PSCs for large-area devices, particularly in high-output processing techniques like the roll-to-roll approach. As a result, the fabrication cost is substantially reduced but still need to maintain high performance.³⁶ All these incredible properties make perovskite an excellent semiconductor absorber material with low cost that has not been detected in any other semiconductors (Si, GaAs, CdTe, CIGS) featuring high performance.

1.3.2. Perovskite Film Deposition Techniques

The high-quality, perovskite thin film is a main prerequisite to attain high PCE. Therefore, numerous researchers put a lot of effort to control the film morphology and hence increase the quality of perovskite film. The morphology of the perovskite film was regulated by optimizing numerous factors like deposition techniques, annealing temperature, environmental conditions, initial material composition, solvent engineering and use of various additives. Till now, there are five deposition techniques

for the deposition of perovskite film, a schematic illustration of these deposition methods has been given in **Fig. 1.6**.

1.3.2.1. One-Step Deposition

The one step deposition process is the most widely employed deposition process for PSC manufacturing because of its simple and easy processing. This process involves the mixing of perovskite precursors in a suitable solvent (DMF, NMP, DMSO and GBL) to get a clear solution. Then, the precursor solution is spin-coated or drop-cast on a p-type or n-type substrate to form a film of the perovskite material. After deposition annealing is also required to complete the formation of desired perovskite structure.³⁷ One-step deposition for thin film deposition is shown in **Fig. 1.6(a)**.

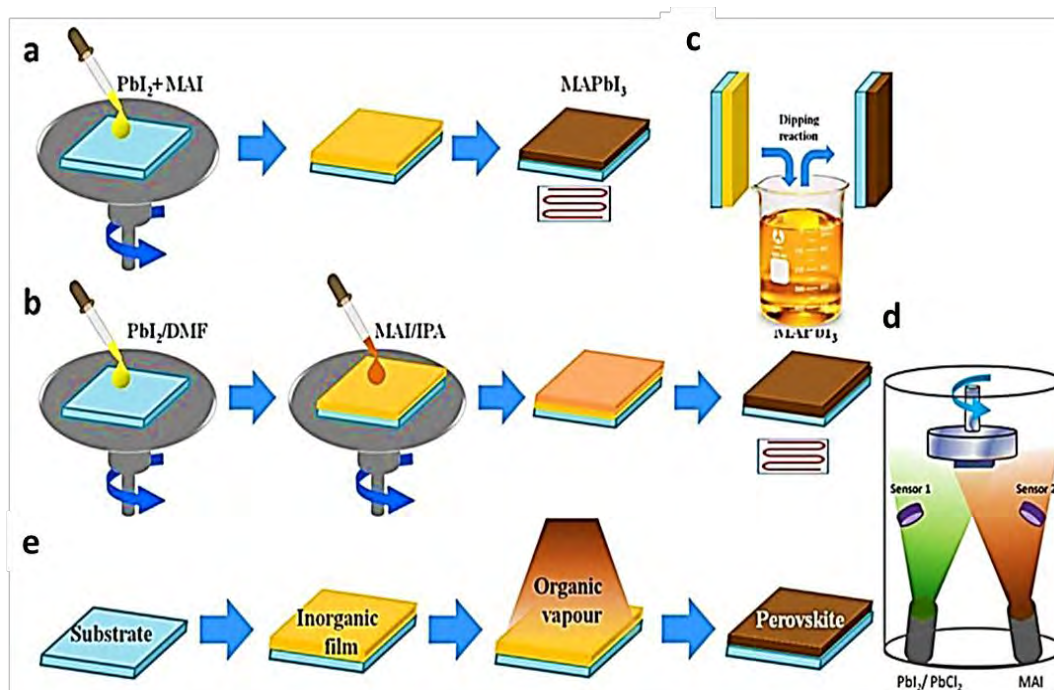


Figure 1.6: Different techniques for the deposition of perovskite layer, (a) one-step deposition, (b) two-step deposition, (c) in-situ dipping method, (d) dual source thermal evaporation and (e) vapor assisted deposition.

1.3.2.2. Two-Step Deposition

The two-step deposition process involves the step-wise formation of the precursor layers to improve the morphology of the perovskite layer (**Fig. 1.6(b)**). In this method, precursors are dissolved separately to form a solution. The first step involves the spin coating of precursor solution on a substrate followed by annealing to obtain a thin film of perovskite precursor. In the second step, the solution of the second perovskite

precursor is spin-coated on an already deposited film of the first precursor to start the perovskite crystallization reaction.³⁸

1.3.2.3. In-Situ Dipping Method

The rough texture of perovskite films due to rapid crystallization and low viscosity of perovskite precursors leads to devices with poor performance. Therefore, the deposition of the pinhole-free and compact film is still a challenge for researchers. To resolve this issue new methods are being employed for the fabrication of PSCs. In-situ dipping reaction is one of them (**Fig. 1.6(c)**). This process involves the formation of PbX_2 by spin coating followed by immersing the coated substrate into the solution of AX in IPA and then heating it to form a perovskite film.³⁹

1.3.2.4. Vapor-Assisted Deposition

Vapor-based or vapor-assisted coating techniques are also widely used in addition to solution-based deposition techniques to improve the morphology and surface coverage. In 2013 Liu et al. first introduced the dual-source deposition technique in which both precursors for perovskite (AX and BX_2) were loaded into two different evaporation boats as shown in **Fig. 1.6(d)**.⁴⁰ Extremely uniform perovskite films are produced by co-evaporating these sources by precisely adjusting their evaporation rates with the aid of two sensors. On the contrary, this is a high energy-consuming procedure owing to its need for high vacuum ($\sim 10^{-7}$ mbar) at very high temperatures. Later on, Yang et al. introduced a vapor-assisted deposition technique to deposit perovskite film (**Fig. 1.6(e)**). It combines vapor and solution coating techniques.⁴¹

The fabrication techniques previously addressed are mostly focused on the fabrication of uniform, pinhole-free solar cells. Other environmental factors like humidity, temperature, and solvent preference also play an important role. More innovative methods for improved interfaces and grain size might have a significant impact in developing a uniform pinhole-free film with higher crystallinity to enhance the stability and performance of devices. Additionally, lab-scale device fabrication methods should be well-established and directed towards the development of large-scale fabrication methods. The optimization of these methods must be actively pursued in order to advance perovskite technology towards the commercialization stage.⁴²

1.4. PSCs Architectures:

Apart from modifying the perovskite composition different device architectures have

also been analyzed. PSC structure commonly contains an absorber layer (i-layer) which is inserted between hole transport layer (HTL) and electron transport layer (ETL). Generally, working of PSC comprise few steps which involve the absorption of a photon by the perovskite absorber layer, followed by the production of excitons which are then dissociated into electrons and holes either into the perovskite layer or at the heterojunction interface. Subsequently, photogenerated charge carriers are transferred via HTL and ETL to an external circuit to generate electric current.

PSCs are classified into two categories n-i-p or normal and p-i-n or inverted based on which charge transport layer (CTL) encountering by incident light first. It can be classified as mesoscopic or planar based on the structure. It is termed as a mesoscopic device when a mesoporous material is utilized, and a planar device when the layers are thin films. **Fig. 1.7** displays the various PSC architectures, standard mesoscopic (**Fig. 1.7(a and d)**) and planar (**Fig. 1.7(b and c)**) device architecture in normal configuration (glass/FTO/TiO₂/ perovskite/HTL/Au) and in inverted configuration (glass/ITO/HTL /perovskite/ETL/Al).

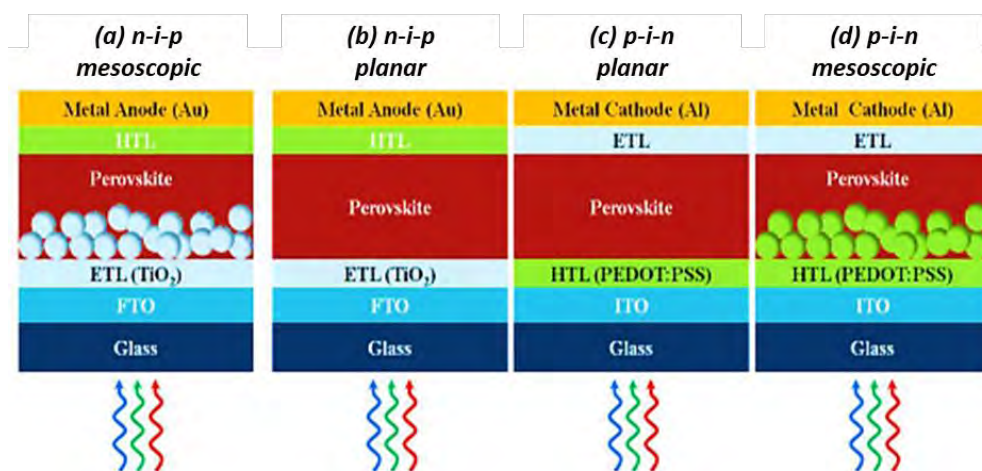


Figure 1.7: Different architecture of PSC device, normal (a) mesoscopic and (b) planar, inverted (c) planar and (d) mesoscopic.¹³

1.4.1. Mesoporous Architecture

The DSSC gives rise to the mesoporous architecture of the PSC, where the sensitizer material is present within the pores of a mesoporous layer.⁴³ In DSSC liquid electrolyte is used which is an obstacle towards stability, this issue was resolved by the fabrication of solid-state perovskite materials. In contrast to the Si solar cells where transport of holes and electrons occurs through the same material, in mesoporous architecture CTL either transport holes or electrons.

1.4.2. Planar Architecture

In planar architecture, a mesoporous scaffold is removed, which leads to an advantage of a low-temperature production method that makes it more flexible for application in flexible substrates and tandem solar cells. Additionally, it makes possible to use various synthetic methods and interfacial modification to develop devices with improved performance.⁴⁴ However, the characteristics of the perovskite film are one of the main obstacles as it, governs several aspects, such as exciton dissociation, charge transport and diffusion length.^{45,46} These structures are further divided into regular (n-i-p) and inverted (p-i-n) configurations. The n-i-p configuration consists of a conductive substrate on which an n-type ETM is deposited, followed by a perovskite layer and a p-type HTL with a metal electrode on it. While in an inverted configuration, the perovskite layer is deposited on the HTL layer. However, the planar structure has a problem of trap-assisted non-radiative recombination which impair the device performance.^{47,48} According to several studies, the inverted configuration minimizes the hysteresis in PSCs and the quest for efficient and stable devices headed the researchers to explore the inverted architecture.⁴⁹⁻⁵¹

1.4.3. Charge Transport Materials

1.4.3.1. Hole Transport Materials (HTMs)

A basic PSC architecture comprises of light absorber material and CTLs to transport generated electrons and holes. For efficient transfer of holes, HTM is required with an electronic property of high mobility and low resistance and it should have higher valence and conduction band edge compared to the perovskite layer for electron rejection and efficient hole extraction. In PSC, both inorganic and organic HTMs have been used as given in **Table 1.1**.

1.4.3.2. Electron Transport Materials (ETMs)

The ETL is necessary for a smooth transport of electrons to the electrode, the ETM must have a wide bandgap, good mobility, and compatible band alignment with perovskite material for efficient transfer of electrons. In addition to good antireflection properties, it should have compact morphology and pinhole-free film to prevent direct interaction with the transparent conducting oxide (TCO). Commonly used ETMs are given in **Table 1.1**.

Overall CTLs play a vital role in PSC device as it directly impacts the device stability and performance. An appropriate CTL could increase the reliability of charge transportation, reducing recombination and could modify itself with different dopants.

Table 1.1. Summary of notable ETMs and HTMs in PSCs.

Device architecture	ETM	HTM	Ref.
SnO₂/PCBM/perovskite/FBT-Th4:Cu_xO	SnO ₂	FBT-Th4: Cu _x O	52
SnO₂/MAPbI_{3-x}Cl_x/ SpiroMeOTAD	SnO ₂	SpiroMeOTAD	53
ZnO/MAPbI₃/ SpiroMeOTAD	ZnO	SpiroMeOTAD	54
CdSe/MAPbI₃/Spiro-MeOTAD	CdSe	SpiroMeOTAD	55
MoS₂/MAPbI₃/Spiro-MeOTAD	MoS ₂	SpiroMeOTAD	56
WO₃/MAPbI_{3-x}Cl_x/ SpiroMeOTAD	WO ₃	SpiroMeOTAD	57
c-TiO₂/m-ZrO₂/MAPbI₃/C	ZrO ₂		58
Fe₂O₃/PCBM/MAPbI₃/ SpiroMeOTAD	Fe ₂ O ₃ - PCBM	SpiroMeOTAD	59
m-TiO₂/MAPbI₃/ SpiroMeOTAD	TiO ₂	SpiroMeOTAD	60
c-TiO₂/MAPbI_{3-x}Cl_x/P3HT	TiO ₂	P3HT	61
TiO₂/Perovskite/CuSCN	TiO ₂	CuSCN	62
CoO_x/MAPbI₃/PCBM	PCBM	CoO _x	63
PEDOT:PSS/Perovskite/PCBM	PCBM	PEDOT:PSS	64
NiO_x/Perovskite/PCBM/TiO_x	PCBM	NiO _x	65
Co_{1-y}Cu_yO_x/Perovskite/PCBM	PCBM	Co _{1-y} Cu _y O _x	66

PTAA/MAPbI ₃ /PCBM/BCP	PCBM	PTAA	67
PEDOT:PSS/Perovskite/PCBM	PCBM	PEDOT:PSS	68
CuO _x /MAPbI ₃ /C ₆₀ /BCP	C ₆₀	CuO _x	69

1.5. Working Principle of Perovskite Solar Cells

A simplified working of PSCs encompasses the transmittance of incoming light from TCO followed by absorption by the absorber perovskite layer. Owing to the high absorption coefficient and low exciton binding energy of perovskites, almost 100% of the incident light is absorbed by the perovskite layer with a thickness of less than 500 nm. After photon absorption free carriers or exciton are generated within a timescale ranging from a few femtoseconds to picoseconds.⁷⁰ Then the free charge carriers moved in the perovskite layer by diffusion. This activity usually, requires several nanoseconds.^{45,71} Owing to the large charge carrier diffusion length of perovskite films the charge carriers are further transported to their related interface contacts. During this process numerous unwanted processes may occur as shown in **Fig. 1.8**.

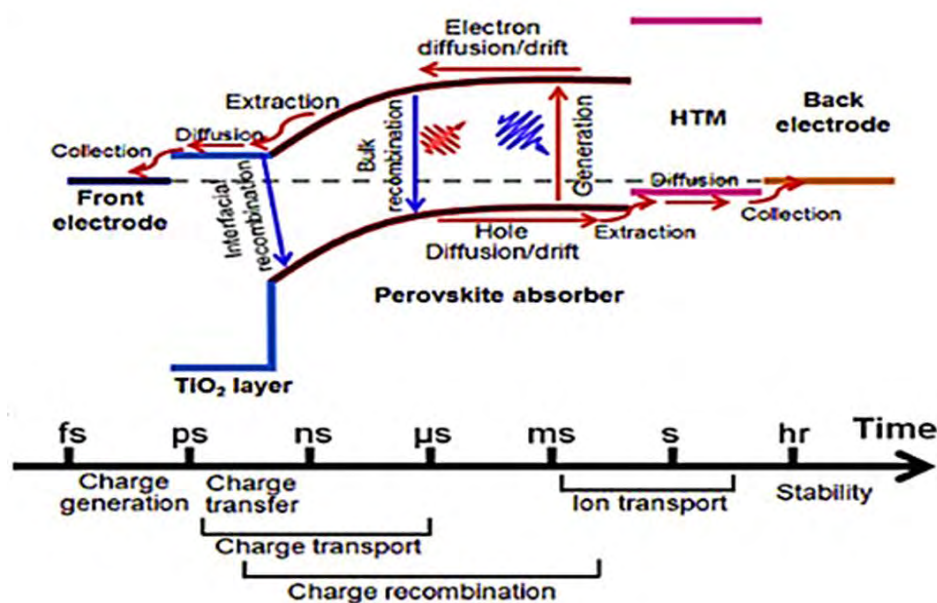


Figure 1.8: The charge transport and recombination processes in PSC and the corresponding timeframe.⁷²

The remaining electrons and holes can pass through their respective interface and will be extracted at the electrodes, several microseconds are required for this process.⁷²

Finally the charge carriers are transported to an external circuit to produce electricity. Various charge transport and recombination processes in PSC and the corresponding timeframe are schematically described in **Fig. 1.8**.

1.5.1. Charge Generation

Upon photoexcitation, the early-stage process is charge generation.^{73,74} When a photon having energy equal to or higher than the E_g interacts with valance band electrons results in the excitation of charges to form free carriers or excitons. Some carriers jumped from energy positions higher than the valance band maximum (VBM) and conduction band minimum (CBM) to high energy sub-bands creating hot carriers (**Fig. 1.9(a)**). Then after electron-phonon interactions, these hot carriers relax to the VBM or CBM. Apart from intra-band transitions, sub-band relaxation can also happen when numerous sub-bands are present and charge carriers are excited by high-energy photons.⁷⁵

1.5.2. Charge Transport and Recombination

The free charge carriers must undergo transport processes to be extracted by CTL and collected at an electrode, where a dynamic competition occurs between the recombination and transport process.^{76,77} An important property of perovskites is its long charge carrier diffusion length. This remarkable feature surpasses the absorption depth, thus recommending efficient charge collection.⁷⁸ The movement of electrons and holes within perovskites is directly associated to the effective masses of holes and electrons. The electron mass of perovskite ($0.2m_e$) is low and very close to standard GaAs, semiconductor.⁷⁹ The free charge carrier decay can be explained through equation given below:

$$\frac{dn}{dt} = -k_3n^3 - k_2n^2 - k_1n^1 \quad (1.3)$$

where k_1 is the rate constant related to trap-related recombination (monomolecular recombination), rate constant k_2 is correlated with band-to-band recombination (bimolecular recombination) and rate constant k_3 is associated with Auger recombination which is related to charge-carrier density. All these recombinations (**Fig. 1.9(b)**) participate in total charge recombination. The rates of trap-assisted recombination in perovskite films vary from tens to hundreds of nanoseconds, and is significantly influenced by the processing conditions. The electronic band structure

affects Auger recombination. The additional bands in perovskite due to the spin-orbit coupling resulted in a high Auger recombination rate constant ($(0.2-1.6) \times 10^{-28} \text{ cm}^6\text{s}^{-1}$) which is significantly higher than GaAs. Though it might be a problem for their application in laser but it would not affect their application in photovoltaics.

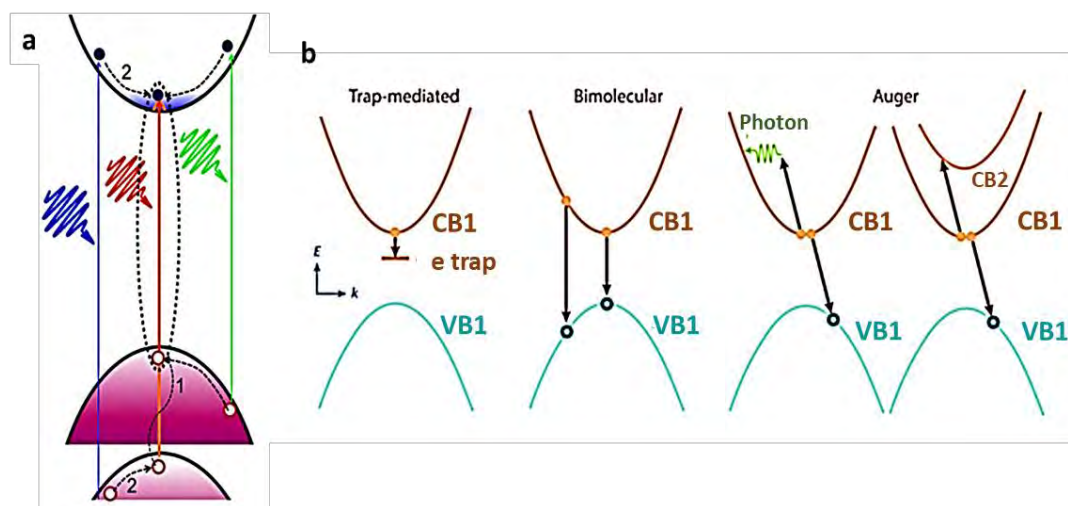


Figure 1.9: (a) Schematic of charge generation, relaxation, and sub-band transition in the perovskite absorber material.⁷² (b) Schematic illustration of three different recombination processes in perovskite.⁸⁰

1.5.3. Charge Extraction

For efficient extraction of charge carriers from the perovskite layer, careful selection of the corresponding CTL is important. Moreover, these CTLs should have favorable alignment of energy levels to the VBM and CBM of the perovskite respectively. The V_{OC} of the PSC depends on the energetics of the transporting layers and the radiative recombination of the perovskite.⁸¹ Additionally, unbiased charge extraction at interfaces plays an important role in optimizing the device's performance.

1.6. Solar Cell Characteristic Parameters

Here in this section, the solar cell characteristics parameters that are required to explain the current density-voltage (J-V) curves of the solar cell will be illustrated. The characteristic J-V curve of a solar cell is mainly the graphical illustration of the operation of a PV cell or module that summarizes the correlation between the current and voltage at given conditions of temperature and irradiation thus giving a detailed explanation of its output performance. Therefore, knowing the J-V characteristics (most importantly P_{max}), of a solar cell is necessary to find out the device efficiency. As shown in **Fig. 1.10(a)** solar cell behaves like a diode. The comprehensive detail of the electric

response of a PV cell can be obtained through an equivalent circuit diagram (ECD). The ECD of an ideal solar cell is simply a diode coupled to a light source but usually, it incorporates both series resistance (R_s) and shunt resistance (R_{sh}) (Fig. 1.10(b and c)). The important parameters required to explain the PV characteristics of a solar cell are given below:

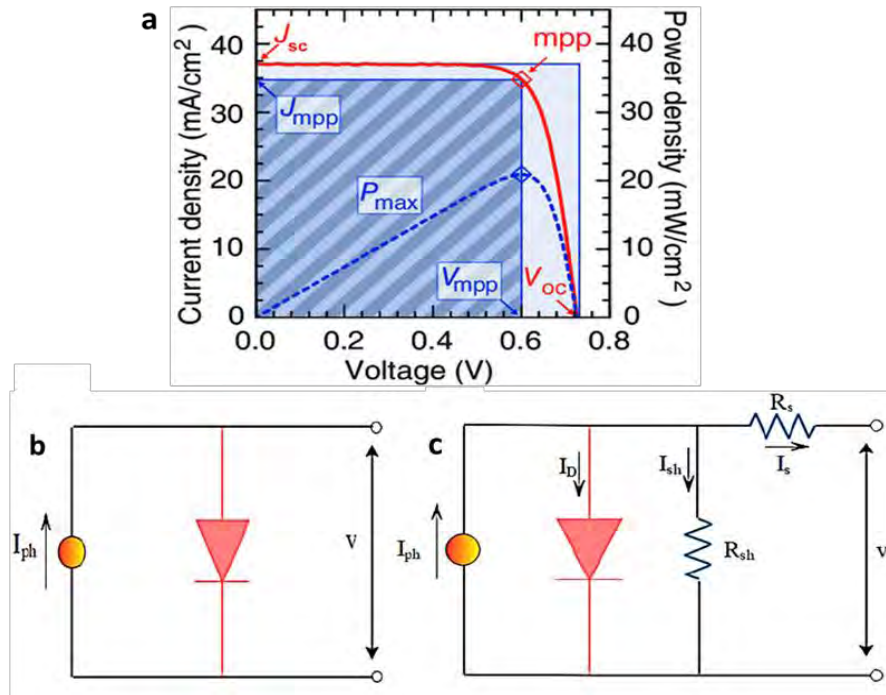


Figure 1.10: (a) Solar Cell characteristic J-V curve.⁸² (b) Equivalent circuit diagram ideal (c) typical solar cells.⁸³

1.6.1. Open Circuit Voltage (V_{oc})

A V_{oc} is the maximum achievable voltage output of a solar cell. This corresponds to a voltage at which no current will flow through the circuit. It depends on the charge carrier recombination and semiconductor band gap. Generally, V_{oc} changes according to the current produced through the light source and the saturation current density of the PV cell. Though the photocurrent produced by incident photons (J_{ph}) has a minor variation, the major effect is because of the saturation current. So V_{oc} is a measurement of the amount of recombination in the solar cell due to the saturation current density.

1.6.2. Short Circuit Current (I_{sc})

The I_{sc} corresponds to the highest current produced by a solar cell under illumination when $V=0$. At this condition, no power will be produced. For an ideal device, $I_{sc} = I_{ph}$ but various factors can lower the value of I_{sc} from its ideal value. To represent the

behavior of PV cell I is generally not suitable as current depends on area. Hence, the current density is used as an alternative to I and is represented as:

$$J_{SC} = \frac{I_{SC}}{A} \quad (1.4)$$

Where A represents the area of a solar cell.

1.6.3. Maximum Power Output (Pmax)

Pmax is the maximum power that can be obtained from the solar cells and is marked in **Fig. 1.10(a)**. It can be explained as a point at which the product of J and V is maximum.

$$P_{max} = J_{max} \cdot V_{max} \quad (1.5)$$

Due to the resistance in a device and recombination losses, V_{max} and J_{max} are always lower than V_{OC} and J_{SC} .

1.6.4. Fill Factor (FF)

FF is the ratio between maximum obtainable power from a solar cell and the product J_{SC} and V_{OC} . In an ideal case, the value of FF is ~ 1 . Usually, the difference arises from internal losses as described earlier. Generally, FF provides a comparison between the real solar cell efficiency to the ideal cell efficiency. It is represented as follows:

$$FF = \frac{(J_{max} \cdot V_{max})}{(J_{SC} \cdot V_{OC})} \quad (1.6)$$

It shows the closeness of J_{max} and V_{max} to the J_{SC} and V_{OC} . Solar cells with higher J_{SC} and V_{OC} and lower FF suggests that a fault is present, and device needs to be improved.

1.6.5. Power Conversion Efficiency (PCE)

The PCE is defined as the ratio between the maximum power generated by a solar cell and the power incident on the solar cell. Apart from reflecting the solar cell performance the PCE is affected by the temperature of the solar cell and the intensity and spectrum of the incident light. The terrestrial solar cell is measured under AM 1.5 and a temperature of 25 °C. The mathematical expression representing the PCE is:

$$PCE = \frac{P_{out}}{P_{in}} = \frac{(FF \cdot J_{SC} \cdot V_{OC})}{P_{in}} \quad (1.7)$$

where P_{in} is the power absorbed by sunlight. Efficiency is normally taken in percentage.⁸²

1.6.6. Incident Photon Conversion Efficiency (IPCE)

It is the ratio between no. of incident photons and the no. of photogenerated charge carriers generated by a solar cell at a specific frequency. This efficiency is also said as Quantum Efficiency (QE) or 'External Quantum Efficiency (EQE). Losses from recombination, scattering, and reflection are also considered by IPCE.

$$IPCE = \frac{N_{photons}}{N_{charge}} \quad (1.8)$$

1.6.7. Series Resistance (R_s)

The R_s is the consequence of contact resistance. It lowers the fill factor which affects the PCE of the solar cell. It depends upon the current passing through the device, the contact resistance of the electrode and the resistance between the device active area and metal electrodes. A minimal R_s is preferred for the best performance of PV cells. With a high value of R_s , the probability of charge carrier recombination increases which lowers current density and consequently, solar cell efficiency.

1.6.8. Shunt Resistance (R_{sh})

The low shunt resistance provides an alternating current for the photogenerated power thus resulting in a significant power loss. The shunt resistance minimizes the chances of unnecessary current paths which leads to the charge carrier recombination before collection. Therefore, R_{sh} should be high for an efficient solar cell. A slight change in R_{sh} puts an unfavorable impact on the V_{oc} , FF and device's efficiency. **Fig. 1.11** shows the impact of shunt and series resistance on the I-V curve of a solar cell. To maximize the solar cell performance R_{sh} is to be infinitely large and R_s to be zero.⁸⁴

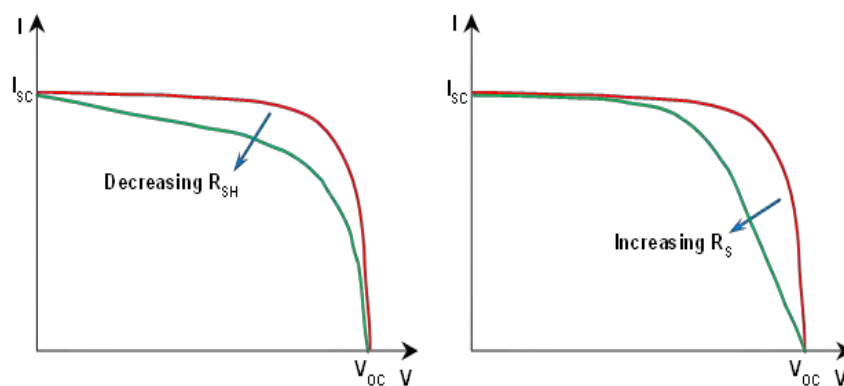


Figure 1.11: The impact of shunt and series resistance on the I-V curve of solar cell.⁸⁴

1.7. Inorganic Caesium Lead Halide Perovskites for PSCs

The application of OIH perovskites in PV devices was first reported in 2009 by Miyasaka's group.⁸⁵ Since that time, interest in perovskite material has increased due to its broad absorption spectra, high carrier mobility and high extinction coefficient.^{45,86} But, the organic component in perovskite is highly volatile, hygroscopic, and inclined to thermal degradation.⁸⁷ This led to a question in the scientific community "Is the organic cation compulsory to achieve high-quality PSCs?" This question is answered by Kulbak et al. by the substitution of the polar organic components in perovskite with non-polar (Cs^+) component and the resultant caesium lead halide perovskite (CsPbX_3) have more stability.⁸⁸ Moreover, the partial substitution of organic component (MA/FA) with inorganic cation (Cs^+) also improved the thermal stability of the perovskite phase in a wide range of temperatures by favorably tuning the t value.⁸⁹ Currently, all-inorganic perovskite (i.e., where a Cs^+ completely replaces the organic component) is an ultimate way to diminish the problem of chemical decomposition and air stability without compromising the characteristics of PV materials. CsPbI_3 perovskite first synthesized by Wells et al. has a perfect combination of thermal stability, band-gap and absorption coefficient for applications in PV devices.⁹⁰ Generally a material with an ideal cubic structure has a t value of 0.9-1.0. Regrettably, the Cs^+ cation in CsPbI_3 is too small for a stable cubic phase at ambient temperature and the photoactive cubic phase of CsPbI_3 (α - CsPbI_3 , $\text{Pm}3\text{m}$) with a t value of 0.81 is only stable above 320 °C which revert rapidly to yellow non-perovskite phase (γ - CsPbI_3 , Pnma). The PCE of PSC with γ - CsPbI_3 did not surpass 0.09%.⁹¹ Thus one of the most challenging tasks in utilizing CsPbI_3 in PSC is to stabilize its photoactive cubic phase under ambient conditions.⁹² In 2015 opening the way towards PSC containing inorganic perovskite material Eperon et al. revealed that γ - CsPbI_3 could be converted into the α - CsPbI_3 at 100 °C by the addition of HI in the perovskite precursor solution.⁹³

Fig. 1.12(a and b) depicted the structure and absorbance spectra of both phases γ , orthorhombic (band-gap of ≈ 2.82 eV) at ambient temperature, and α , cubic (band-gap of ≈ 1.73 eV) at $T > 300$ °C or 100 °C with HI. The resulting PSC with the CsPbI_3 absorber layer demonstrated a PCE of 1.7 for inverted and 2.9% for the regular devices.

Considering these results, Hu et al. use the one-step deposition method to further stabilize the photoactive phase of CsPbI_3 at ambient condition by partially replacing the Pb^{2+} (1.19 Å) with Bi^{3+} (1.03 Å) which increases the t value from 0.81 (α - CsPbI_3) to

0.84 (α -CsPb_{1-x}Bi_xI₃).⁹⁴ The possible mechanism for the α -CsPbI₃ stabilization by HI or Bi³⁺ addition is given in Fig. 1.12(c). Moreover, the addition of chloride precursor in the MAPbI₃ precursor solution increases its air stability.⁹⁵ Motivated by this fact, Dastinar et al. enhanced the stability of CsPbI₃ nanocrystals by introducing chlorine as a dopant.⁹⁶ Afterward the colloidal nanocrystals of CsPbI_{3-x}Cl_x perovskite were synthesized and applied as a thin film in PSC.⁹⁷ The doped film showed improved phase stability under humid conditions.

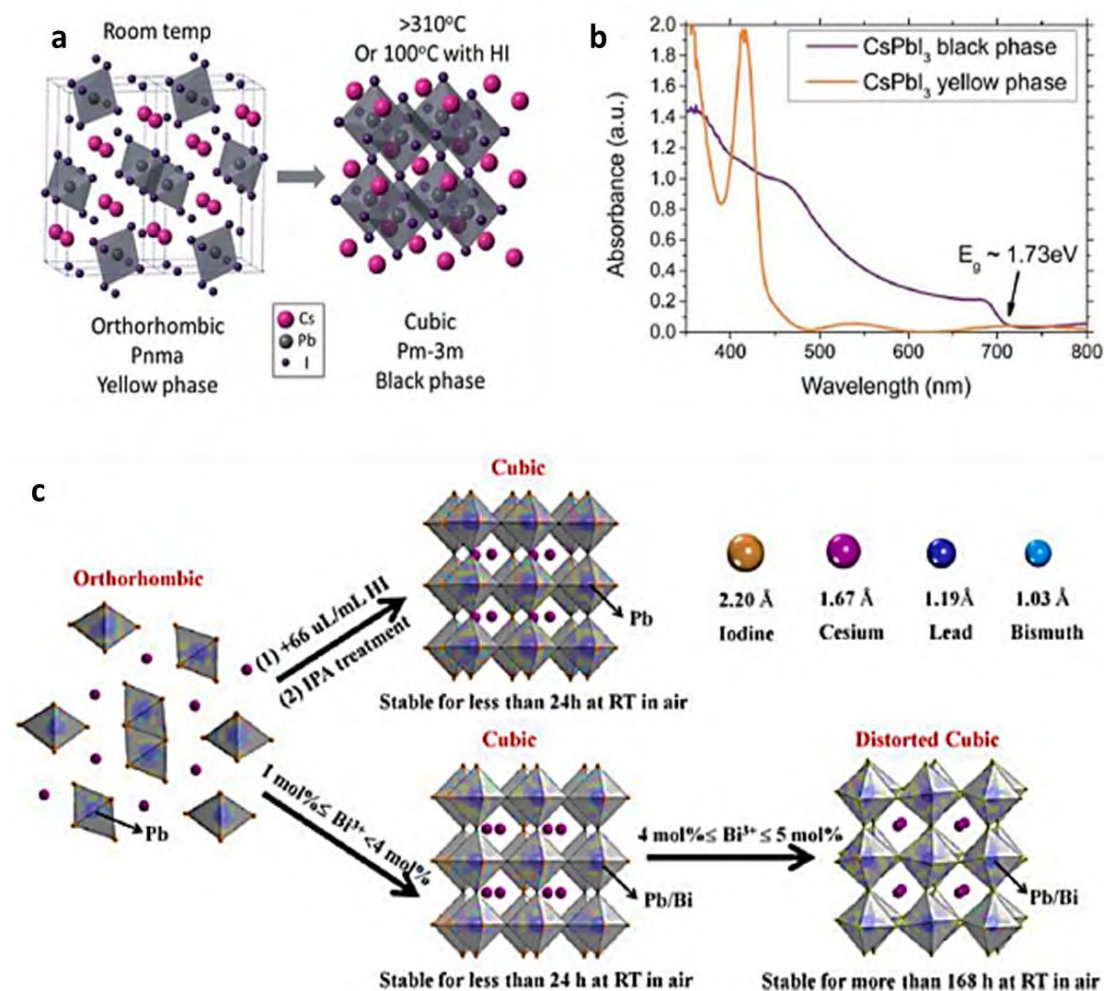


Figure 1.12: a) Structure and b) absorbance spectra of yellow and black phase of CsPbI₃ perovskite thin films.⁹³ (c) Possible mechanism for HI or Bi³⁺ addition to stabilize cubic (black) phase of CsPbI₃.⁹⁴

In addition, CsPbBr₃ perovskite (completely replacing the I⁻ with Br⁻) is a potential material for stable PSC but its efficiency is limited owing to its relatively large band gap.⁹⁸ Due to the limited solubility of Cs precursors used for the CsPbBr₃ synthesis, it is difficult to adapt the conventional solution process method for the fabrication of perovskite devices.⁹⁹ The dilemma related to solution processing for the CsPbBr₃,

owing to the limited solubility of the precursor's salts, was resolved by Protesescu et al. using the two-step process.⁹⁷ Based on these observations Sutton et al. demonstrated that this process could be reduced to a one-step solution process method by partially incorporating Br in CsPbI₃.¹⁰⁰ Thus, CsPbI₃ structural stability was enhanced by choosing the appropriate ratio of the mixed halide in the perovskite material. Among various CsPbX₃ perovskite, CsPbI₂Br presented a trade-off between phase stability, band gap and efficiency and become a promising material as inorganic perovskite absorber material for PV applications. Two different types of device configurations were reported based on m-TiO₂ (mesoporous) and cTiO₂ (compact). Planar devices exhibited the highest PCE of 9% with an average efficiency of 6%. After these exciting results of CsPbI₂Br Kennedy et al. further characterize the CsPbI₂Br perovskite through excited-state diffusion and ultrafast recombination dynamics.¹⁰¹ Considering these outcomes Nam et al. used different annealing conditions that cause significant changes in the surface morphology and PV characteristics. They fabricate CsPbI₂Br perovskite films by the solution-processed method using a one-step spin-coating technique followed by annealing at a temperature range from 100-350 °C.¹⁰² Sutton et al.¹⁰³ Niezgodna et al.¹⁰⁴ executed experiments in the glovebox to prevent moisture and air that might have remarkable impact on crystal growth and decomposition of perovskite. Thus, by using the best annealing conditions, highly effective planar PSCs with the configuration of glass/FTO/TiO₂/CsPbI₂Br/spiro-MeOTAD/Au were fabricated and the champion device exhibited a V_{OC} of 1.23 V and a PCE of 10.7%.

1.8. Properties of Caesium Lead Halide Perovskite Materials

Theoretical calculations to determine the electronic structures of CsPbX₃ have demonstrated to be highly useful in predicting their optoelectronic properties. Based on theoretical calculations it was determined that in CsPbX₃ perovskites, the electronic structures have qualitatively revealed the same features for different halide compositions. Golibjon R. et al. stated by using DFT calculations that when organic cation is substituted by inorganic Cs⁺, the optoelectronic properties of both OIH and CsPbX₃ perovskites remain unaffected.¹⁰⁵ Nicholas et al. were the first to analytically studied the basic properties of Cs lead halide perovskites, such as its dielectric screening, reduced mass (μ), exciton binding energy (R*) and phase transition via low-temperature magneto-transmission spectroscopy. For CsPbI₃, CsPbBr₃ and CsPbI₂Br the temperature-dependent transmission spectra (**Fig. 1.13(a-c)**) were examined at the

temperature range from 4.2 to 270 K. Bandgap tuning by replacing the heavier halide atom in the perovskite lattice was highlighted by a red shift in absorption energy from CsPbBr₃ to CsPbI₃ via CsPbI₂Br, which is closely related to experimental results.¹⁰⁶

Fig. 1.13(d) shows bandgap absorption energy with temperature. The bandgaps display a well-shaped monotonic temperature dependency, indicating the presence of cubic perovskite phase of CsPbX₃ even at cryogenic temperatures. This is in contrast with OIH perovskite where an increase in the band gap is observed corresponding to the phase change by a change in temperature. This remarkable phase stability of CsPbX₃ will serve as a foundation for making stable and durable PSCs.¹⁰⁷

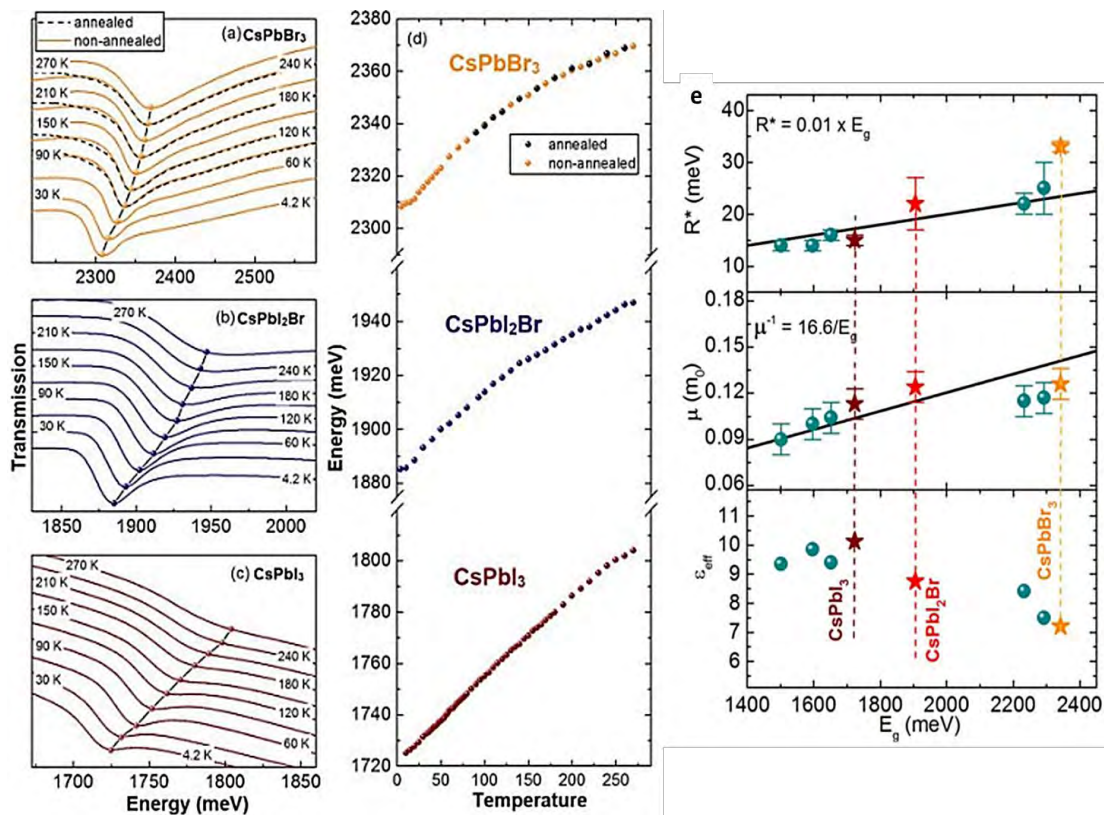


Figure 1.13: (a-c) Transmission-spectra of CsPbX₃ as a function of temperatures vs bandgap absorption energies. (d) 1s transition energy vs temperature. (e) Effective dielectric constant (ϵ_{eff}), effective mass (μ), and binding energy R^* vs bandgap¹⁰⁷ while green spheres represent another experimental result.¹⁰⁸

All-inorganic perovskites' exciton binding (R^*) energy of CsPbI₃ is comparable to MAPbI₃ but for CsPbI₂Br and CsPbBr₃ it increases which demonstrated that by the incorporation of heavier halide, the free carrier R^* increases in perovskite lattice.^{101,107}

The experimentally determined values of " ϵ_{eff} ", " μ " and " R^* " for CsPbX₃ perovskites (**Fig. 1.23(e)**) showed that by increasing the value of bandgap the carrier effective mass also increases.

1.9. Stability of Caesium Lead Halide Perovskite Materials

A PSC must produce long-lasting PCEs for commercial usage and industrial requirement. The OIH perovskite semiconductors degrade quickly in the presence of continuous illumination, moisture or heat. CsPbX₃ perovskites have shown enhanced stability towards light and heat but are still vulnerable to moisture. The phase, thermal and light sensitivity of CsPbX₃ perovskite is described in the subsequent section.

1.9.1. Phase Stability

The unwanted thermodynamic phase change in CsPbX₃ perovskite is still one of the obstacles, hampering the progress and commercialization of high-performance devices. It is possible to improve the phase stability of these perovskites either through doping directly into the perovskite layer or by modifying the perovskite grain size.¹⁰⁹ In terms of doping, there are three feasible approaches that might be employed to clarify the resultant microstructure. (1) the dopants might modify the surface of perovskite (2) the dopant may develop a distinct phase and not affect the phase of perovskite (3) the dopants may replace the other components. In the first situation, the change in crystal surface can have an impact on the growth rate with surface passivation and reduction in the crystal size. The second scenario may result in a complicated amalgam of phases as with the addition of K or Rb. The third scenario appears plausible as it enhances the perovskite lattice's total entropy and stabilizes it thermodynamically.^{110–113}

The CsPbI₂Br is the only all-inorganic perovskite material that has an acceptable band gap along with phase stability for PV devices. However, the operational stability of PSCs has been compromised due to the slight phase instability caused by the smaller size of Cs⁺ in retaining the [PbX₆]⁴⁻ octahedra and lower tolerance factor value of CsPbI₂Br ($t = 0.855$).¹¹⁴

Several research groups have proposed and adopted B-site substitutional doping to improve the phase stability of perovskite and retain the tolerance factor within a reasonable range. Substitution of Pb with other metals minimized the toxicity issue along with the stabilization of the perovskite photoactive phase. Swarnkar et al. conducted a comparison of the properties of undoped and doped CsPbBr₃ nanocrystals and determined the change in tolerance factor and formation energy for various dopants per Pb²⁺ ion by using the first principle calculation shown in **Fig. 1.14(a and b)**.¹¹⁵ Therefore, it is necessary to optimize B-site doping, which could resolve the perovskite

phase instability problem without impairing its optoelectronic capabilities. Phase instability has shown to be effectively combated by germanium (Ge) as a B-site dopant due to improved effective tolerance factor (teff). Additionally, among CsPbI₂Br perovskites, the PSC with an optimized composition (CsPb_{0.8}Ge_{0.2}I₂Br) showed the greatest V_{OC} of 1.34 V.¹¹⁶ Europium (Eu), was also employed as a B-site dopant. The ionic radius of Eu²⁺ is less than that of Pb²⁺, therefore the substitution of cation at B-site by Eu improved the teff and enhanced the CsPbI₂Br perovskite phase stability. The partial incorporation of Eu suppresses the nonradiative recombination that considerably enhanced the V_{OC}.¹¹⁷

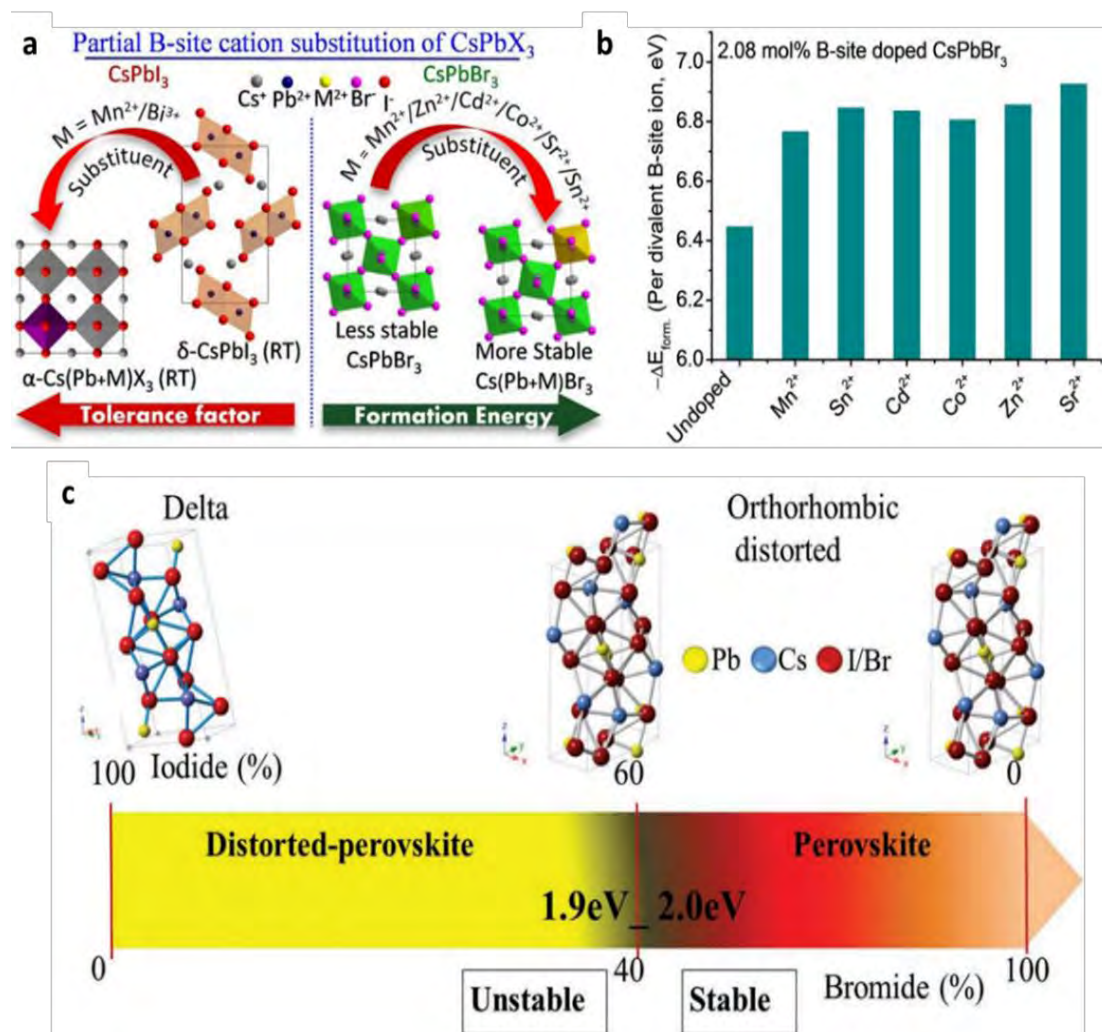


Figure 1.14: Schematic representation showing Pb²⁺ substitution by several metal ions, which results in (a) stabilization of CsPbI₃ α - phase at ambient conditions by improving the tolerance factor and by increasing the formation energy, orthorhombic CsPbBr₃ thermal stability was improved. (b) Histograms represent the formation energy change (ΔE_{form}) for undoped and doped CsPbBr₃, (results based on first principle calculations).¹¹⁵ (c) Schematic illustration showing the perovskite phase stability in relation to I/Br ratio.¹¹⁸

Fig. 1.14(c) illustrates the phase stability versus halide (I/Br) content ratio based on the experimental findings. At an I/Br ratio of 3:1, a distinct separation between the deformed and stable perovskite lattices was seen.¹¹⁸ Yin et al. used the X-site doping method by adding fluorine (F) with an optimum ratio to create bulk-phase heterostructures to improve the phase stability of CsPbI₂Br perovskite. As a result, the carrier lifetimes were prolonged which led to enhanced stability.¹¹⁹ According to Waqas et al. for a stabilized photoactive phase of CsPbX₃ perovskites, the Goldschmidt tolerance factor should be satisfied but the tilting or contraction of perovskite lattice is even acceptable to improve fabricated device parameters.¹²⁰

1.9.2. Light Stability

The light induced phase segregation was observed in OIH perovskites, which made them unstable to UV light. Even this is more serious in mixed-halide perovskites such as MAPbI_{3-x}Br_x and results in the I⁻ and Br⁻ rich domains within perovskite absorber layers.¹²¹ The rearrangement of halides caused by light has also been stated in single halides, such as MAPbI₃ and MAPbBr₃.¹²² Ionic migration and halide segregation owing to residual halides are the two major effects related to light.

1.9.2.1. Photoinduced Halide Segregation

Light-induced halide segregation causes a significant decline in PV characteristics like a decrease in V_{OC}. The photoinduced charge traps lead to charge recombination at the interface of perovskite and CTL which declines the overall performance of the device. To explore the light-independent halide segregation, ion migration and defect formation researchers compared CsPbX₃ and OIH perovskites. Rachel et al. were the first to show that CsPbX₃ perovskites are stable against light, and they recorded photoluminescence (PL) peak positions of various CsPb(I_{1-x}Br_x)₃ compositions under 100 mWcm⁻² as a function of time. It was found that the PL-peak position remained the same for compositions in the range of $0 \leq x \leq 0.4$, representing a wide variety of stable compounds.¹²³

In OIH perovskite films, photo-induced halide segregation has been verified which can be explained by light-enhanced ion migration. Still, in CsPbX₃ perovskite, the photo-induced halide segregation was less severe. The PL spectra for CsPbI₂Br and MAPb(I_{0.5}Br_{0.5})₃ under extremely intense 104 mWcm⁻² illumination are shown in **Fig.**

1.15(a-b) which shows that in CsPbI₂Br perovskite the photo-induced phase segregation was successfully suppressed.

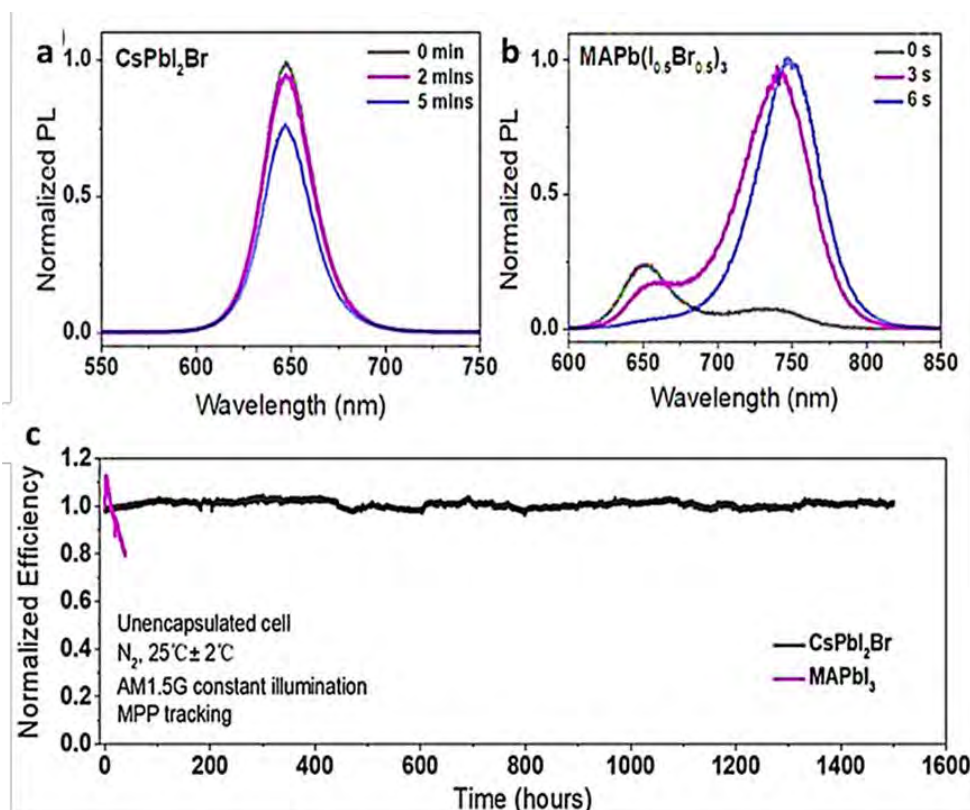


Figure 1.15: PL-spectra of (a) CsPbI₂Br (b) MAPb(I_{0.5}Br_{0.5})₃ (c) MPPT of the CsPbI₂Br and MAPbI₃ based encapsulated PSCs for more than 1500 h.¹²⁴

This suppressed photo-induced phase segregation in CsPbI₂Br perovskite was also confirmed by Zhao et al. and some other researchers.^{124–128} **Fig. 1.15(c)** further demonstrate that CsPbI₂Br is more stable than single halide MAPbI₃ against light-induced phase segregation. Phase segregation under illumination occurs in the CsPb(Br_xI_{1-x})₃ perovskites when $x > 0.4$ and dominant in CsPbIBr₂ ($x = 0.67$) but inhibited in CsPbI₂Br ($x = 0.33$).^{129,130} It is also possible to suppress photo-induced phase separation in CsPb(Br_xI_{1-x})₃ by downsizing to nanocrystals.¹³¹ Thus in all-inorganic perovskites, phase segregation can be prevented by maintaining the halide composition within an acceptable ratio and decreasing the size of the grains.

1.9.2.2. Polaron Formation

Inorganic perovskites have several benefits over hybrid perovskites, such as stability towards light and lattice instabilities in operation, but they linger behind hybrid ones in terms of carrier lifetimes. Furthermore, being volatile, the organic cation also causes carrier recombination at grain boundaries, resulting in the formation of polarons

(having deformed lattices) that surround photogenerated carriers. Zhu et al. inspected that polaron formation is present in OIH perovskites that surround the photo-generated carriers while this phenomenon is absent in CsPbX_3 perovskites.¹³² It has been demonstrated that polaron production and ionic migration are both entirely dependent on organic cations, providing yet another explanation for a potential method of ion transportation under illumination.¹²⁵

1.9.3. Thermal Stability

To meet the commercialization norms and industrial standards CsPbX_3 perovskites should withstand adverse environmental conditions i.e. high solar irradiance and a temperature of up to 85°C at some geographic positions. Particularly, the perovskite absorber layer must be stable under thermal stresses, taking into account both consequences of the annealing that occurs during the synthesis and the operational conditions.

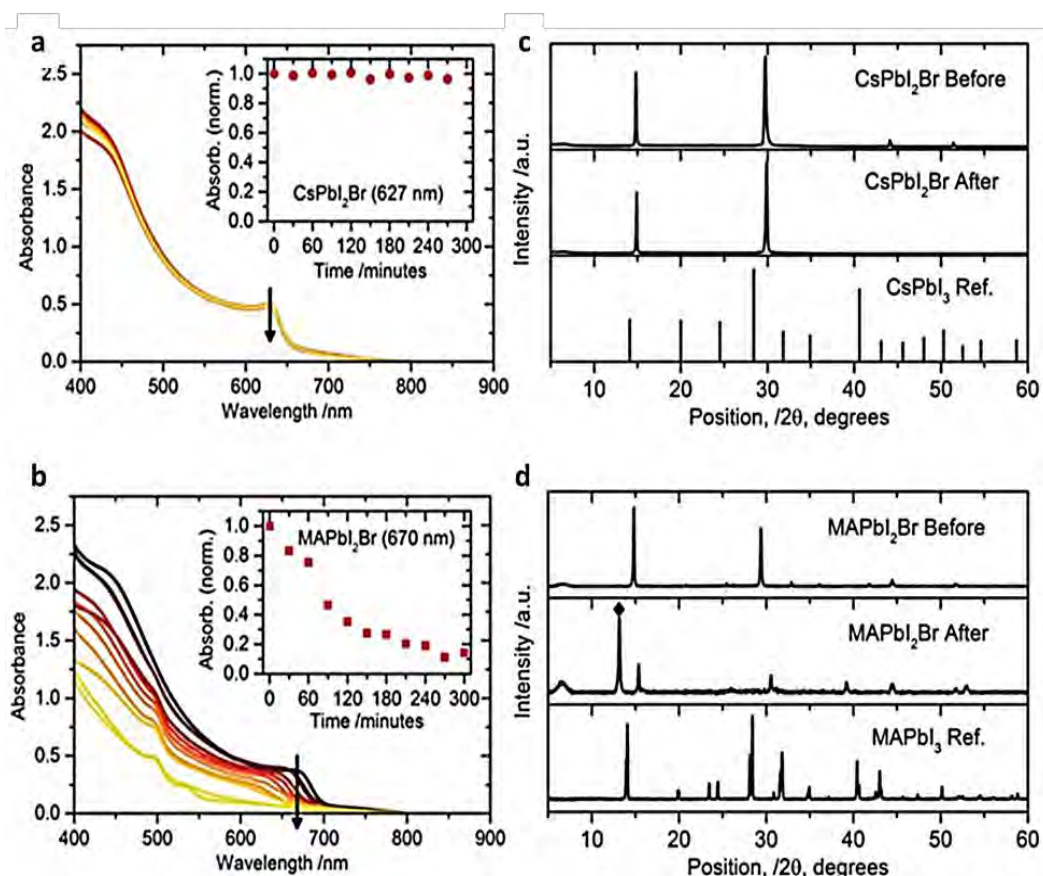


Figure 1.16: Absorption spectra for perovskite absorber layer (a) CsPbI_2Br (b) MAPbI_2Br heated at 85°C for different times. Arrows depict the increase in heating time. Insets show the absorption intensity vs heating time. XRD-spectra for (c) CsPbI_2Br and (d) MAPbI_2Br . The peak of $\text{PbI}_{2-x}\text{Br}_x$ is represented by a diamond symbol.¹⁰⁶

As a consequence of the aforementioned requirements, Snaith et al. investigated the ambient stability of CsPbI₂Br and presented a comparison of the environmental and thermal stability of CsPbI₂Br and MAPbI₂Br perovskites. The XRD and absorption spectra for both perovskite films heated at 85 °C in a humidity range of 20 to 25% were shown in **Fig. 1.16**. In contrast to MAPbI₂Br, where the absorbance reduced continuously at 670 nm and an extra peak appeared in the XRD spectra (represented by a diamond in **Fig. 1.16(d)**), the absorption spectra for CsPbI₂Br were almost the same and without any additional peak in the XRD spectrum illustrating no phase segregation in CsPbI₂Br owing to thermal stress.¹⁰⁶ In continuation to the illustration of CsPbI₂Br perovskite resistance to thermal stress, Silvia et al. also demonstrated that, unlike MAPbI₃, the decomposition of CsPbI₂Br into its component salts is not irreversible but instead it converted to a non-perovskite (yellow) phase with higher bandgap (2.85eV), when exposed to moisture that can be easily reversed when heated at 350°C in moisture free environment.¹³³

As a whole, a comparison of OIH and CsPbX₃ perovskites is discussed with several characteristics pertaining to the light, phase and temperature stability. Although hybrid perovskites have superior intrinsic phase stability, CsPbX₃ perovskites have higher stability against thermal and light stresses. Among CsPbX₃ perovskites, CsPbI₂Br perovskite has demonstrated higher stability against heat, light and phase segregations caused by moisture which improved the stability of the device. However, there are still many loopholes that need further research to be resolved to increase the performance of these PSCs to meet commercialization demands.

1.10. Energetics of Caesium Lead Halide PSCs

1.10.1. Interface Engineering

The stability and efficiency of PSC devices are derived from the charge transfer kinetics, which is the charge transport among various interfaces, notably from perovskite to the CTL. The injection barrier and extraction barrier are the two forms of charge carrier barriers that are present when the perovskite layer is in contact with the electron and hole transport layers. As shown in **Fig. 1.17** the extraction barrier or injection barrier for holes is defined by the energy difference between the VBM of the perovskite and the highest occupied molecular orbital (HOMO) of the HTL and the extraction barrier or injection barrier of electrons is the difference in energy between

the perovskite CBM and the lowest unoccupied molecular orbital (LUMO) of the ETL. The injection barrier restricts the V_{OC} of the device owing to the hole's thermionic loss while the extraction barrier affected FF with no observable effect on V_{OC} of PSC.¹³⁴ Particularly, when the energy levels of perovskite and CTL don't match loss of charge carriers occurs at interface.^{135,136} Since both injection and extraction barriers are detrimental to the performance of PSCs, therefore, to mitigate the energy loss and decrease energy mismatch suitable choice of charge transfer layers with favorable energy level alignment with the perovskite layer is required.

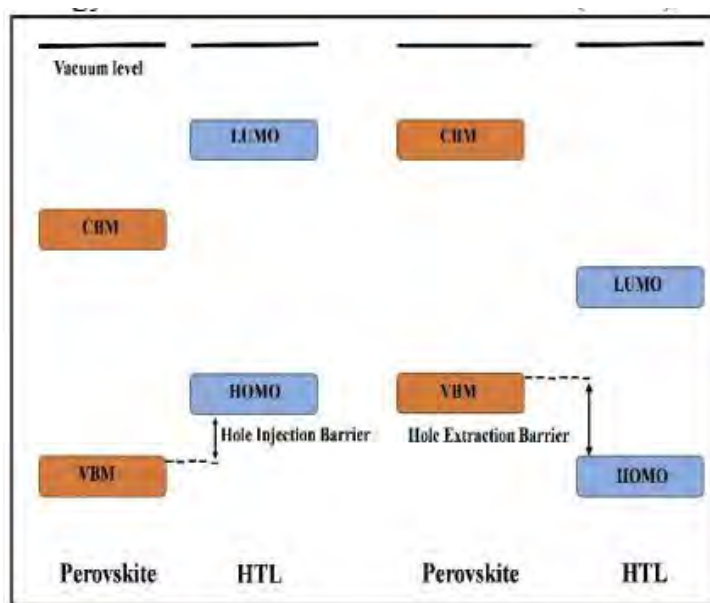


Figure 1.17: Schematics of energy barriers at perovskite/CTL interface.¹³⁴

Jiang et al. revealed that the existence of CsPb_2Br_5 with CsPbBr_3 passivated the grain defects, reduce the carrier recombination and lower the energy barrier. Surprisingly, this self-passivation led to a PCE of 8.34% with improved stability.¹³⁷

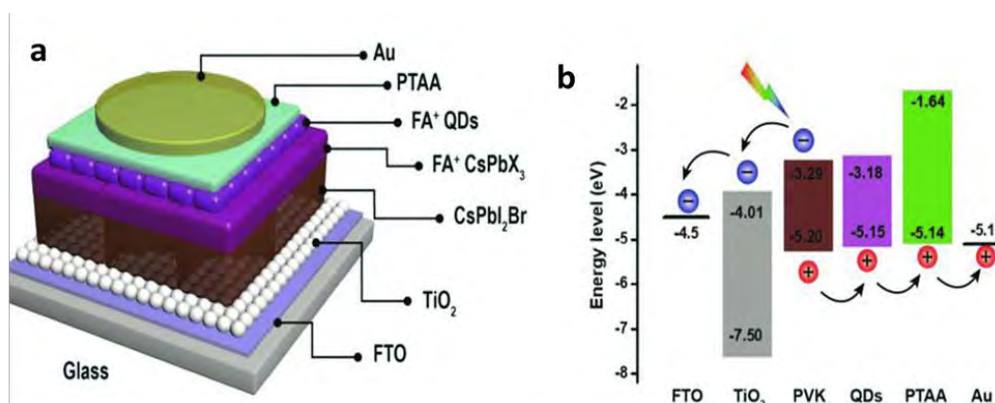


Figure 1.18: (a) Device architecture of fabricated PSC of CsPbI_2Br QDs film post-treated FAI. (b) corresponding energy level diagram.¹³⁸

Recently, the CsPbI₂Br perovskite interface optimized with iodine was reported. In the first step the QDs of CsPbI₂Br were deposited on the top of bulk CsPbI₂Br to form a heterojunction structure. Then the organic iodide salts (PEAI, FAI, MAI, etc.) were used for the post-treatment of the resulting heterojunction perovskite film. **Fig. 1.18(a and b)** represents the architecture of the fabricated device and corresponding energy level diagram which showed improvement in the charge collection property of the resultant PSC upon treatment.¹³⁸ A bilayer ETL (SnO₂/ZnO) was also applied to facilitate electron extraction at the interface in all inorganic planar perovskite devices. The optimized ETL with favorable band alignment with the perovskite layer minimizes the non-radiative recombination with efficient charge extraction.¹³⁹ Furthermore the device exhibited improved stability towards heat and moisture.

There is still a gap within the optimization of interfaces, to further improve the transport and collection of charge carriers. Interface engineering of CsPbX₃ PSCs can further improve the PCE of PSC by improving PV characteristics like FF, and J_{SC}. V_{OC} along with their remarkable environmental and thermal stability makes it easier to fulfill the industrial and commercialization standards.

1.10.2. Defect Passivation

Similar to organic-inorganic hybrid perovskites, the surface traps and bulk defects are also present in the perovskite layer of CsPbX₃ perovskites. These defects were also verified by theoretical calculations and generally arise either due to the limited solubility of precursor salts of perovskite in polar solvents or due to the excessive domains of Pb-X (X= I, Br) after heating at higher temperatures. Recently, a number of approaches have been used by various groups to tackle these issues, which substantially affected the efficiency of the device.⁸⁸¹¹⁵¹⁴⁰ Li et al. reported an increase in the electron cloud density of CsPbI₃ by the addition of PVP into the perovskite layer which decreased the trap density and surface energy. Along with these this strategy also enhance the phase stability and diffusion length of the charge carrier hence leading the all-inorganic CsPbI₃ PSCs towards commercialization.¹⁴¹

Additive engineering was also narrated to reduce the surface defects in CsPbX₃ perovskites. Lead nitrate (Pb(NO₃)₂) was found effective for surface defects passivation of CsPbI₂Br perovskite by improving the hole transfer and decreasing the carrier-trap density.¹⁴² Moreover at lower temperatures, thermodynamically stabilized β -CsPbI₃

was attained via pinhole and surface cracks passivation with choline iodide (CHI). **Fig. 1.19** shows the schematics for perovskite passivation and crack filling of the pristine and control film respectively. The passivation tuned the band alignment and passivates the defects of the perovskite material thus reducing recombination loss and enhancing the charge transport.¹⁴³

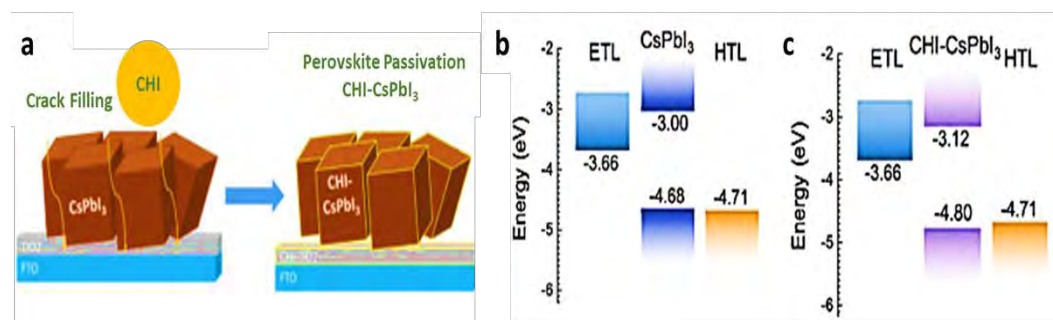


Figure 1.19: (a) Schematic diagram of crack-filling using choline iodide (CHI). Corresponding energy diagram of the fabricated device (e) Pristine and (f) CHI treated.¹⁴³

Apart from the strategies still it is demanding to detect and identify defects and passivate them with innovative approaches to acquire high-quality all-inorganic perovskite absorber material with high carrier lifetime and reduced recombination loss for further improvement in the stability and performance of the device.

1.11. Challenges Regarding All-Inorganic PSC Phase Stability and High PCE

Despite significant progress of CsPbX₃-based PSCs in recent years, there are still several questions related to the phase stability and high efficiency of CsPbX₃ perovskites. According to several theoretical reports on PSC PV parameters (V_{oc} , J_{sc} , FF and PCE) the obtained all-inorganic device parameters are still lower than the theoretical values.^{144,145} This seems to be a great challenge, so optimization of perovskite composition, interfaces of perovskite and CTL is necessary.^{146,147} Thus, more research avenues need to be discovered to improve the intrinsic phase stability and performance of CsPbX₃ PSCs.

1.12. Piezoelectric Nanogenerator (PENG)

A nanogenerator (NG) is an energy harvesting device which convert the harvested energy into useful electrical energy. Based on the nanostructured material used for energy conversion the NG is divided into three main categories i.e. pyroelectric, piezoelectric and triboelectric NG. A PENG is a device that uses active materials that

produce charges when they are mechanically pressed, thus transforming mechanical energy into electricity. The first nanogenerator was developed in 2006 based on the piezoelectric effect utilizing ZnO nanowires.¹⁴⁸

1.12.1. Piezoelectric Mechanism

PENGs typically include electrodes and piezoelectric materials. When the mechanical force is applied on a PENGs polarization occurs and opposite charge is produced on the upper and lower surface of piezoelectric material.

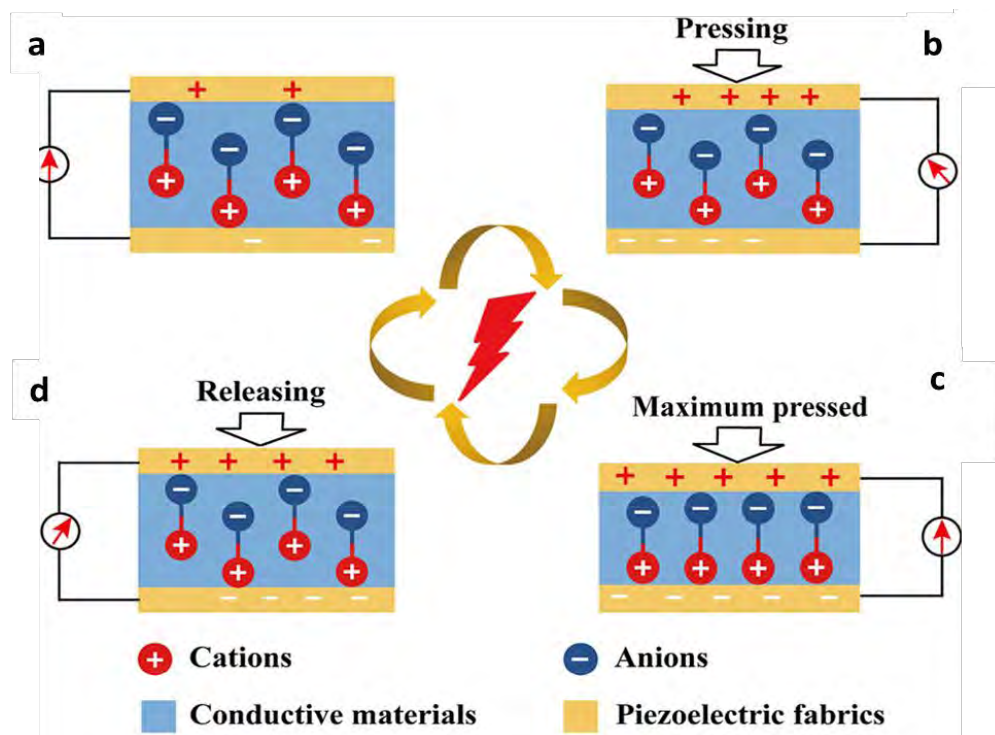


Figure 1.20: Operational mechanism of PENGs.¹⁴⁹

Schematic representation of how the PENGs generate electricity when pressed and released is shown in **Fig. 1.20**. In the first step the ferroelectric domains aligned themselves in the direction of applied magnetic field (**Fig. 1.20(a)**). Strain can be experienced by both cations and anions, but the equivalent center of charge remains unchanged. This means there is no polarization or generation of electric current. When external force is applied on a NG the equivalent center of cations and anions changes and result into the formation of electric dipole which results into piezoelectric potential between oppositely charged electrode as shown in **Fig. 1.20(b)**. Additionally, a current can be seen by connecting the electrodes to an external load. When the gap between the two electrodes is the smallest, the electric polarization density is greatest (**Fig. 1.20(c)**) due to the higher interaction between the electrode and active area. Finally, when the

pressure is released, the electrons revert back to their initial state as displayed in **Fig. 1.20(d)**. Consequently, a reversed piezoelectric electric current can be seen.¹⁴⁹

When the ZnO material is used in PENG the similar mechanism occurs. In the wurtzite-structured ZnO crystal, the arrangement of tetrahedrally coordinated Zn^{2+} and O^{2-} ions occurs in a layered manner along the c -axis as displayed in **Fig. 1.21(a)**.

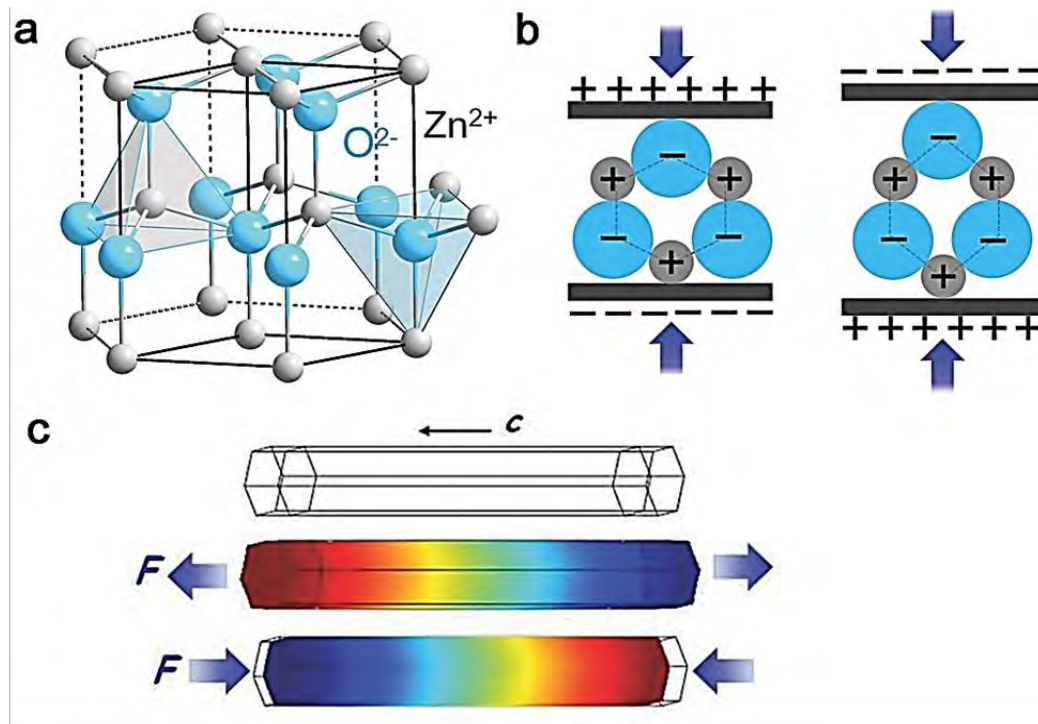


Figure 1.21: (a) Wurtzite-structured ZnO (atomic model). (b) Piezoelectric characteristics and different piezopotentials in the material's tension and compression modes. (c) Theoretical calculation of the distribution of piezoelectric potential under axial strain in a ZnO nanowire.¹⁵⁰

When a mechanical force is applied ZnO crystal, it will deform and an electric dipole is generated by the separation of cations and anions resulting in the development of a piezo potential shown in **Fig. 1.21(b)**. When an external load is applied to this deformed crystal, the movement of free electrons occurs through the external circuit, to partially screen the piezo potential and attain a new state of equilibrium (**Fig. 1.21(c)**) which is the process for energy conversion. Hence, by continuously modifying the piezopotential through a dynamic straining phenomenon, the fundamental operating principle of the nanogenerator involves a consistent flow of pulse current passing through the external circuit. Other PENGs employing different piezoelectric materials such as PZT, PVDF and BaTiO_3 (BTO) can also be powered by using the same basic model and principle.¹⁵⁰

1.13. Hybrid Devices for Harvesting Multi-Type Energies

Our living environment is abundant with a diverse range of energy sources, encompassing mechanical, solar, thermal, chemical, and biological energy, providing us with an abundance of diverse energy options. In order to fulfill the global energy demands and achieve the self-sustaining and environmentally-friendly operation of micro/nanosystems, several energy harvesting devices have been developed to generate electricity from the surrounding environment. Each energy harvesting device utilizes different methods and captures specific types of energy, while all other types remain unused. A solar cell, for instance, cannot be used in regions where sunlight is not present because it is only intended to produce power under light illumination. Therefore, there is a strong need to develop a hybrid device (HD) that can efficiently convert multiple forms of energy into electricity. This would allow us to fully utilize the available energy sources and power systems anytime and anywhere.¹⁵¹

In order to maximize the utilization of energy from the environment, Wang's group in 2009 proposed the concept of a hybrid cell which can harvest both mechanical and solar energy.¹⁵² This innovative approach enables the simultaneous harvesting of multiple forms of energy using a single device. Thus sets the foundation for the fabrication of hybrid harvesters and opens up new possibilities in the field of energy harvesting.

1.14. Problem Statement

When moving photovoltaic technology from the laboratory to commercial scale, it is essential to give utmost importance to three key metrics: cost-effectiveness, high PCE, and prolonged stability to ensure a durable product lifespan. OIH perovskites have received immense attention as most promising photovoltaic materials due to high efficiency and low cost, but their practical applicability is still hampered due to the short device stability. As an alternative all-inorganic perovskite based on caesium exhibit superior light, moisture, and thermal stability, offering a potential route to stable PSCs. Till now different categories of inorganic perovskite has been used but CsPbX₃ series have achieved higher performances than others series. Furthermore, numerous studies have demonstrated that CsPbX₃ series exhibit comparable optoelectronic characteristics to their organic inorganic hybrid counterparts. Among CsPbX₃ perovskites, CsPbI₂Br perovskite has demonstrated higher stability against heat, light and phase segregations caused by moisture which increased the stability of the device. Although the stability

of CsPbI₂Br PSCs surpasses that of hybrid perovskite devices, but their PCEs still lower than their hybrid perovskite counterparts. This low performance of CsPbI₂Br-based devices could be attributed to the poor quality of the film, which results into defects and structural imperfections like grain boundaries and dislocations. These defects hinder charge transport and cause variations in light absorption and exciton generation within the film, ultimately reducing device stability and performance. Furthermore, the poor film quality can also lead to increased trap density, which can trap charge carriers and reduce their mobility, leading to lower charge transport efficiency which ultimately diminish the device performance.

So high quality CsPbI₂Br perovskite film is a prerequisite to fabricate high performance PSC. Therefore, a simple, low-cost, high-quality film deposition techniques and optimization methods is highly desirable which can improve the stability, reduce the defects and traps, lead to efficient charge transport and collection and provide favorable energy level alignment for further development of inorganic PSCs. So, there are still many loopholes that need further research to be resolved to increase the PCE of these PSCs to meet commercialization demands.

1.15. Aims of Research

This research work aims to address the aforementioned issues by introducing different methodologies to improve the stability and quality of the CsPbI₂Br perovskite film to enhance the performance and stability of inorganic PSCs.

1.16. Plan of Work

In order to accomplish the stated objective a research plan was developed which encompasses the following approaches:

1. Selection of suitable deposition methods, optimization of CTLs (NiO_x and C₆₀) and absorbing layer (CsPbI₂Br) to achieve working PSCs.
2. Compositional engineering of the CsPbI₂Br perovskite material to minimize the defects and to enhance the stability of perovskite material.
3. Surface treatment of CsPbI₂Br to modify the interface between perovskite/HTL and to improve the perovskite film quality.
4. Lewis base passivation of CsPbI₂Br perovskite to minimize the defect states in the perovskite material.

5. Characterization of the modified perovskite and use it for the fabrication of the PSC and analyze their performance.
6. Fabrication of hybrid harvester devices for sustainable energy harvesting.

2. Materials and Methodology

This chapter outlines the experimental methodologies and measurement techniques employed in this research. It commences with a brief introduction of deposition techniques followed by the details of solutions and methods for HTL, ETL and perovskite film formation used for device fabrication. Additionally, different characterization methods for the characterization of films and fabricated devices are also illustrated in this chapter.

2.1. Materials

All the chemicals required for the fabrication of PSC devices were purchased from Sigma-Aldrich, CreaPhys, Great Cell Solar, and TCI, stored in the glove box and used as received. The chemicals include nickel(II) acetylacetonate (Sigma-Aldrich), zinc acetate (Sigma-Aldrich), caesium iodide (Sigma-Aldrich), lead iodide (Sigma-Aldrich), lead bromide (Sigma-Aldrich), copper bromide (Sigma-Aldrich), lithium fluoride (Sigma-Aldrich), 2-amino ethanol (Sigma-Aldrich), 2-methoxy ethanol (Sigma-Aldrich), ethylene diamine (Sigma-Aldrich), poly (methyl methacrylate) (Sigma-Aldrich), polyvinylpyrrolidone (Sigma-Aldrich), hexamethylenetetramine (Sigma-Aldrich), methyl ethyl ketone (Sigma-Aldrich), dimethyl sulfoxide (Sigma-Aldrich), isopropanol (Sigma-Aldrich), hydrochloric acid (Sigma-Aldrich), acetonitrile (Sigma-Aldrich), chlorobenzene (Sigma-Aldrich), C₆₀ (CreaPhys), Spiro-O-MeTAD (Greatcell Solar), bis (tri fluoro methane) sulfonimide lithium salt (TCI), 4-tert-butylpyridine (TCI).

2.2. Deposition Techniques for PSCs Fabrication

PSCs were fabricated by using spin coating and thermal evaporation methods. A generalized overview of these methods is given below.

2.2.1. Spin Coating Method

The spin coating technique is used to fabricate thin films with thicknesses ranging from micrometers to nanometers. It involves the mounting of substrate on the chuck which rotates the sample and causes the liquid to be violently propelled outward by centrifugal force. Smooth deposition on the surface is primarily facilitated by the viscous force and surface tension. Ultimately, evaporation leads to the formation of a thin film. A schematic diagram of the spin coating process is shown in **Fig. 2.1**.

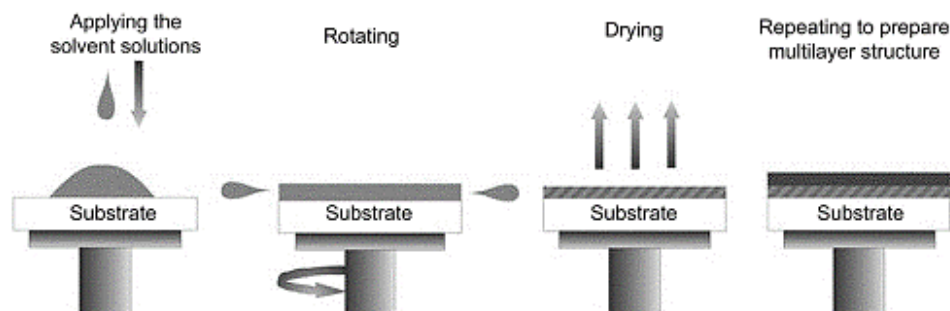


Figure 2.1: Schematic diagram of the spin-coating process.¹⁵³

The steps involved in the spin-coating process are given below.

- i. The substrate is placed on the spin coater's chuck. Rotating time and speed are adjusted by built-in controlling time and speed functions.
- ii. The precursor solution is dropped on the substrate by a micro-pipette.
- iii. The substrate is rotated at a certain speed (rpm) and duration to form a thin film.

The thickness of the film is influenced by the spin speed while uniformity of the film is related to spin time. Other factors like solvent vapor pressure, boiling point and environmental conditions (humidity and temperature) are also crucial.

2.2.2. Thermal Evaporation

This method involves the evaporation of desired material by heating under a vacuum below 1×10^{-6} torr (1.3×10^{-4} Pa) to produce some vapor pressure. Due to low pressure inside the chamber materials start to vaporize at the sublimation temperature. Depending on the evaporating material the tantalum, molybdenum or tungsten coil or boat will be used to evaporate the source material i.e., it should not react with the material. Rotary and diffusion pumps are used to generate a high vacuum and evaporation rate is influenced by the temperature of the source material and regulated by varying current of the heating element. Since the substance is heated to its melting point and is liquid during this process thus placed in an upright position at the bottom of the chamber. The vapor stream of the evaporated material rises upward towards the top of the chamber and condenses on the substrates that are held inverted in an appropriate fixture to form a coating or film. Film thickness is determined by a thickness monitor usually a microbalance quartz crystal coated with gold.¹⁵⁴ The schematic diagram of the thermal evaporation process is shown in **Fig. 2.2**.

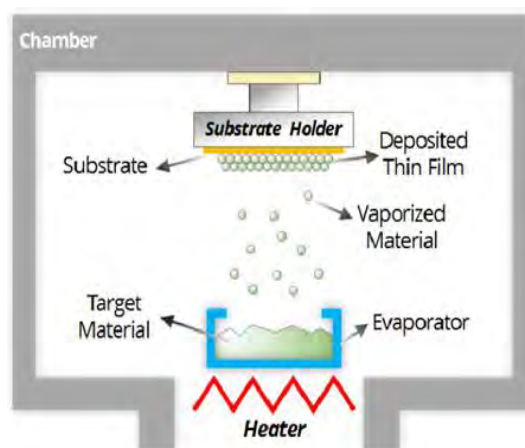


Figure 2.2: Schematic of thermal evaporation deposition technique.¹⁵⁵

2.3. Fabrication of PSC Devices

2.3.1. Fabrication of Inverted PSC Devices

Inverted PSCs were fabricated with a device configuration of ITO/NiO_x/Perovskite/C₆₀/LiF/Cu shown in **Fig. 2.3**. Firstly, nickel oxide (NiO_x) HTL layer was deposited on indium tin oxide coated glass substrate (ITO) using the spin coating method followed by spin coating of the perovskite layer. Subsequently, the [6,6]-C₆₀-butyric acid methyl ester (C₆₀) ETL was deposited on top of the perovskite layer using a thermal evaporation process. Finally, a lithium fluoride (LiF) buffer layer and a copper (Cu) electrode were consecutively thermally evaporated onto the C₆₀ layer. A detailed description of the device fabrication process is given below.

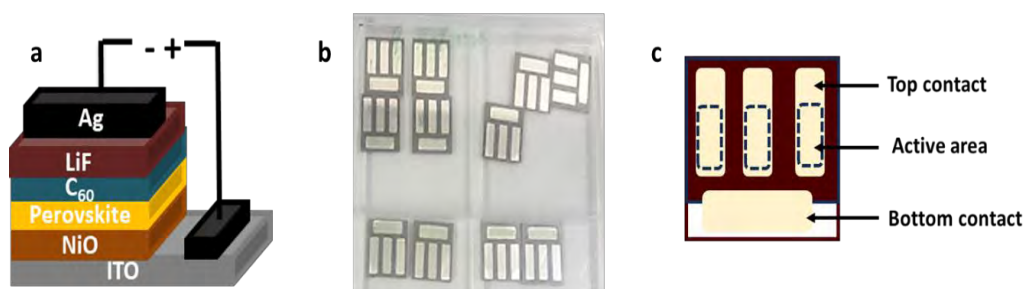


Figure 2.3: (a) Diagrammatic representation (side view) of fabricated inverted PSC showing different layers. (b) Fabricated PSC devices. (c) Top view showing top and bottom contact with active area.

2.3.1.1. Substrate Cleaning Procedure

The ITO (sheet resistance $14 \Omega/\square$, 1 mm thick) were etched by using 37% hydrochloric acid (HCl) and zinc powder and cut into suitable size ($14 \times 14 \text{ mm}^2$). After that, the glass and ITO substrates were cleaned via sonication in a soap water, distilled water, acetone,

and isopropanol for 5 minutes in each solvent and then dried under N₂ flow. Subsequently, ITO substrates were subjected to UV-ozone treatment for 15 minutes. Different steps for substrate preparation are shown in Fig. 2.4.

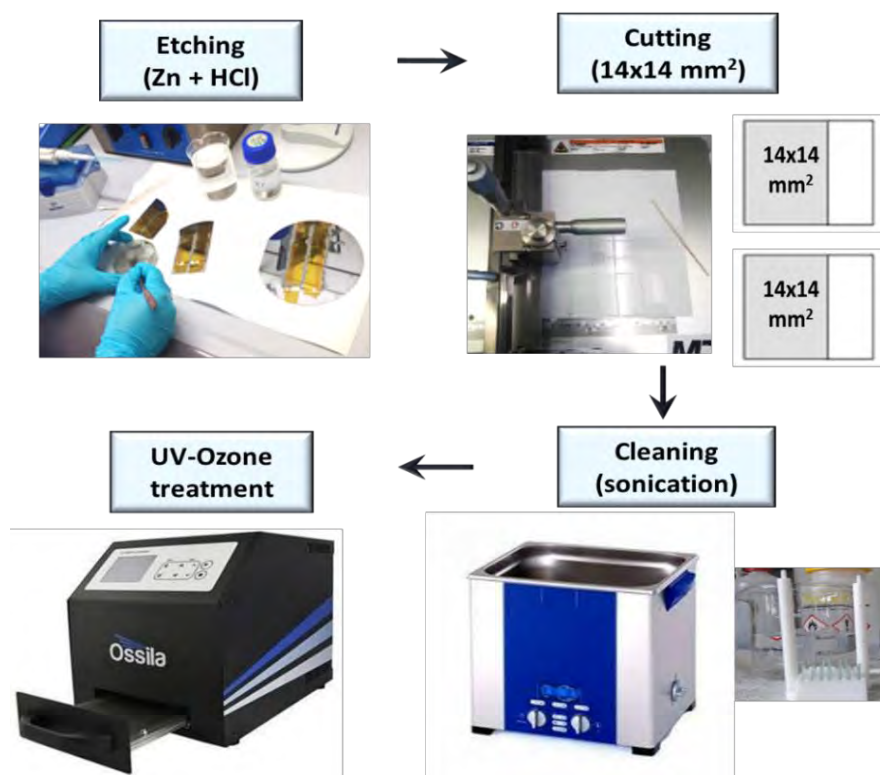


Figure 2.4: Steps for the preparation of the substrate.

2.3.1.2. Preparation of NiO_x Films

Solution process method was used for the fabrication of NiO_x films. For this, the precursor solution for NiO_x was prepared by dissolving nickel(II) acetylacetonate (C₁₀H₁₄NiO₄) (129 mg) in anhydrous ethanol (5 mL) and HCl (37%, 50 μL) and stirred overnight which yielded a green color solution. Then, the NiO_x precursor solution was filtered with a 0.45 μm PTFE membrane filter. Afterward, the NiO_x film was deposited in ambient conditions on the top of ITO substrates by spin coating the NiO_x precursor solution at 5000 rpm for 30 s followed by drying at 100 °C for a minute. To clean contact area, a cotton swab dipped in ethanol was used to wipe a 2-3 mm edge of the NiO_x layer. Then, the films were annealed at 360 °C for 45 minutes in ambient conditions for the fabrication of NiO_x films.¹⁵⁶

2.3.1.2.1. Surface Treatment of NiO_x Films

The NiO_x films were treated with plasma for twenty seconds to improve the wetting properties of the top perovskite film. The treated NiO_x films were immediately

transferred to a glovebox with controlled oxygen and moisture level (less than 5 ppm) for further processing to complete the device fabrication. **Fig. 2.5** depicts different steps for the preparation and post-treatment of NiO_x films.

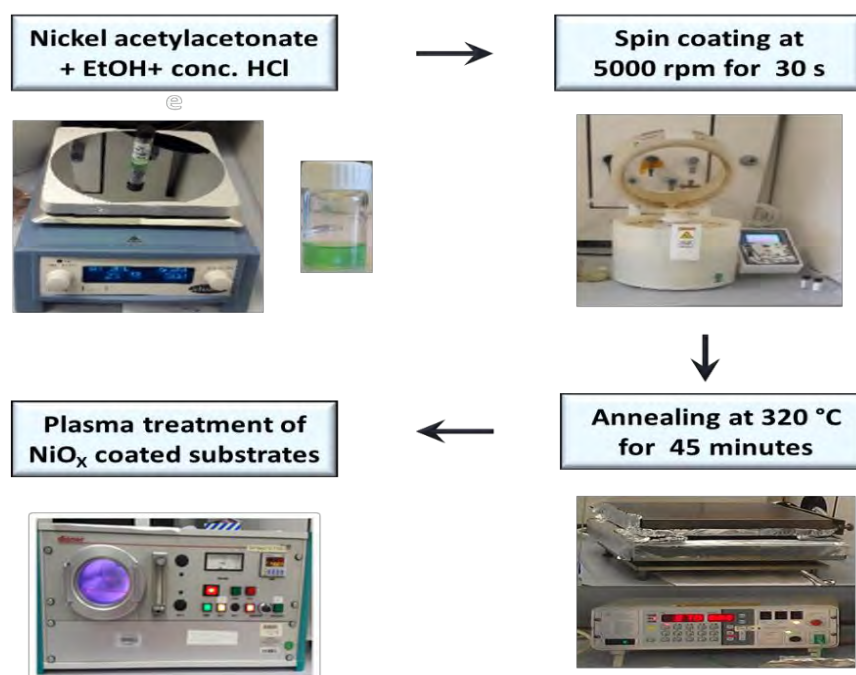


Figure 2.5: Steps showing the preparation and post-treatment of NiO_x films.

2.3.1.3. General Procedure for the Fabrication of Perovskite Films

The precursor solution for perovskite was prepared by mixing perovskite precursor salts in 1 mL of anhydrous dimethyl sulfoxide (DMSO) with continuous heating at 70 °C until a complete clear solution was formed.

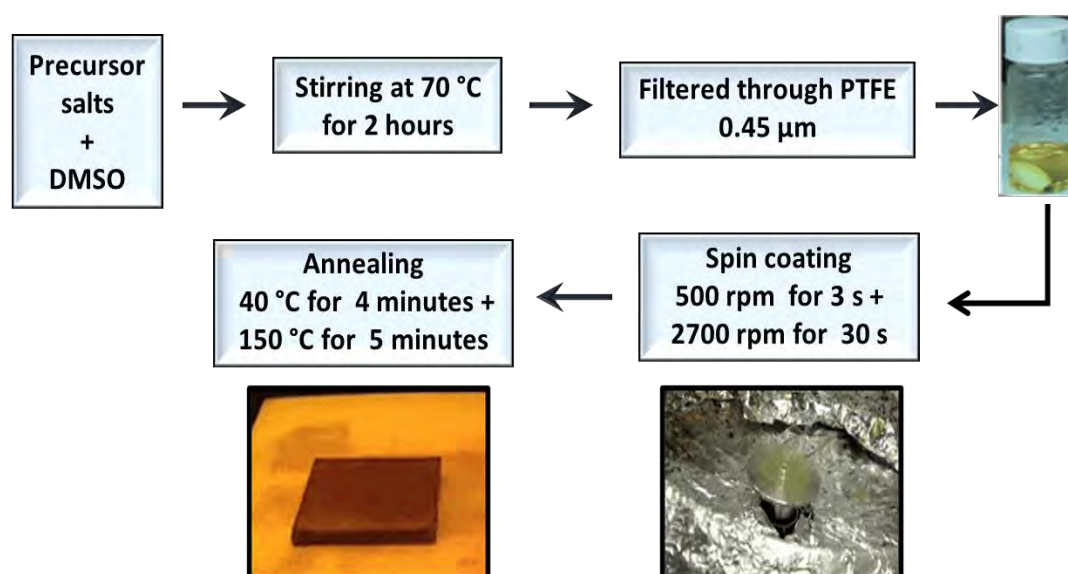


Figure 2.6: Schematics showing the preparation of perovskite films.

Before processing into devices, the prepared perovskite precursor solution was filtered with a 0.45 μm PTFE membrane filter. The perovskite film was fabricated on NiO_x coated ITO substrates by spin-coating perovskite precursor solution (45 μL) at 500 rpm for 3 s and 2700 rpm for the 30 s. The films were annealed on a hotplate at 40 $^\circ\text{C}$ for 4 minutes and 150 $^\circ\text{C}$ for 5 minutes to complete the crystallization of perovskite film. The general method for the preparation of perovskite films is shown in **Fig. 2.6**.

2.3.1.3.1. Preparation of CsPbI_2Br Perovskite Films

The precursor solution for perovskite was prepared by mixing 313 mg of caesium iodide (CsI), 277 mg of lead iodide (PbI_2), and 220 mg of lead bromide (PbBr_2) in 1 mL of DMSO. The CsPbI_2Br films were fabricated by following the above-mentioned general method.

2.3.1.3.2. Preparation of Non-Stoichiometric $\text{CsPb}_{1-x}\text{I}_{2-x}\text{Br}$ Perovskite Films

The precursor solution for perovskite was prepared by dissolving 313 mg of CsI, 227 mg of PbI_2 , and 220 mg of PbBr_2 in 1 mL of anhydrous DMSO and the above-mentioned general procedure was followed for the fabrication of films.

2.3.1.3.3. Preparation of Cu Doped $\text{CsPb}_{1-x}\text{I}_{2-x}\text{Br}$ Perovskite Films

For the preparation of 5% Cu doped $\text{CsPb}_{1-x}\text{I}_{2-x}\text{Br}$ perovskite 313 mg of CsI, 227 mg of PbI_2 , 198 mg of PbBr_2 and 13.4 mg of copper bromide (CuBr_2) were mixed in 1 mL DMSO. For 3% Cu doping 207 mg of PbBr_2 and 8.04 mg of CuBr_2 were used whereas for 2% Cu doping 211 mg of PbBr_2 and 5.36 mg of CuBr_2 were utilized, along with the same amounts of CsI and PbI_2 . Perovskite films were fabricated by employing a general recipe described earlier.

2.3.1.4. Isopropanol Post-Treatment of CsPbI_2Br Perovskite Films

In the case of IPA-treated film the perovskite deposited substrates were dipped in isopropanol (IPA) solvent for different times (5, 10 and 15 minutes). After that, the films were dried at 40 $^\circ\text{C}$ for 3 minutes to ensure the complete removal of the solvent.

2.3.1.5. Ethylene Diamine Treated CsPbI_2Br Perovskite Films

In the case of surface modification via Lewis acid-base passivation method simplest Lewis-base ethylene diamine (EDA) was used. For this purpose, the 30 μL of 0.009% solution of EDA in chlorobenzene was spin-coated at the top of the perovskite layer at

3000 rpm for the 30 s.

2.3.1.6. Preparation of C₆₀, LiF Layers and Cu Contacts

The perovskite-coated substrates were transferred into a glovebox fitted with a thermal evaporator (UNIVEX 350 G, Leybold). After that, the pressure inside the chamber of the thermal evaporator is reduced to 5×10^{-6} mbar by pumping for 20 minutes. Then, the C₆₀ layer of different thicknesses (10 to 45 nm) was thermally evaporated with an evaporation rate of 0.2 Å/s to form an electron-selective contact. Subsequently, a 1 nm LiF buffer layer was evaporated on the top of the C₆₀ layer at the rate of 0.04 Å/s. The substrates were then taken out from the thermal evaporator to anneal at 80 °C for 10 minutes under a nitrogen environment. Finally, the Cu contacts (80 nm) were evaporated at a rate of 1 Å/s. The active area of the PSCs was 0.133 cm² which was defined by a measurement mask.

2.3.2. Fabrication of Normal PSC Devices

Normal PSCs devices were fabricated with a device configuration PET/ITO/ZnO/Perovskite/SpiroOMeTAD/Au shown in **Fig. 2.9(b)**. Firstly, zinc oxide (ZnO) nanorods as an ETL layer were synthesized on ITO-coated polyethylene terephthalate (PET/ITO) substrate followed by spin coating of the perovskite layer. Subsequently, the spiro-O-MeTAD (spiro) HTL was deposited on top of the perovskite layer using a spin coating method. Finally, a gold (Au) electrode was thermally evaporated onto the spiro layer. Below is a detailed description of the device fabrication process.

2.3.2.1. Substrate Cleaning Procedure

PET/ITO substrates were cut into suitable sizes (150x 250 mm²). After that, the PET/ITO substrates were cleaned via sonication in a soap water, distilled water, acetone, and isopropanol for fifteen minutes respectively. Then, a nitrogen gun was used to dry the substrates under nitrogen flow. Afterward, the substrates were subjected to plasma treatment for 15 minutes.

2.3.2.2. ZnO Nanorods Synthesis

ZnO nanorods were synthesized on PET/ITO substrate by following a reported method with slight modification.¹⁵⁷ Schematic representation of steps for ZnO nanorods synthesis is shown in **Fig. 2.7** For ZnO nanorod synthesis, a ZnO seed layer was

deposited on the top of the ITO/PET substrate via spin coating method. The seed layer precursor solution was prepared by dissolving 219 mg of zinc acetate ($\text{Zn}(\text{CH}_3\text{COO})_2 \cdot 2\text{H}_2\text{O}$) and 61.08 mg of 2-amino ethanol ($\text{NH}_2\text{CH}_2\text{CH}_2\text{OH}$) in 10 mL of 2-methoxy ethanol ($\text{CH}_3\text{OCH}_2\text{CH}_2\text{OH}$) and stirred overnight. Then, the precursor solution was filtered with a $0.45 \mu\text{m}$ PTFE membrane filter. Afterward, the ZnO seed layer was deposited on the top of the PET/ITO substrate by spin coating the precursor solution at 500 rpm for 10 s and 3000 rpm for 30 s, followed by annealing at 140°C for 30 minutes and subsequently cooled to room temperature. This process was repeated five times and during the second, third and fourth times, the film was heated at 140°C for 15 minutes.

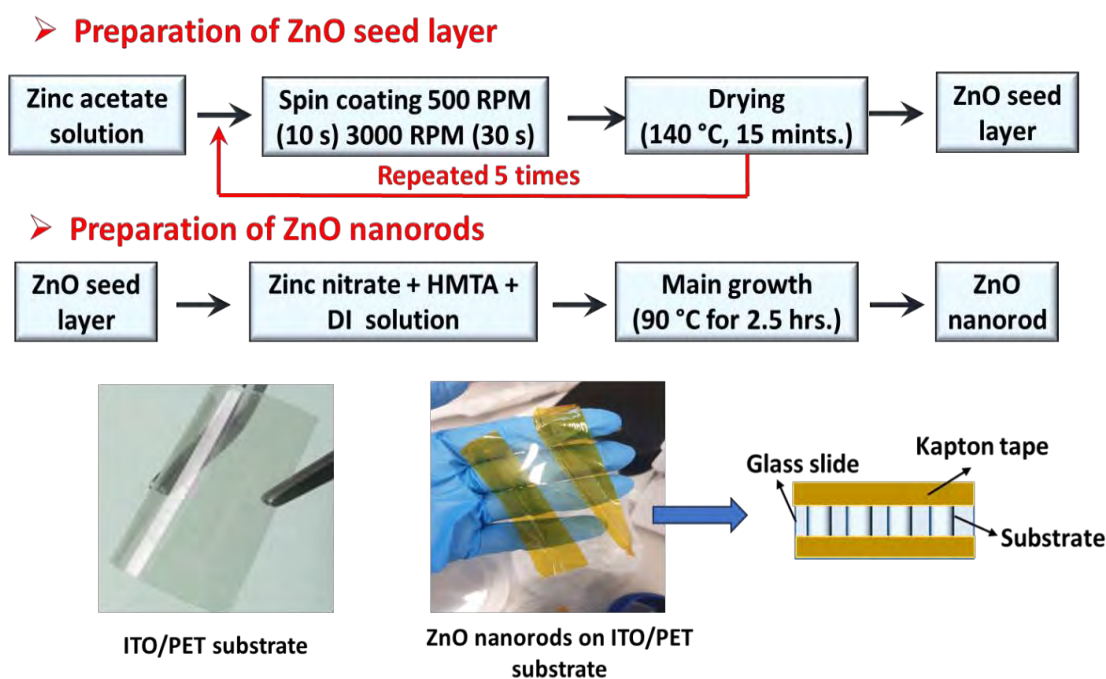


Figure 2.7: Steps showing the synthesis of ZnO nanorods.

Then the coated substrates were fixed to a microscope slide by the Kapton tape and dipped into solution in a closed container. The solution was prepared by mixing 1.86 g of zinc nitrate ($\text{Zn}(\text{NO}_3)_2$) and 0.88 g of hexamethylenetetramine ($\text{C}_6\text{H}_{12}\text{N}_4$) in 200 mL of deionized water. After that, the container was placed in a preheated oven at 90°C for 2.5 hrs. Finally, the substrates were rinsed with deionized water and dried at 80°C .

2.3.2.2.1. Surface Treatment of ZnO Nanorods

The ZnO nanorods were treated with plasma for fifteen minutes to improve the wetting properties of the top perovskite film. The treated substrates were immediately

transferred to a glovebox with controlled oxygen and moisture level (less than 5ppm) for the fabrication of perovskite film.

2.3.2.3. Preparation of Perovskite Films

The perovskite precursor solution was prepared by mixing 313 mg of CsI, 227 mg of PbI_2 , and 220 mg of PbBr_2 in 1 mL of anhydrous DMSO with continuous stirring at 70 °C until a complete clear solution was formed. Then the solution was filtered with a 0.45 μm PTFE membrane filter. Afterward, 7.6 mg, 11.4 mg and 15.2 mg polyvinylpyrrolidone (PVP) was added to the perovskite precursor solution with continuous stirring at 70 °C for 1%, 1.5% and 2% PVP-incorporated perovskite respectively. For the fabrication of perovskite film shown in **Fig. 2.8** 90 μL of perovskite precursor solution was spin coated on ZnO coated PET/ITO substrate inside the glove box at 500 rpm for 3 s and 2700 rpm for the 30 s. The deposited films were firstly annealed at 40 °C for 4 minutes and 150 °C for 5 minutes.

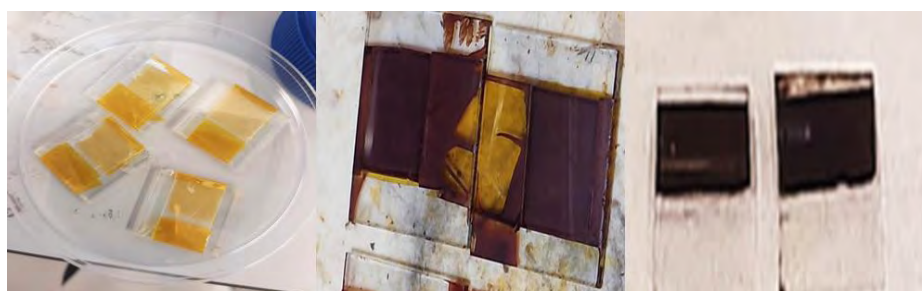


Figure 2.8: Perovskite film fabricated on ZnO nanorods.

2.3.2.4. Preparation of Spiro Layer, Au Contacts and Device Encapsulation

The solution of HTM was prepared by mixing 72.3 mg of spiro with 1 mL anhydrous chlorobenzene with continuous stirring until a complete clear solution was formed. After that, 17.5 μL of bis (tri fluoro methane) sulfonimide lithium salt (Li- 3 TFSI) solution in acetonitrile (520 mg/mL) and 28.8 μL of 4-tert-butylpyridine (tBP) was added and stirred. Then the solution was filtered using a 0.45 μm PTFE filter and then applied onto the perovskite films through spin-coating at 3000 rpm for a duration of 20 s. Solution of poly (methyl methacrylate) (PMMA) in methyl ethyl ketone (MEK) was coated on the left corner of substrate, to prevent short circuits. After that, an Au electrode of 150 nm thickness was deposited on the top of the spiro layer by thermal evaporation (E306A, Edwards) with an evaporation rate of 1 $\text{\AA}/\text{s}$. Afterward, the flat copper strips were stuck to the ITO and Au layer as the electrode using conductive silver

adhesive epoxy followed by soldering of copper wires to the copper strips (**Fig. 2.9(a)**). Then, the device was encapsulated in a laminating pouch by using hot press (**Fig. 2.9(c)**). The active area of device is 0.25 cm^2 .

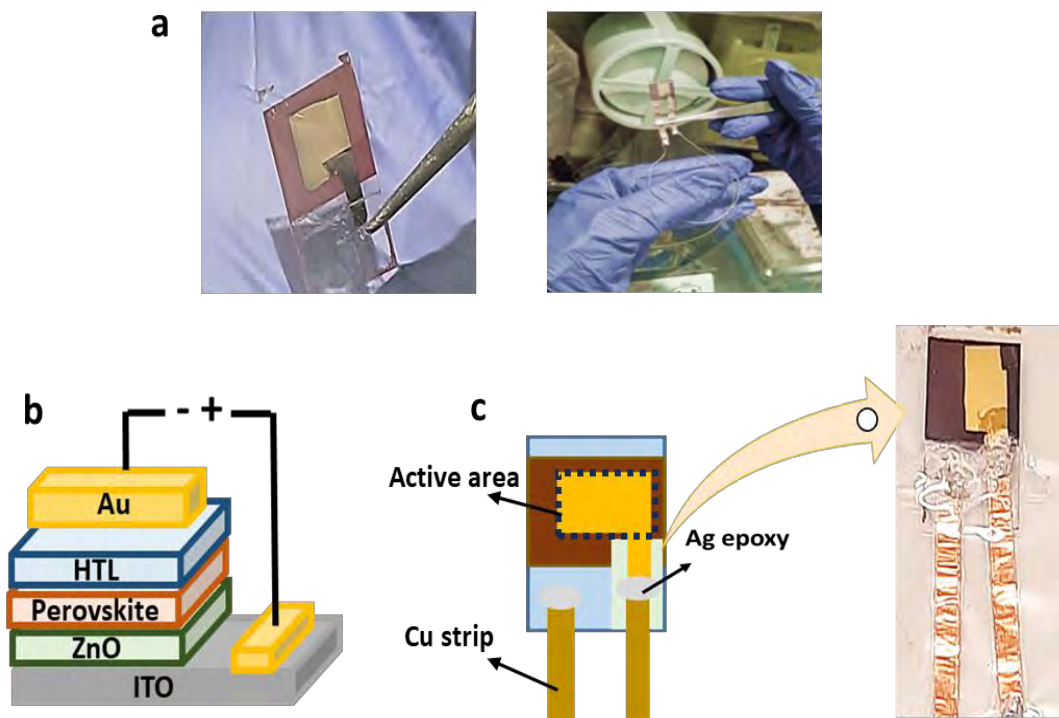


Figure 2.9: (a) Thermal evaporation of Au and Cu strips attached to ITO and Au electrode. (b) Diagrammatic representation of side view of fabricated hybrid device showing different layers. (c) Top view of fabricated hybrid device.

2.4. Characterization Techniques

2.4.1. Techniques for Perovskite Film Characterizations

This section explains the techniques employed for characterizations of fabricated perovskite films used for the fabrication of PSC devices.

2.4.1.1. X-ray Diffraction (XRD)

The X-ray diffraction studies of the thin films were investigated under ambient condition using an X-ray diffractometer Bruker D8 Discover equipped with Lynxeye XE detector, and Cu $K\alpha$ radiation source was used.

2.4.1.2. X-ray Photoelectron Spectroscopy (XPS)

In our study, the XPS measurements were performed using a standard Omicron system with Al K-alpha X-rays (1,486.7 eV). C1s core level was used for the calibration of data.

2.4.1.3. Photoluminescence (PL) Spectroscopy

A FluoTime 300 from PicoQuant was used to record PL spectra of thin films. The samples were excited with a 485 nm laser illumination source. A filter of 575 nm was inserted between the detector and sample to block reflected and scattered laser beams. To get insights into the time-resolved photoluminescence (TRPL), lifetime transients were recorded using time-correlated single-photon counting (TCSPC) mode.

2.4.1.4. Scanning Electron Microscopy (SEM)

The SEM images of perovskite thin films were obtained using Zeiss Crossbeam 1540XB FESEM to study the morphology of the perovskite film. An accelerating voltage of 5 kV was used for imaging. The EDX spectrum was generated using a 15 kV electron beam.

2.4.1.5. Photoelectron Spectroscopy in Air (PESA)

PESA is a technique used to examine the work function of a surface. The light from a deep, wide-band ultraviolet (UV) source is focused by a monochromator into a small spot on the sample. Electrons at particular energy levels will be produced because of the photoelectric effect that is associated with the work function of the surface. In current studies, a low photoelectron energy of 3-6 eV was used to determine the valence band position of perovskite samples by using the AC-2 instrument (Riken Instruments).

2.4.1.6. Ultraviolet-Visible (UV-Vis) Spectroscopy

The UV-Vis absorption spectra for the perovskite films were acquired using a Perkin Elmer Lambda 950 UV-Vis spectrometer.

2.4.1.7. Contact Angle Measurement

To reveal the wettability of water on perovskite substrates sessile drop method was used for contact angle measurement. The setup consists of a camera and an elevated stage on which the substrates were placed. The positions of the camera and stage were kept constant throughout the measurement so that images were obtained at the same angle, enabling comparison of the data. A water droplet was placed on the surface of a substrate, and an image was then captured. ImageJ software was used to analyze the images and to measure the contact angle. In current studies, contact angle measurements were carried out by using a contact angle goniometer (DSA100 KRUSS).

2.4.1.8. Atomic Force Microscopy (AFM)

In AFM surface topology and roughness were evaluated. The information is collected by touching or feeling the sample surface with a mechanical probe. For imaging, the reaction between the probe and the force that the sample executes on the probe will be used to create a high-resolution image of the topography of a sample surface.¹⁵⁸ In our study, the topographical imaging was done by employing the tapping mode using Bruker Dimension Icon with ScanAsyst instrument.

2.4.2. Characterization Methods for PSCs

2.4.2.1. Current Density Voltage (J-V) Characteristics

The J-V curves of the solar cell were measured under nitrogen in the glove box. To compute the associated current, a biasing voltage is applied to the solar cell ranging from a negative potential (reverse biasing) to a positive potential (forward biasing). The current density (J), which is drawn against the applied voltage (V), is obtained by dividing the current by the active area. From the J-V curve, other photovoltaic parameters such as J_{sc} , V_{oc} , FF and PCE were calculated, as explained in **section 1.6**. In current studies, the J-V characteristics of inverted PSCs were measured using a Keithley 2400 Source Meter, a KG5 filter, and a Fraunhofer ISE-certified Si reference diode in an N₂-filled glovebox. LOT 300 W Xenon solar simulator was used to illuminate the cells through a shadow mask producing an active area of 0.133 cm². Maximum PowerPoint (MPP) tracking algorithm, developed by Zimmermann et al.¹⁵⁹ was employed for a reliable measurement. The J-V curve was measured by a step size of 10 mV and a sweep rate of 50 mV/s. In case of hybrid device, the J-V characteristics of solar cell were measured in ambient conditions using a Ossila unit-200 Source Meter, a 1.5 AM filter and a ORIEL Si reference cell. A class AAA, 150 W, Sciencetech solar simulator was used to illuminate the cells.

2.4.2.2. External Quantum Efficiency (EQE)

In this method, a solar cell is exposed to monochromatic light, and the resulting current is determined. From the EQE we can calculate the J_{sc} of the solar cell. First the EQE (λ) for all the wavelengths is multiplied with radiation flux $\Phi(\lambda)$ followed by its integration over the entire wavelength range which yields the J_{sc} value according to the equation 2.1.

$$J_{sc} = -q \int EQE(\lambda) \cdot \Phi(\lambda) d\lambda \quad (2.1)$$

In current studies, EQE measurements were done by a home-built setup that have two 150 W tungsten lamps from LOT-Oriel as a light source for monochromatic radiation and white light background illumination. The setup was fitted with a Zurich Instruments lock-in amplifier and a trans-impedance amplifier as a measurement unit.

2.4.3. Nanogenerator Performance Measurements

To assess the performance of the nanogenerator, a setup consisting of various components was employed, which include a Brüel & Kjær LDS V406 magnetic shaker, a frequency generator, a resistance box (100 Ω to 10 M Ω) and a data acquisition system. A resonant mass-spring system was utilized to induce bending in the nanogenerator. This involved fixing the nanogenerator to a spring steel cantilever with a tip mass of 30 g. The cantilever, along with the attached nanogenerator, was then subjected to vibrations generated by the magnetic shaker. The output voltage was monitored using a Tektronix TDS2012C oscilloscope in trigger mode. The nanogenerator performance of device was measured in ambient condition and an insulating material was used for tapping the device.

3. Results and Discussion

This chapter provides an interpretation and explanation of the work conducted in this project. The results obtained from experiments and the characterization of materials and PSCs are presented using graphs, tables, followed by interpretations. This chapter is divided into three main sections, each focusing on a specific type of study conducted in this work. The first section of the study involves compositional engineering, whereas in the second section, two different methodologies are employed to elucidate the surface treatment of CsPbI₂Br perovskite. In the third section hybrid energy harvester device based on PENG and PSC is described and its performance is discussed. This idea incorporates the piezoelectric and photovoltaic effect in a single device for mechanical and solar energy harvesting, to enable the efficient and complementary use of energy sources.

3.1. Compositional Engineering of CsPbI₂Br Perovskite

The compositional engineering of CsPbI₂Br perovskite was done by altering the precursor ratio to modify the stoichiometry of the perovskite. This altered perovskite was referred as non-stoichiometric perovskite. Afterward, the B-site doping of non-stoichiometric perovskite was done using CuBr₂.

3.1.1. Performance Enhancement of CsPbI₂Br Perovskite Solar Cells via Stoichiometric Control †

Caesium-based inorganic halide perovskite is a promising alternative to address the degradation issue of the organic-inorganic hybrid halide perovskites. However high iodine content in these inorganic perovskites leads to structural instability upon exposure to moisture. In this work, the stoichiometry of CsPbI₂Br perovskite was slightly tuned and its effect on structural stability and device performance was studied. Afterward, the charge transport layers were optimized to improve the charge extraction in perovskite solar cells.

† Part of this section has been published (reproduced with permissions):

Fatima, K., Haider, M. I., Fakharuddin, A., Akhter, Z., Sultan, M., & Schmidt-Mende, L. Performance enhancement of CsPbI₂Br perovskite solar cells via stoichiometric control and interface engineering. *Solar Energy*, 2020, 211, 654-660.

DOI: 10.1016/j.solener.2020.10.007

To investigate the effect of precursor solution stoichiometry on the phase stability of CsPbI₂Br the perovskite precursor ratios was modified. When CsI, PbI₂, and PbBr₂ precursors were added in an appropriate ratio i.e. 1.2:0.6:0.6, a stoichiometrically balanced CsPbI₂Br perovskite was formed. However, a slightly altered precursor ratio (1.2:0.5:0.6), led to the formation of non-stoichiometric perovskite. Both types of perovskites were synthesized through a one-step solution processing method in N₂ environment (in the glovebox). Details of the process are given in section 2.3.1.3.

3.1.1.1. Structural Analysis and Stability Measurement

XRD measurements of the perovskite thin films were carried out to evaluate the structural properties. These measurements were performed in air immediately after exposing the samples to ambient conditions. The XRD patterns of stoichiometric and non-stoichiometric CsPbI₂Br films are shown in Fig. 3.1(a). Consistent with the literature, the main diffraction peaks at 14.7° and 29.7° corresponding to (100) and (200) planes for cubic phase of CsPbI₂Br are evident in both perovskite films.^{97,104,123}

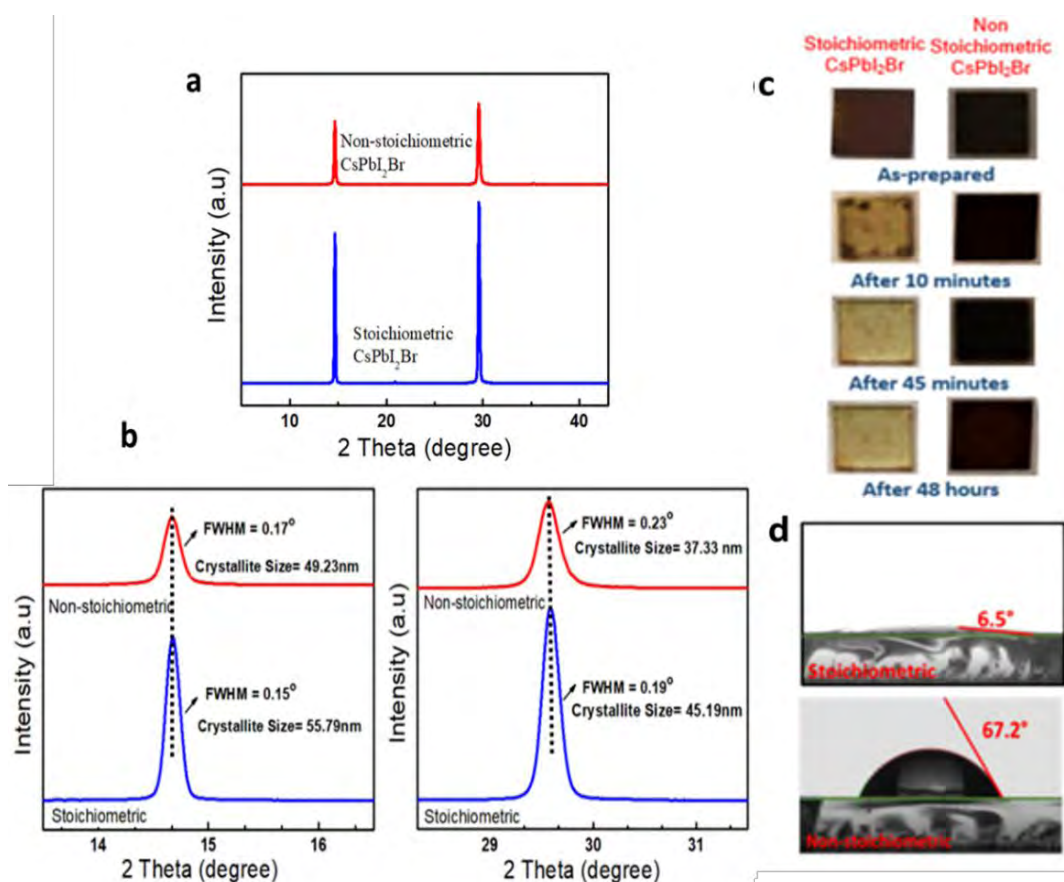


Figure 3.1: (a,b) XRD patterns of perovskite thin films. (c) Comparison of the air stability of the stoichiometric and non-stoichiometric CsPbI₂Br perovskite films. (d) Contact angle measurement.

However, the stoichiometric perovskite showed sharper XRD peaks and narrower fullwidth at half maxima than the non-stoichiometric counterpart suggesting a higher crystallinity of the former. Further, the calculated crystallite size of the stoichiometric perovskite (45.19/55.79 nm) was also larger than that of non-stoichiometric perovskite (37.33/49.23 nm) (**Fig. 3.1(b)**).

The phase stability of both types of perovskite films was studied under ambient conditions (at room temperature, average humidity of 30-40%) outside the glovebox. It was observed that these two films manifest different air stability. Photos of stoichiometric and non-stoichiometric perovskite showing different rates of phase stability in the air are given in **Fig. 3.1(c)**. The stoichiometrically balanced film started to decolorize after 10 minutes and became yellow after 45 minutes. While the non-stoichiometric CsPbI₂Br film did not show any signs of the phase change within 48 hours under the same conditions indicating its better air stability. The observed stabilization effect could be crucially important for the further development of stable PSCs. As this is the moisture-induced phase transition therefore to get an idea about this water contact angle measurements were performed. These measurements showed that the contact angle increased from 6.5° to 67.2° (**Fig. 3.1(d)**) which means that the hydrophilicity of the film decreased by changing the precursor ratio thus leading to an increase in moisture tolerance.

3.1.1.2. Photophysical Properties

To get insight into photo-physical properties, UV-Vis absorbance and SSPL spectra of both perovskite films were recorded. The absorbance and emission spectra (**Fig. 3.2(a and c)**) showed that the non-stoichiometric perovskite absorbance and PL emission peaks (centered at 648 nm) are slightly blue-shifted than that of the stoichiometric perovskite film (emission peak at 652 nm). These correspond to a bandgap of 1.91 and 1.90 eV, respectively. This shift might be due to slightly altered chemical composition, e.g., the slightly different ratio of iodide to bromide anions that have shown to induce such spectral shift.¹⁶⁰ **Fig. 3.2(d)** showed the TRPL spectra of the two perovskite films on the glass substrate. Fitting of the TRPL data (slow and fast component) using a bi-exponential model yields lifetime values corresponding to τ_1 and τ_2 as 14.86 ± 0.16 and 25.64 ± 4.91 ns for stoichiometric perovskite film and 7.37 ± 0.11 and 25.79 ± 2.6 ns for non-stoichiometric perovskite film where τ_1 represents non radiative recombinations and τ_2 is associated with radiative recombinations.

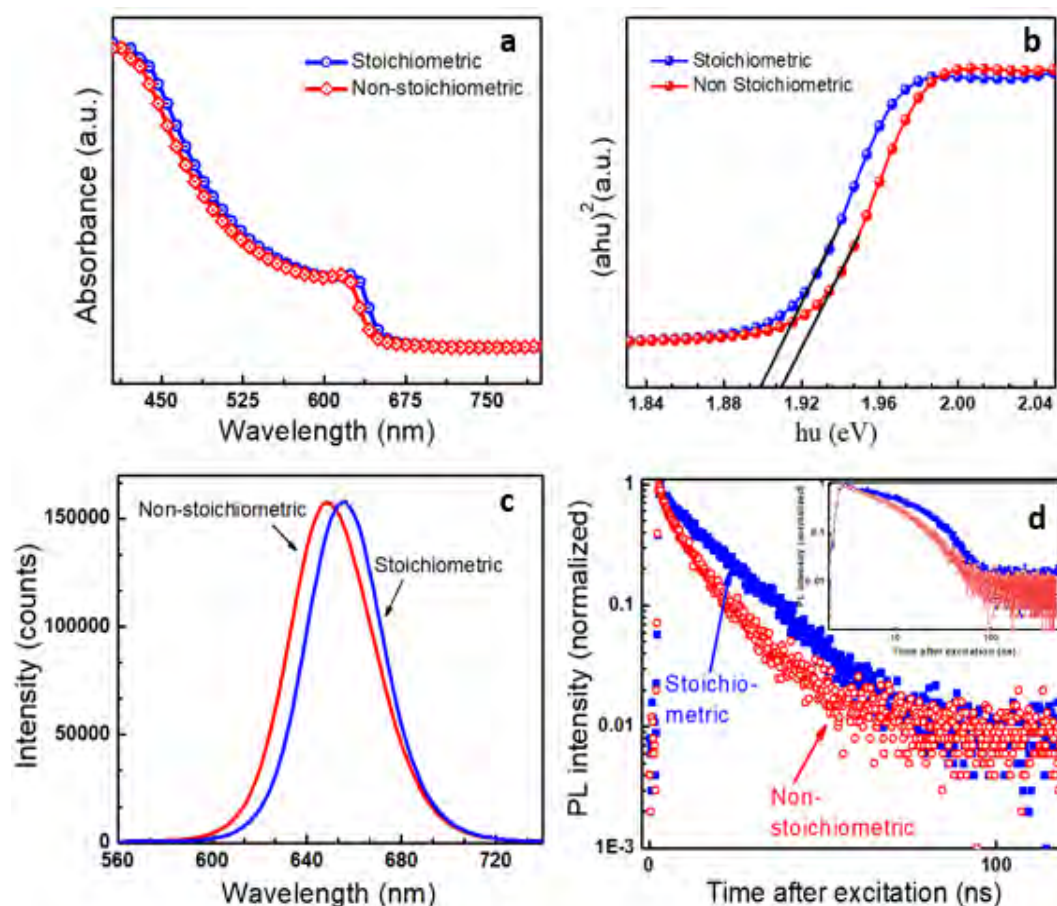


Figure 3.2: (a) UV-visible absorption spectra. (b) Tauc plot (c) SSPL and (d) TRPL spectra of the two perovskite films on a glass substrate. The films were excited using a 485 nm pulsed laser.

To estimate the ionization potential, PESA measurement of both perovskite films was carried out in the air. The measured VBM values were -5.37 eV and -5.24 eV for stoichiometric and non-stoichiometric film, respectively, as shown in **Fig. 3.3(a and b)**. Thus, by using the bandgap values from PL emission spectra, we inferred the values of CBM by using the formula $CBM = E_g + VBM$. The resultant energy level diagram of the PSC device is shown in **Fig. 3.3(c)**. The band-edge positions of NiO_x , C_{60} , and work functions of ITO and Cu are taken from the literature.^{161,162} The VBM of non-stoichiometric perovskite is somewhat higher and more closely aligned with the valence band of NiO_x as compared to its stoichiometric counterpart which can facilitate more efficient hole extraction.

From these findings it appears that the non-stoichiometric composition of $CsPbI_2Br$ can be a better choice for a device than its stoichiometric counterpart owing to its improved ambient stability and a more favorable energy level alignment for efficient charge extraction.

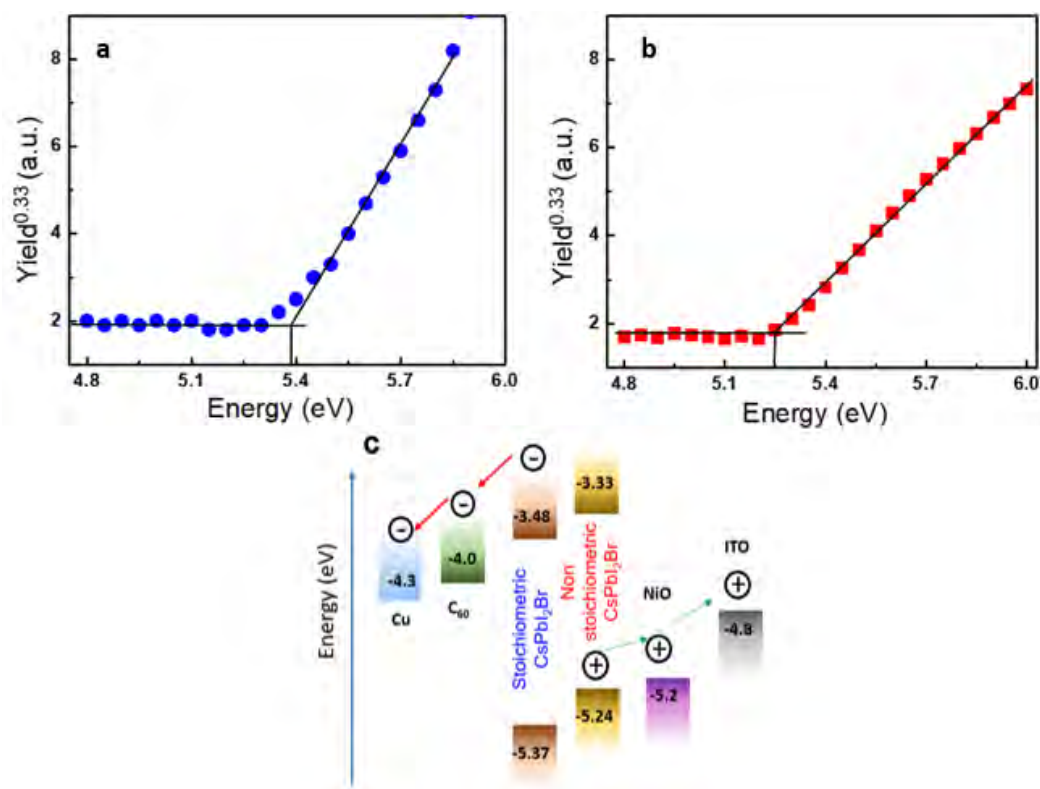


Figure 3.3: PESA measurements of (a) stoichiometric and (b) non-stoichiometric CsPbI_2Br perovskite. c) Energy level diagram of different layers used for the fabrication of PSC.

3.1.1.3. Morphological Studies of Stoichiometric and Non-Stoichiometric Perovskite

The morphology of the perovskite films was analyzed by top-view SEM, as shown in **Fig. 3.4(a)**. The SEM image of both perovskites showed closely packed grains with compact and uniform film morphology while non-stoichiometric perovskite showed smaller grain size with better uniformity. This reduction in grain size with improved air stability is consistent with the findings in previous work.¹⁶³ Furthermore the EDX mapping **Fig. 3.4(b and c)** confirmed the presence and uniform distribution of perovskite elements in both types of perovskites. AFM images shown in **Fig. 3.4(d)** also displayed similar morphology as shown by SEM images and revealed that non-stoichiometric perovskite has a smoother surface as shown by smaller root mean surface roughness (RMS = 25.0 nm) compared to pristine perovskite (RMS = 41.6 nm) which is suitable for efficient charge transport.¹⁶⁴ According to the literature,¹⁶⁵ a water droplet can more easily adsorb on a film's surface when it is rough, but as the surface smoothness increases, the process becomes more difficult. Thus, these results were concordant with the results obtained from water contact angle measurements.

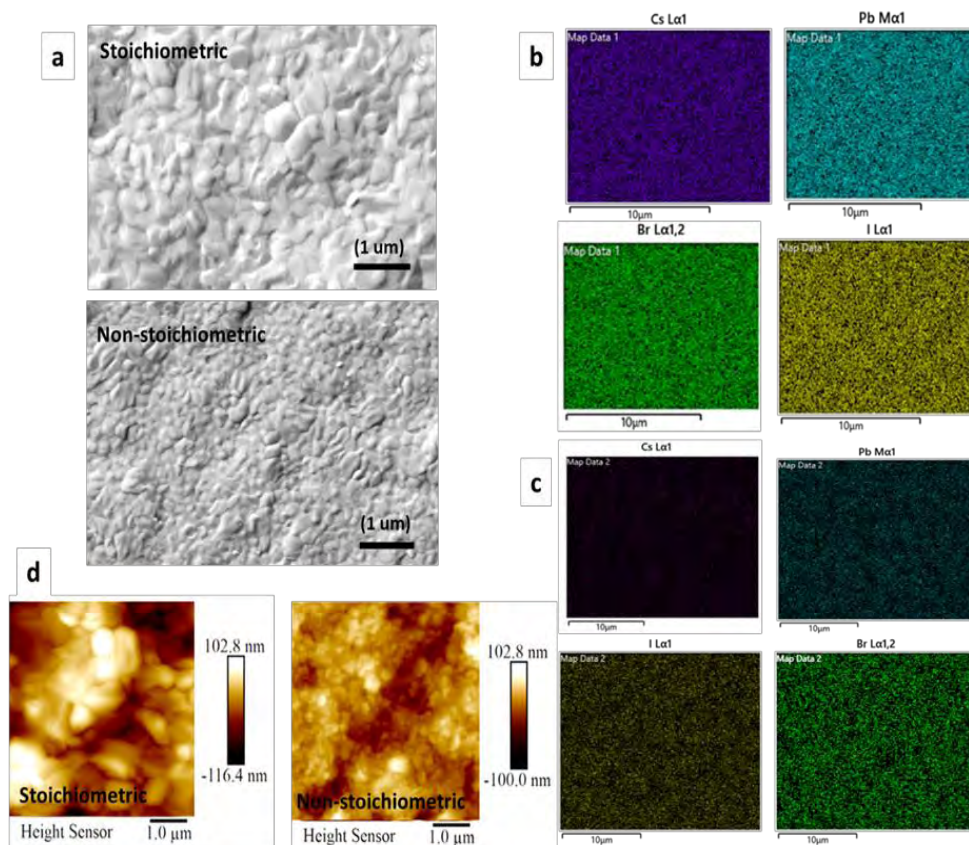


Figure 3.4: (a) Top-down SEM images. (b) EDX elemental mapping stoichiometric (c) non-stoichiometric perovskite. (c) AFM images of the perovskites.

3.1.1.4. X-ray Photoelectron Spectroscopic (XPS) Analysis

The surface elemental distributions of the non-stoichiometric CsPbI₂Br film were further analyzed by XPS analysis.

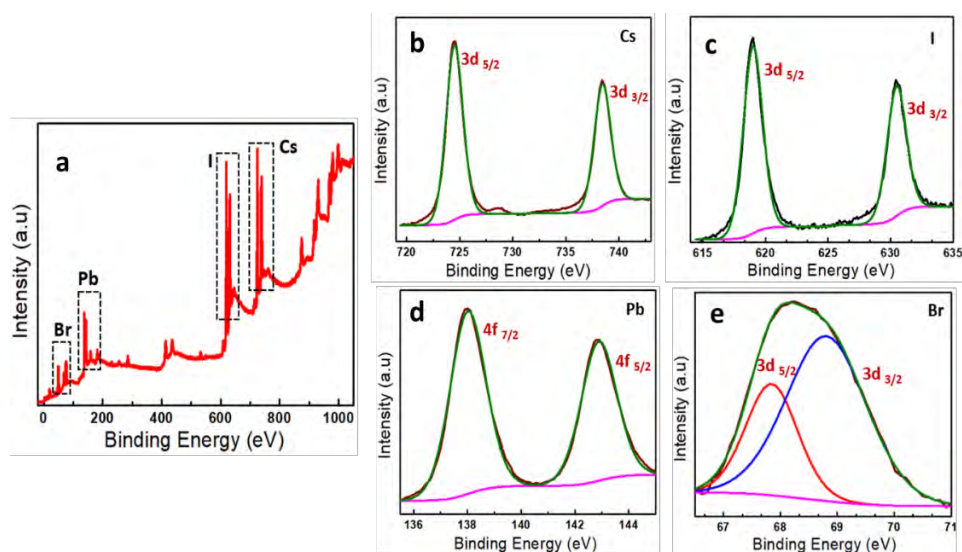


Figure 3.5: (a) XPS survey spectrum of non-stoichiometric CsPbI₂Br thin film, high resolution (b) Cs 3d, (c) Pb 4f, (d) I 3d and (e) Br 3d core level spectra.

Fig. 3.5(a) depicted the XPS survey spectrum, which displayed characteristic peaks corresponding to Cs 3d, Pb 4f, I 3d, and Br 3d verifying the perovskite composition. The high-resolution core-level peaks of all elements are depicted in **Fig. 3.5(b-e)**. The peaks appeared at 724 and 738 eV corresponds to the Cs 3d_{5/2} and 3d_{3/2} respectively with the +1 oxidation state. Similarly, Pb 4f spectra showed 4f_{7/2} and 4f_{5/2} peaks around 138 and 142 eV corresponding to the Pb⁺² cation. Meanwhile, two XPS peaks around 619 and 630 eV are attributed to 3d_{5/2} and 3d_{3/2} peaks of the I 3d spectrum. Br 3d_{3/2} and Br 3d_{5/2} peaks are centered at 67.8 and 68.8 eV, respectively.

3.1.1.5. Photovoltaic Performance and Stability of Perovskite Solar Cells

To compare the effect of change in stoichiometry of CsPbI₂Br on cell performance in inverted PSCs was fabricated with device configuration ITO/NiO_x/Perovskite/C₆₀/LiF/Cu. Current-voltage (J-V) curves of champion PSCs measured at 1 Sun (100 mW/cm²) conditions are shown in **Fig. 3.7(a)**. The non-stoichiometric PSC demonstrated an average J_{SC} of 11.2 mA/cm² (champion J_{SC} of 11.6 mA/cm²) slightly higher than their stoichiometric counterparts (average and champion J_{SC} 9.3 and 10.20 mA/cm², respectively).

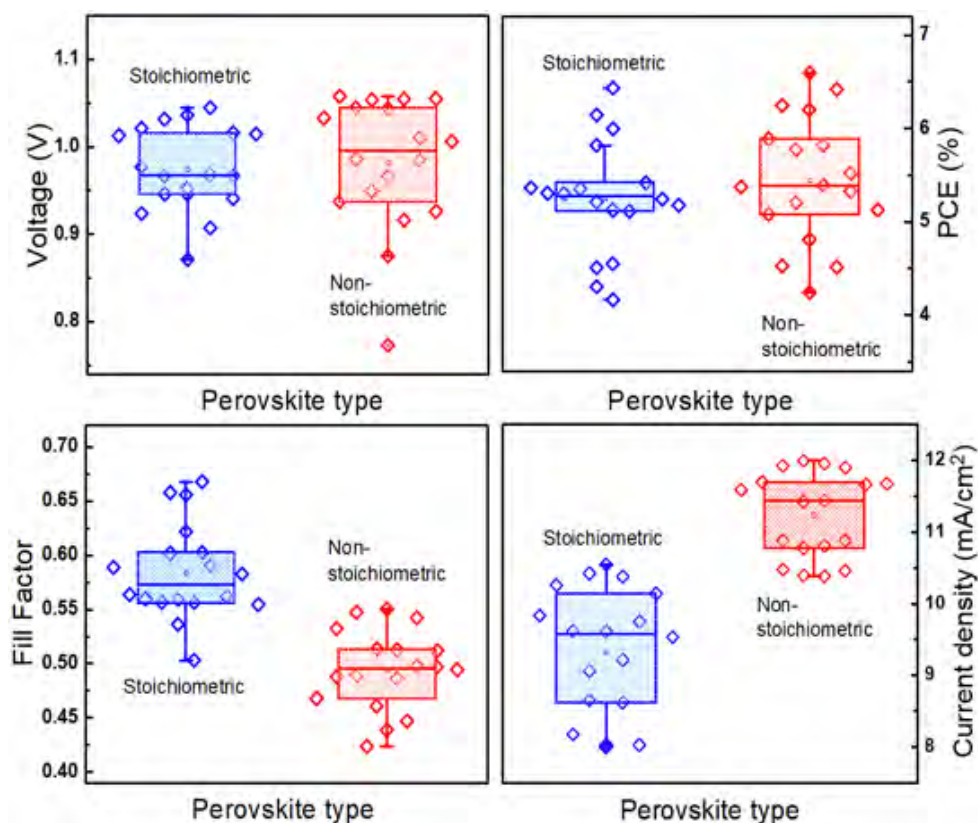


Figure 3.6: Statistical distribution of the photovoltaic parameters of nine devices of each type, stoichiometric and non-stoichiometric devices.

Table 3.1. Photovoltaic parameters (average of nine devices of each type \pm std deviation and champion forward (F) and reverse (R) scans) of stoichiometric and non-stoichiometric device with an active area of 0.133 cm^2 under 1 Sun (100 mW/cm^2) illumination.

Perovskite type	Parameters	J_{sc} (mA/cm^2)	V_{oc} (V)	FF	PCE (%)
Stoichiometric	Average	9.3 ± 0.89	0.97 ± 0.04	0.58 ± 0.04	5.2 ± 0.61
	Champion (F)	10.20	0.92	0.60	5.6
	(R)	10.14	0.98	0.65	6.4
Non-Stoichiometric	Average	11.2 ± 0.59	0.98 ± 0.07	0.49 ± 0.04	5.4 ± 0.67
	Champion (F)	11.66	0.97	0.51	5.8
	(R)	11.69	1.03	0.55	6.6

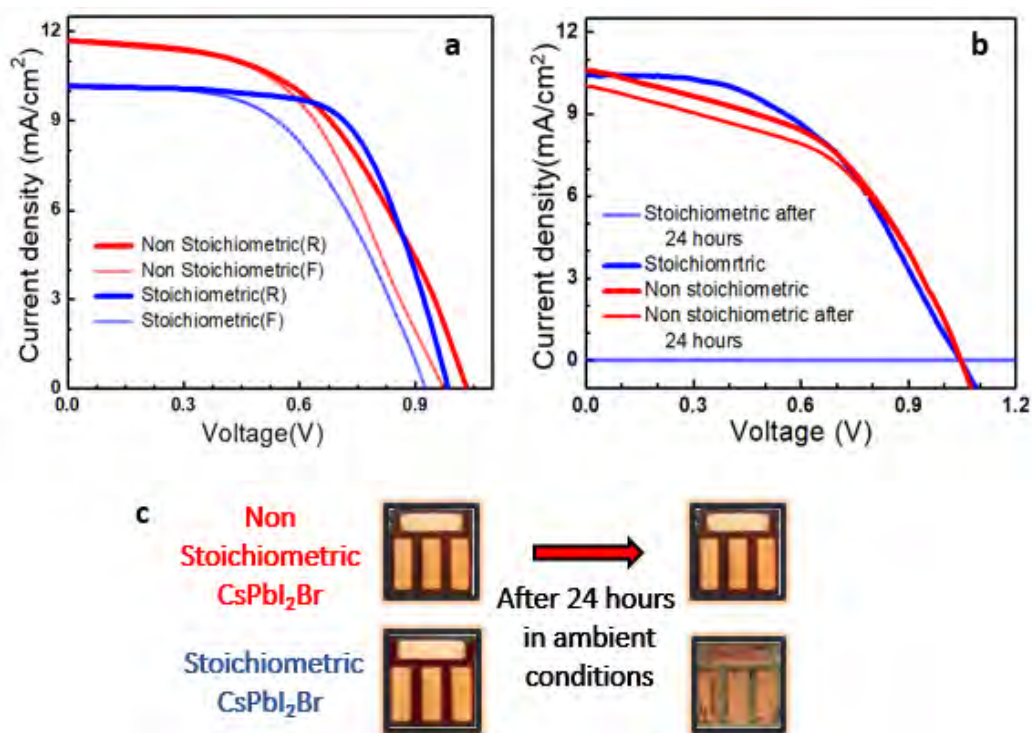


Figure 3.7: (a) J-V curves for F and R scans of the champion stoichiometric and non-stoichiometric devices with an active area of 0.133 cm^2 under 1 Sun (100 mW/cm^2) illumination. (b) J-V curves of representative stoichiometric and non-stoichiometric devices showing their ambient stability. The devices were kept at ambient (un-encapsulated) for 24 hours and the J-V performance was measured before and after storage. (c) Photographs showing the comparison of the air stability of the stoichiometric and non-stoichiometric CsPbI_2Br devices.

Table 3.2. Photovoltaic parameters of the stoichiometric and non-stoichiometric device before and after air exposure for 24 hours.

Perovskite type		J _{sc} (mA/cm ²)	V _{oc} (V)	FF	PCE (%)
Stoichiometric	Before	10.203	1.04	0.48	5.3
	After	9.7x 10 ⁻⁹	0.31	233.78	6.8x 10 ⁻⁷
Non-stoichiometric	Before	10.7	1.06	0.54	5.7
	After	10.0	1.06	0.53	5.5

The higher J_{sc} suggested an improved charge collection in non-stoichiometric PSCs. Both devices showed nearly identical V_{oc} although slightly lower FF is noted in non-stoichiometric PSCs (**Fig. 3.6 and Table 3.1**).

The air stability of both types of PSCs was also investigated. Both the stoichiometric and non-stoichiometric devices were stored in ambient conditions outside the glove box for 24 hours and J-V curves were measured before and after air exposure. The non-stoichiometric PSC retained its performance after 24 hours evidencing no degradation (**Fig. 3.7(b) and Table 3.2**). In contrast, the stoichiometric device showed a complete degradation after air exposure suggesting a phase change. **Fig. 3.7(c)** shows photographs of two types of devices. The non-stoichiometric device showed no color change after 24 hours as compared to the stoichiometric device which changed its color due to phase change-induced degradation. Although non-stoichiometric CsPbI₂Br showed nearly similar PCE values as that of the stoichiometric counterpart, however, its higher ambient stability makes it more promising for practical application. For this reason, we chose this device for further optimization by tailoring charge transport.

3.1.1.6. Optimization of Hole Transport/Extraction Layer

For the optimization of NiO_x HTL in CsPbI₂Br PSCs two different types of NiO_x films were fabricated via sputtering and solution processing. For the sputtered NiO_x film different thicknesses (10nm, 20nm, 30nm, 40nm, and 60nm) were used. **Fig. 3.8** showed the statistical distribution of photovoltaic parameters under 1 Sun (100 mW/cm²) illumination with different types of NiO_x films and the PV parameters are summarized in **Table 3.3**.

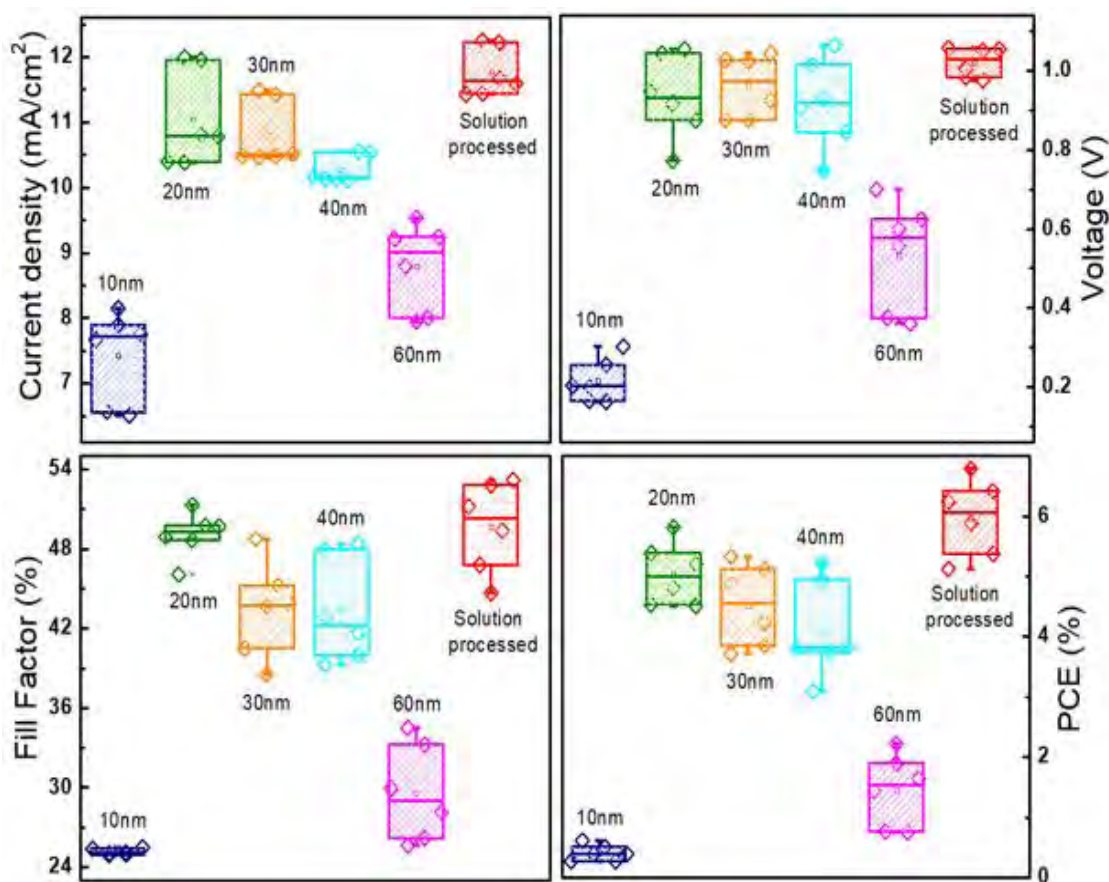


Figure 3.8: Statistical distribution of the photovoltaic parameters of three devices of each type for different types of NiO_x layers in PSCs.

Table 3.3. Photovoltaic parameters (average \pm std Deviation) of devices with different thickness of NiO_x for three devices per data point with an active area of 0.133 cm², under 1 Sun (100 mW/cm²) light illumination.

NiO _x	Parameters	J _{sc} (mA/cm ²)	V _{oc} (V)	FF	PCE (%)
10nm	Average	7.6 \pm 0.6	0.2 \pm 0.05	0.25 \pm 0.002	0.4 \pm 0.12
	Champion	(8.1)	(0.3)	(0.25)	(0.6)
20nm	Average	10.9 \pm 0.6	0.9 \pm 0.11	0.49 \pm 0.02	5.1 \pm 0.50
	Champion	(10.8)	(1.1)	(0.51)	(5.8)
30nm	Average	10.9 \pm 0.5	1.0 \pm 0.07	0.44 \pm 0.03	4.6 \pm 0.59
	Champion	(10,5)	(1.0)	(0.49)	(5.3)
40nm	Average	10.3 \pm 0.2	0.9 \pm 0.11	0.44 \pm 0.04	4.1 \pm 0.79
	Champion	(10.1)	(1.1)	(0.48)	(5.2)
60nm	Average	8.8 \pm 0.7	0.6 \pm 0.11	0.30 \pm 0.03	1.6 \pm 0.49
	Champion	(9.2)	(0.7)	(0.34)	(2.2)

Solution processed	Average Champion	11.8 ± 0.3 (12.2)	1.0 ± 0.03 (1.1)	0.48 ± 0.34 (0.53)	5.9 ± 0.63 (6.8)
--------------------	------------------	--------------------------	-------------------------	---------------------------	-------------------------

The data revealed that the thickness of NiO_x film has a significant impact on the photovoltaic parameters. The performance of devices improved as the thickness increases up to 20 nm and then started to decrease. The lowest photovoltaic performance was noted for a thickness of 10 nm as shown in **Fig. 3.8**. This systematic increase and then decrease follow the trend of V_{OC} and FF as a function of film thickness both increase with increasing thickness of NiO_x layer up to 20 nm and then systematically decrease. A higher V_{OC} of ~1 V was noted for 20 nm thick NiO_x film as HTL. The trend of V_{OC} and FF suggests that the change in performance for different NiO_x thickness is governed by different recombination rates. Nearly identical V_{OC} and FF were noted for 20, 30, and 40 nm thick NiO_x film, however, it decreased drastically for 10 nm and 60 nm devices. For 10 nm, the film might be too thin thus causing shorts and higher recombination (as evidenced by their lowest J_{SC}, FF, and V_{OC}). Contrarily, the drop in performance for 60 nm thick NiO_x film could be due to an increase in series resistance of the film along with increase in the recombination as the film thickness increases.¹⁶⁶

Then, the performance of best performing sputtered NiO_x film (20 nm) with a solution-processed NiO_x having thickness of approximately 20 nm was compared. The J-V curves of the champion devices are shown in **Fig. 3.9** and corresponding PV parameters are shown in **Table 3.4**.

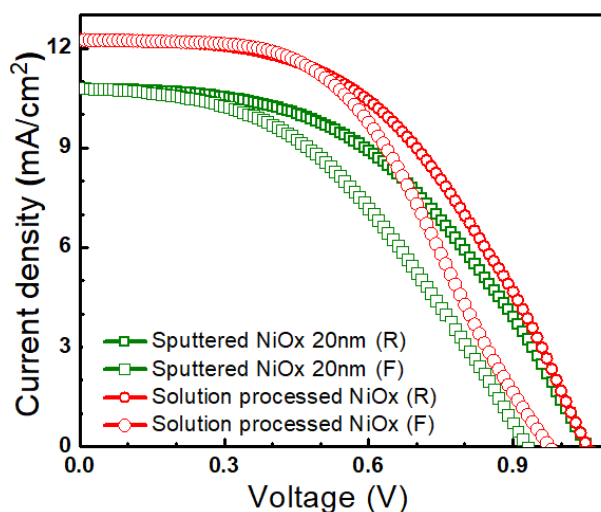


Figure 3.9: J-V curves of the champion solar cell with 20 nm sputtered and solution-processed NiO_x.

Table 3.4. Photovoltaic parameters of 20 nm sputtered and solution-processed NiO_x based champion devices under 1 Sun (100 mW/cm²) illumination.

NiO _x		J _{sc} (mA/cm ²)	V _{oc} (V)	FF	PCE (%)	R _s (Ohm/cm ²)	R _{sh} (Ohm/cm ²)
Sputtered (20nm)	(F)	10.808	0.916	0.49	4.807	0.051	225
	(R)	10.8	1.1	0.51	5.83	0.039	208
Solution processed	(F)	12.218	0.977	0.49	5.883	0.061	295
	(R)	12.251	1.052	0.53	6.791	0.036	214

The sputtered NiO_x based device exhibited a V_{OC} of 1.1 V, a J_{SC} of 10.8 mA cm⁻², and a FF of 0.51, resulting in a PCE of 5.8%. The solution-processed NiO_x-based PSC showed a slightly lower V_{OC} (1.05 V), a higher J_{SC} of 12.2 mA cm⁻², and an increased FF of 0.53, resulting in a PCE of 6.8%. The solution-processed NiO_x devices showed a higher shunt resistance (reduced non-radiative recombination) than that of sputtered NiO_x counterpart which suggested a higher conductivity and better contact at the perovskite/NiO_x interface for solution-processed NiO_x. These contribute to a higher charge collection as evidenced by a higher J_{SC} in solution-processed NiO_x based PSC.

3.1.1.7. Influence of C₆₀ Layer Thickness on the Device Performance

To investigate the role of the ETL and its interface with the perovskite absorber layer, the device performance was investigated by employing solution processed NiO_x as HTL and C₆₀ as an ETL. Four different thicknesses (15 nm, 20 nm, 30 nm, and 45 nm) for C₆₀ ETL were selected. The corresponding statistical data of the PV parameters (**Fig. 3.10**) showed a strong dependency on the thickness of C₆₀ ETL. The PSCs fabricated with a 15 nm C₆₀ layer showed the best PCE of 6.7%, a J_{SC} of 12.0 mA/cm², a V_{OC} of 1.0 V, and a FF of 0.61. The relatively low performance may be because a too thin C₆₀ layer cannot fully cover the perovskite film.¹⁶⁷ The device performance increased as the film thickness increased to 20 nm and subsequently decreased for 30 and 45 nm thick C₆₀ ETLs. We refer to **Table 3.5** for detailed PV parameters. In brief, the 20 nm thick ETL showed the highest J_{SC}, V_{OC}, and FF and a champion PCE of 7.5% (average PCE 6.2%). This was attributed to an optimum C₆₀ thickness, which provided complete surface coverage and an optimum series resistance. A further increase in C₆₀ thickness negatively impacted series resistance mainly affecting V_{OC} and FF which led to a drop in the final PCE.

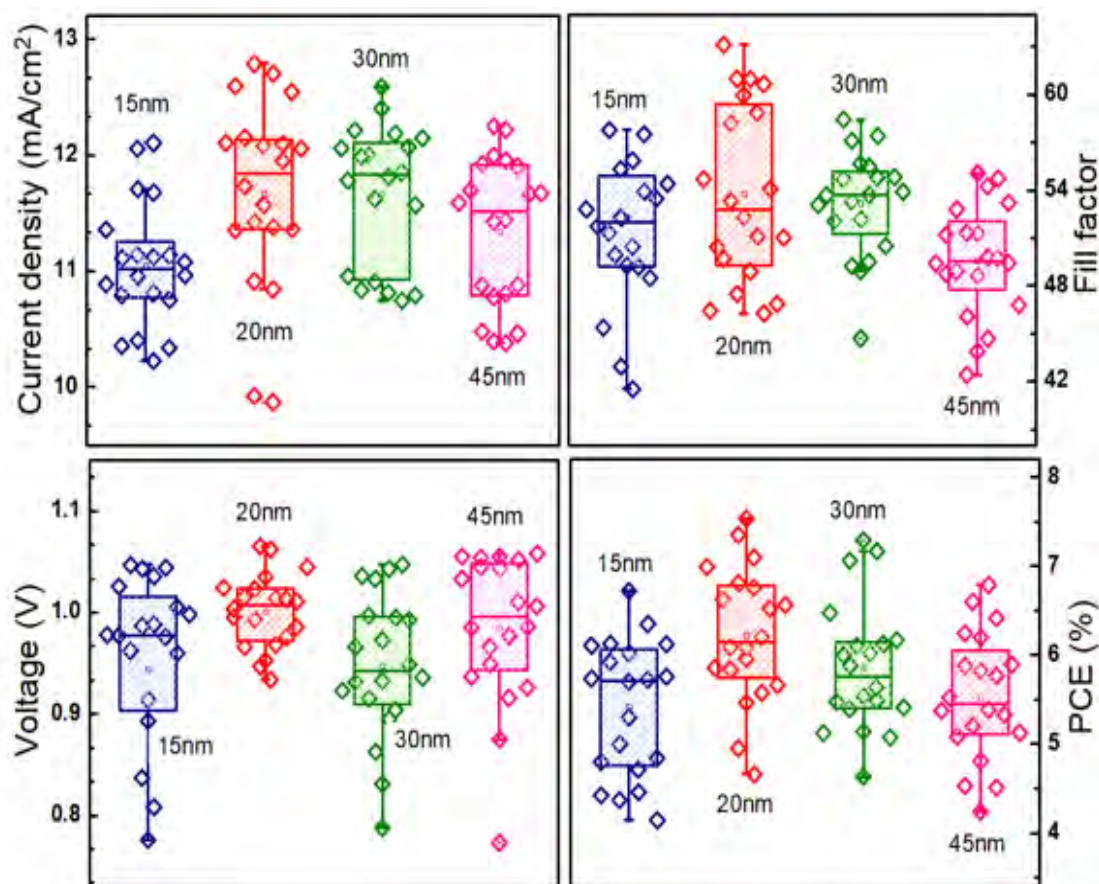


Figure 3.10: Statistical distribution of photovoltaic parameters of ten devices for different thickness of C₆₀ layer in a device configuration ITO/NiO_x/perovskite/C₆₀ LiF/Cu.

Table 3.5. Photovoltaic parameters (average \pm std Deviation) of devices with different C₆₀ layer thickness for ten devices per data point (row 1) and champion device (row 2) under 1 Sun (100 mW/cm²) illumination.

C ₆₀ Thickness (nm)	J _{sc} (mA/cm ²)	V _{oc} (V)	FF	PCE (%)	R _s (Ohm/cm ²)
15	11.0 \pm 0.53 (12.0)	0.9 \pm 0.11 (1.02)	0.52 \pm 0.06 (0.61)	5.4 \pm 0.76 (6.7)	(0.029)
20	11.7 \pm 0.82 (12.7)	1.0 \pm 0.04 (1.02)	0.54 \pm 0.06 (0.58)	6.2 \pm 0.76 (7.5)	(0.01)
30	11.7 \pm 0.60 (12.6)	0.9 \pm 0.07 (1.03)	0.53 \pm 0.03 (0.56)	5.9 \pm 0.72 (7.2)	(0.022)
45	11.3 \pm 0.64 (12.2)	0.9 \pm 0.07 (1.02)	0.49 \pm 0.03 (0.53)	5.5 \pm 0.7 (6.8)	(0.037)

Thus an optimum C_{60} layer thickness is desirable to provide a trade-off between surface coverage and series resistance¹⁶⁸ which in this study is achieved for a 20 nm thin C_{60} ETL. The dark and light J-V curves of the champion device employing a 20 nm thick C_{60} ETL are shown in **Fig. 3.11(a)**. The optimized device achieved a PCE of 7.5% with a J_{SC} of 12.7 mA/cm^2 , a V_{OC} of 1.02 V, a FF of 0.58 and negligible hysteresis.

3.1.1.8. EQE Measurement, MPP Tracking and Stability Test of Champion Device

To validate the photocurrent of devices, the EQE measurement of the champion cell was also carried out as shown in **Fig. 3.11(b)**. The J_{SC} , EQE, calculated by integrating IPCE spectra over the entire visible spectrum with the photon flux at 1 Sun conditions yielded a J_{SC} of 12.44 mA/cm^2 , which matched with the measured J_{SC} of 12.71 mA/cm^2 using J-V curves.

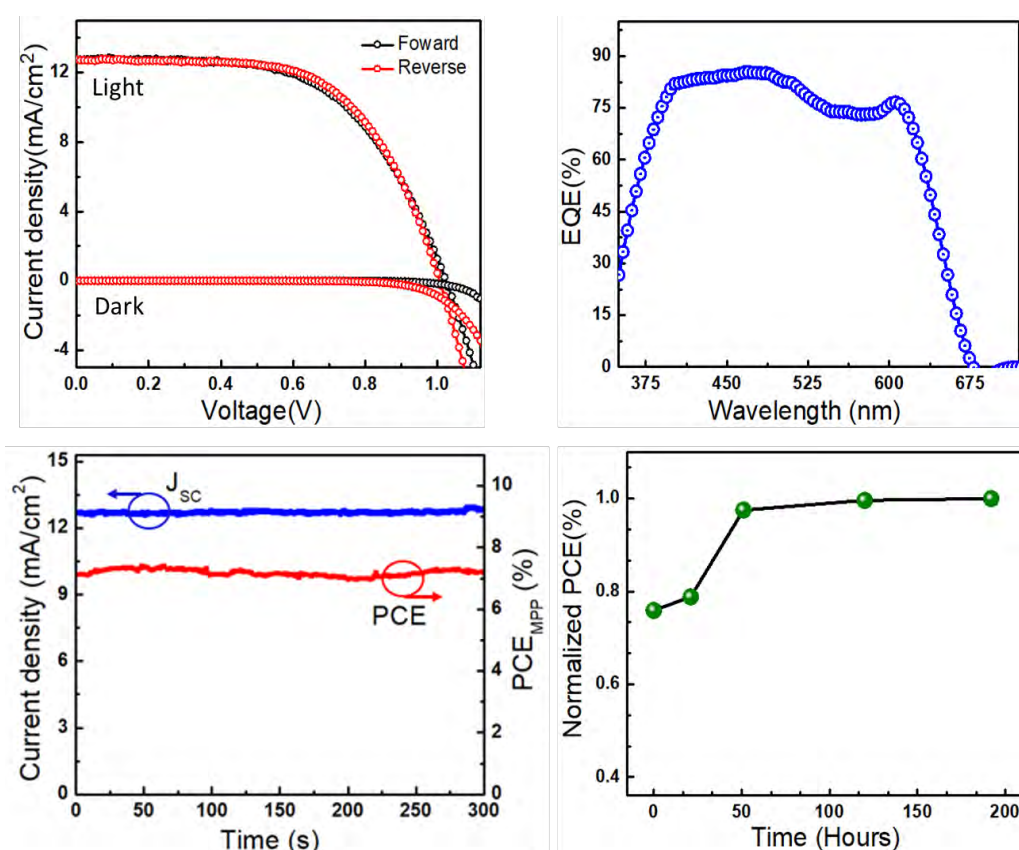


Figure 3.11: (a) J-V curves of the best-performing cell (active area of 0.133 cm^2) measured under 1 Sun ($100 \text{ mW}/\text{cm}^2$) illumination. (b) EQE spectrum of the champion cell. (c) Stabilized J_{SC} and PCE at maximum power point (held at 0.74 V). (d) Normalized PCEs as a function of storage time in the glovebox.

To further validate the performance of the PSCs, we tracked the PCE and J_{SC} of the champion device at continuous illumination under 1 Sun at an output voltage of 0.74V.

Fig. 3.11(c) showed a steady-state J_{SC} of 12.6 mA/cm² and a stabilized PCE of 7.4%. This PCE value matched with the PCE calculated from the J-V curve. Notably, the device retained its performance after continuous light soaking for 300 s. The stability of the device as a function of storage time was also recorded. The devices were stored in the glovebox and measured under standard AM 1.5 illumination. **Fig. 3.11(d)** showed that the device efficiency initially increased and remained unchanged for 200 hours. The PSC showed no sign of degradation, evidencing a stable performance.

In summary, systematic exploration of stoichiometric and non-stoichiometric CsPbI₂Br perovskites as an absorber layer in PSCs demonstrated that non-stoichiometric CsPbI₂Br showed improved stability in combination with favorable energetics and better photovoltaic characteristics than its stoichiometric counterpart.

3.1.2. Bivalent Copper Cation Doping Strategy Enables Reduced Defect Density and Improved Performance of Non-Stoichiometric CsPb_{1-x}I_{2-x}Br PSCs

B-site doping in ABX₃ perovskite is regarded as a simple and effective strategy to improve the PCEs of PSCs. Motivated by this fact a simple doping strategy was used by employing an appropriate amount of Cu²⁺ into a non-stoichiometric CsPb_{1-x}I_{2-x}Br perovskite. Bromine salt is chosen to avoid additional impurities into the perovskite films. As the ionic radius of Cu²⁺ (0.72 Å) is smaller than that of Pb²⁺ (1.19 Å), so divalent Cu²⁺ cations can easily replace the Pb²⁺ ions in the lattice structure of CsPb_{1-x}I_{2-x}Br perovskite.

3.1.2.1. Dopant Optimization and Device Performance

Herein, we explored the effect of B-site doping on the properties of non-stoichiometric CsPb_{1-x}I_{2-x}Br (IP) perovskite by incorporation of copper bromide (CuBr₂) into perovskite precursor solution. To investigate the effect of the Cu²⁺ doping on the photovoltaic performance of PSCs, the PSCs were fabricated having a configuration of ITO/NiO_x/perovskite/C₆₀/LiF/Cu, by employing (IP) perovskite with different percentages of Cu²⁺ (2,3 and 5) as an absorber layer, solution processed NiO_x as HTL and 20 nm of C₆₀ as an ETL. **Fig. 3.12** showed the statistical distribution of photovoltaic parameters under 1 Sun (100 mW/cm²) light illumination with different percentage of CuBr₂ and their corresponding values are summarized in **Table 3.6**. The data revealed that the percentage of CuBr₂ has a significant impact on the photovoltaic parameters. The device performance improved as the CuBr₂ percentage increased up to 2% and then

started to decrease with 3% and 5% respectively. The lowest photovoltaic performance was noted for 5% doped devices as shown in **Fig. 3.12**. The average FF values for the IP and 2%, 3% and 5% CuBr₂ based devices were 0.56, 0.62, 0.60 and 0.47 respectively. The trend of photovoltaic parameters suggested that the change in performance was governed by different charge extraction and recombination rate.

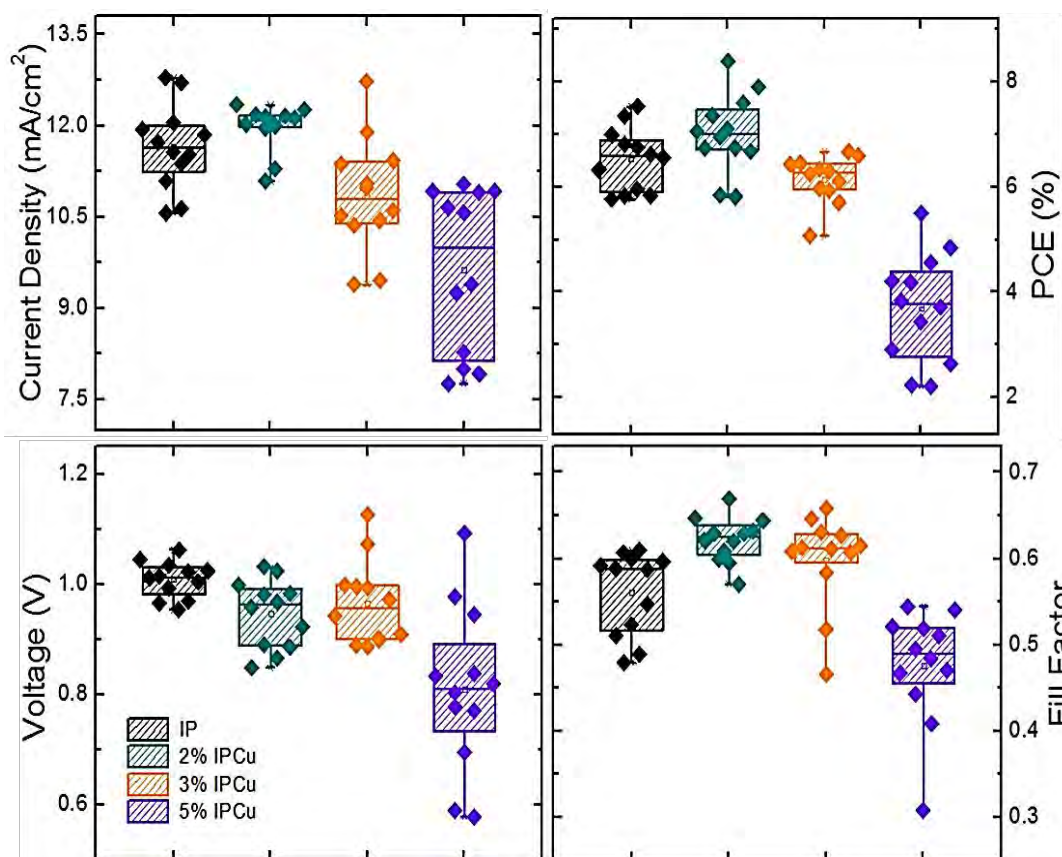


Figure 3.12: Statistical distribution of photovoltaic parameters (six devices of each type) for pristine and with different percentage CuBr₂ devices.

Table 3.6. Photovoltaic parameters (average \pm std Deviation) of PSCs with different percentage of CuBr₂ for six devices of each type with an active area of 0.133 cm² extracted from J-V measurements under 1 Sun (100 mW/cm²) illumination.

CuBr ₂ (%)	J _{SC} (mA/cm ²)	V _{OC} (V)	FF (%)	PCE (%)
0	11.65 \pm 0.69	1.01 \pm 0.03	0.56 \pm 0.05	6.53 \pm 0.60
2	11.96 \pm 0.38	0.95 \pm 0.06	0.62 \pm 0.03	7.02 \pm 0.75
3	10.85 \pm 0.95	0.96 \pm 0.07	0.60 \pm 0.05	6.15 \pm 0.44
5	9.64 \pm 1.35	0.81 \pm 0.14	0.47 \pm 0.06	3.69 \pm 1.04

For these results it appeared that the highest PCE of 7.02% was obtained by the 2% CuBr₂ based devices. The PCE improvement was mainly ascribed to the increase in FF and J_{sc}. The FF values of the PSCs enhanced notably from 0.56 for IP to 0.62 for 2% CuBr₂. The J_{sc} of the PSCs was slightly improved from 11.65 to 11.96 mA cm⁻² for 2% CuBr₂. The FF and J_{sc} improvement were mainly resultant from the improved morphology, reduced non-radiative recombinations and efficient charge extraction ability of IPCu 2%. devices. Thus 2% is selected as the optimum CuBr₂ percentage for devices with the selected configuration. In further discussion the 2% CuBr₂ doped non-stoichiometric perovskite will be termed as IPCu.

3.1.2.2. Structural Analysis

The photographs of the perovskite precursor solutions with the addition of CuBr₂ showed that the color of the perovskite precursor solution changed to brown from yellow but did not affect the color of the fabricated perovskite film (3.13(a)). In order to analyze the structure, XRD measurements of IP and IPCu films after annealing at 40 °C for 4 minutes and 150 °C for 5 min were performed and the results are shown in Fig. 3.13(b).

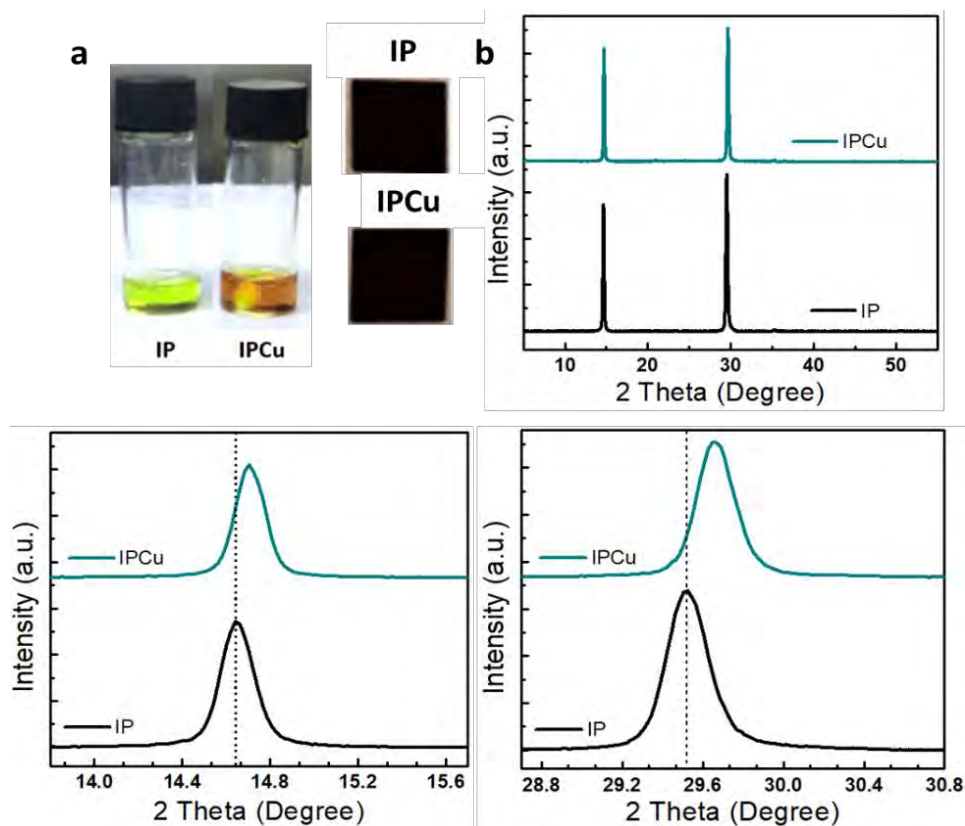


Figure 3.13: (a) The photographs of IP and IPCu precursor solutions and fabricated perovskite films. (b) XRD patterns of IP and IPCu thin films.

The XRD diffraction peaks at 2θ around 15° and 30° correspond to the (100) and (200) planes of α -phase CsPbI₂Br perovskite, inferring a preferential growth direction along the (100) and (200) planes of the grains in the perovskite films.¹⁶⁹ No impurity peaks were detected, indicating that fabricated perovskite films were phase pure with cubic structures and the Cu²⁺ substitution preserves the structure of the perovskite host.¹⁷⁰ Moreover, the calculated crystallite size of the IPCu (34.24/47.82 nm) is smaller than that of IP perovskite (37.33/49.23 nm). In addition, the peak positions of fabricated IPCu film slightly shifted toward higher angle which depicted the successful incorporation of Cu²⁺ into the B-site of the IP lattice. The Cu²⁺ cation has a smaller ionic radius (72 pm) than Pb²⁺ (120 pm), which decreased the size of the perovskite lattice and thus reduced the crystallite size.

3.1.2.3. SEM and AFM Analysis

In consideration of the fact that the morphology of perovskite film has a significant effect on PSC performance, we examined the surface morphologies of both perovskite films by top view SEM images and the results are shown in **Fig. 3.14(a and b)**. After doping the perovskite film exhibited a compact morphology without any pinholes. To ensure the presence of Cu²⁺ and to analyze its distribution in the IPCu perovskite film, EDX spectroscopy was performed. As shown in **Fig. 3.14(c)**, all perovskite elements were uniformly distributed on entire perovskite film.

The top-view AFM was also performed and the corresponding images of pristine IP and IPCu perovskite films, shown in **Fig. 3.14(d and e)**, again manifested the formation of compact film without any pinholes. Moreover, the RMS of the IPCu (13.7 nm) was smaller than that of the IP (25.0 nm), which proved beneficial to minimize the contact resistance.¹⁷¹ Consequently, it is safe to state that the incorporation of an optimal quantity of Cu²⁺ into the perovskite structure enabled the formation of a compact and smooth perovskite film. The better perovskite film quality with reduced defect density and charge recombination plays a vital role in acquiring high-performance PSCs.

3.1.2.4. Optoelectronic Properties of IP and IPCu Perovskites

To further investigate the effect of Cu²⁺ doping on enhanced device performance, some important optoelectronic properties of IP and IPCu perovskites were also investigated. The UV-Vis absorption spectra of IP and IPCu films were collected and compared in **Fig. 3.15(a)**. Notably, the IPCu film showed enhanced optical absorption suggesting

improved light absorption ability of doped devices.

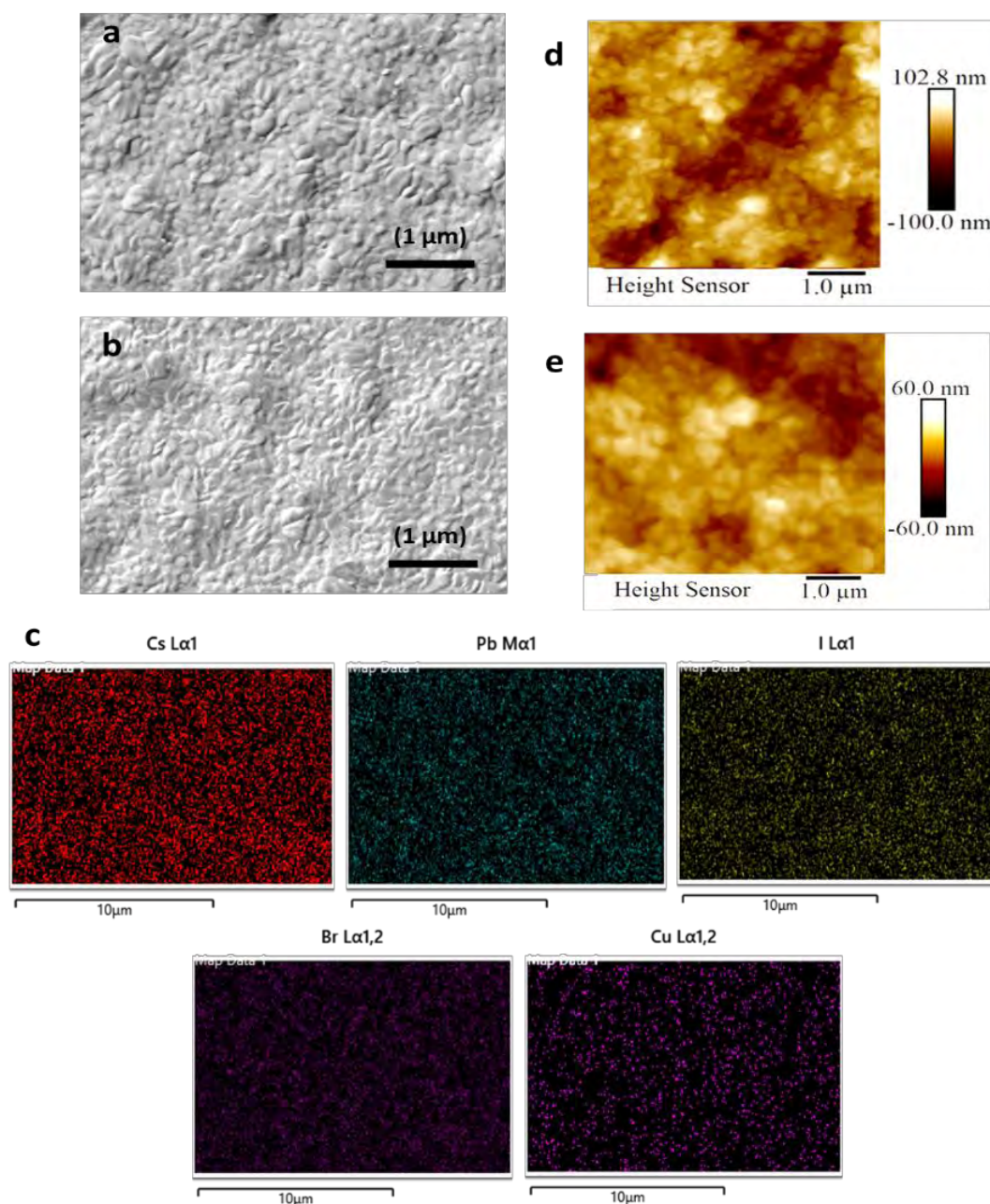


Figure 3.14: Top-down SEM images of the (a) IP and (b) IPCu films. (c) EDX mapping images of IPCu perovskite film. AFM image of the (d) IP and (e) IPCu films.

The calculated bandgap by Tauc plot given in **Fig. 3.15(b)** suggested a value of 1.87 eV for IPCu perovskite film. The value of the highest occupied molecular orbital (HOMO) for IPCu perovskite film from PESA measurements was estimated to be 5.21 eV (**Figure 3.15 (c)**). Thus, by using the bandgap values from the absorption spectra and HOMO values from PESA, we inferred the values of the conduction band minimum. The calculated energy level diagram of the fabricated PSC is displayed in

Fig. 3.15(d). The band-edge positions of NiO_x, C₆₀, IP and work functions of ITO and Cu are taken from the literature.^{172,173} The resultant energy level diagram shows that the incorporation of CuBr₂ reduces the barrier between the interfaces allowing efficient extraction of charges and improving the charge transport effectively.

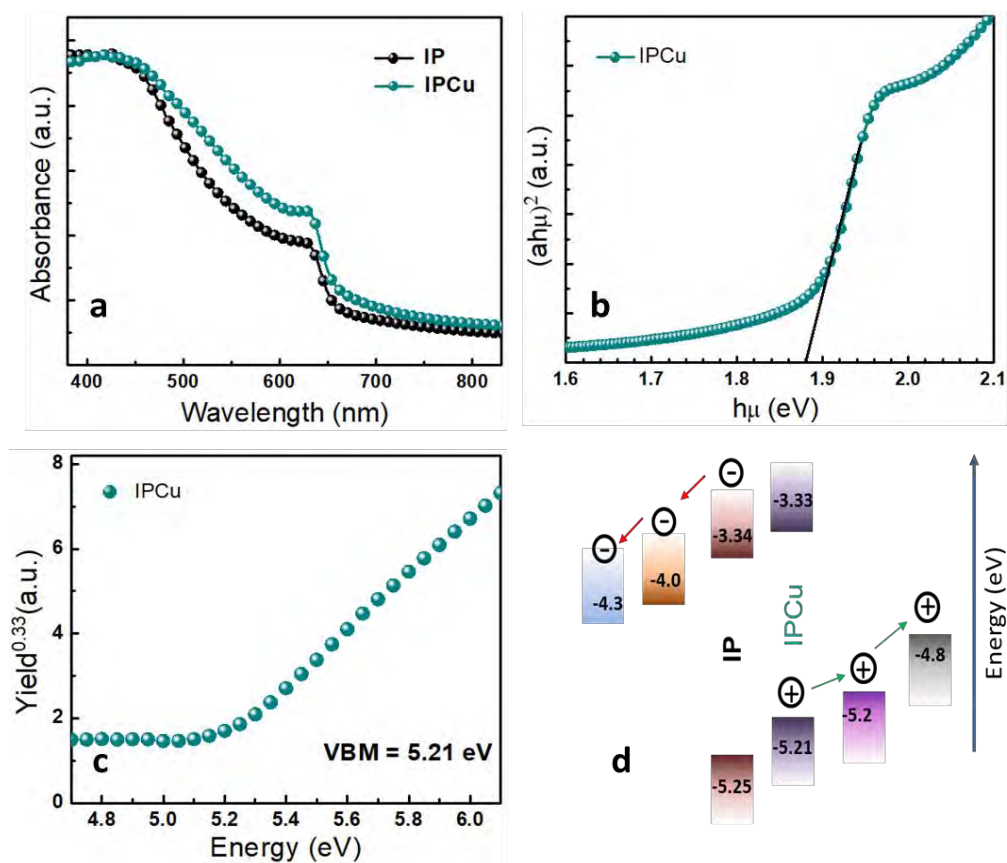


Figure 3.15: (a) UV-Vis absorption spectra. (b) Optical band gap calculated by using Tauc plot. (c) PESA measurements of IPCu thin film. (d) Energy level diagram of the fabricated PSC.

To further investigate the defect and recombination dynamics in IP and IPCu perovskite films, SSPL and TRPL spectra were recorded and shown in **Fig. 3.16** and the TRPL fitting parameters are listed in **Table 3.7**. The SSPL spectrum of the doped perovskite film on glass (non-quenching substrates) showed higher PL emission. Such a substantial increase in PL emission intensity manifests a higher radiative yield due to a smaller trap density. This is further confirmed by the TRPL curves of both samples. The IPCu perovskite displayed a smaller decline in the intensity during the first few ns, which is another indication of reduced nonradiative recombination sites in the film,¹⁷⁴ which in this work is obtained by CuBr₂ doping. The increase in τ_1 with a decrease in τ_2 for IPCu perovskite film compared to IP film manifests reduced nonradiative recombination at the interface and fewer defects in doped perovskite.

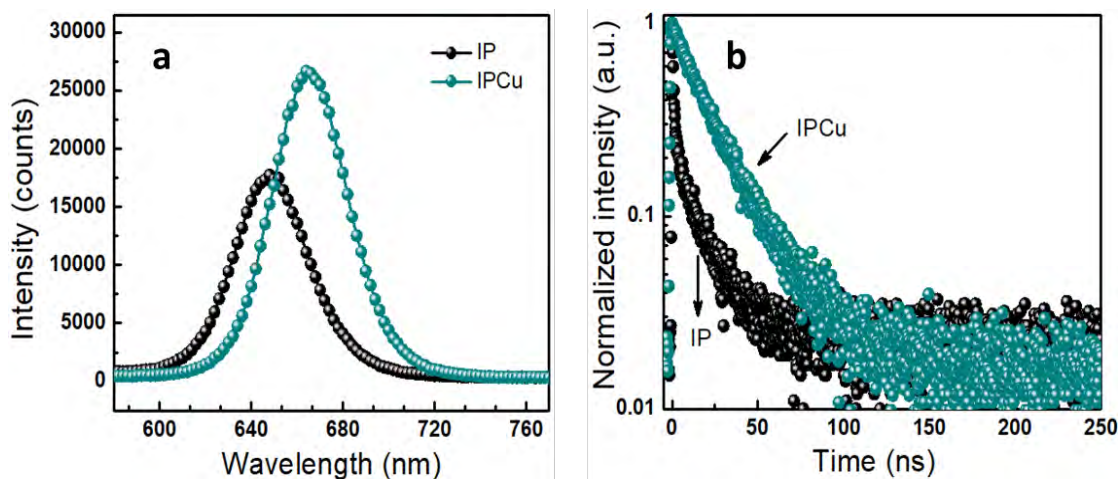


Figure 3.16: (a) PL steady state and (d) TRPL spectra of IP and IPCu films on glass.

Table 3.7. The fitting parameters for TRPL decay curves, band gap and VBM values obtained for IP and IPCu perovskite.

Parameters	τ_1 (ns)	τ_2 (ns)	Band Gap	VBM
IP	7.37 ± 0.11	25.8 ± 2.60	1.91	5.25
IPCu	12.2 ± 1.34	24.7 ± 0.86	1.88	5.21

3.1.2.5. Photovoltaic Performance, MPPT and EQE Measurement of Champion PSC Device

The J-V curves of the champion device in forward (F) and reverse (R) directions under 1 Sun (100 mW/cm^2) are shown in **Fig. 3.17(a)**. The device demonstrated a J_{sc} of 12.26 mA/cm^2 , a V_{oc} of 1.03 V with a FF of 0.67 and PCE of 8.39% in the forward scan and J_{sc} of 12.34 mA/cm^2 , a V_{oc} of 0.99 V with a FF of 0.65 and PCE of 7.91% in the reverse scan.

To validate the performance of the fabricated device, we tracked the PCE of the champion device at continuous illumination under 1 Sun at an output voltage of 0.77 V . **Fig. 3.17(b)** showed a stabilized PCE of around 8% . The PCE value matched with the PCE obtained from the J-V curves. Notably, the device retained its performance after continuous light soaking for 300 s . To further validate the photocurrent of our devices, we also measured the EQE of the champion cell as shown in **Fig. 3.17(c)**. The J_{sc} EQE, calculated by integrating IPCE spectra over the entire visible spectrum with the photon flux at 1 Sun conditions yielded a J_{sc} of 12.40 mA/cm^2 , which well matched with the measured J_{sc} using J-V curves.

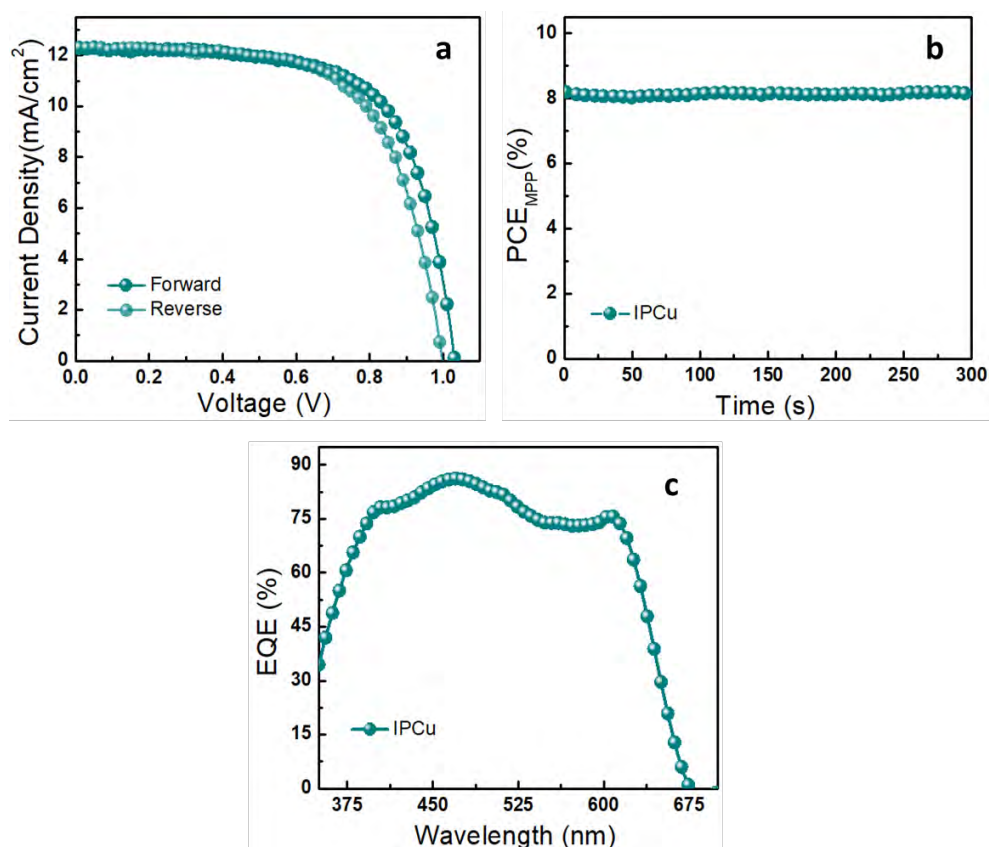


Figure 3.17: (a) J-V curves of the best-performing IPCu device (active area of 0.133 cm²) measured under 1 Sun (100 mW/cm²) illumination. (b) Stabilized PCE at maximum power point (held at 0.77 V). (c) EQE spectrum of the champion cell.

In summary, Cu²⁺ doped CsPb_{1-x}I_{2-x}Br perovskite was synthesized. The structural, photophysical and morphological analysis demonstrated that an appropriate amount of Cu²⁺ can enhance the optoelectronic properties of the perovskite film and reduce the defects in perovskite film thus leading to improvement in the performance of fabricated PSC devices.

3.2. Surface Treatment of CsPbI₂Br Perovskite

The surface treatment of CsPbI₂Br perovskite was carried out using two distinct methodologies. One method involved the IPA treatment to modify the perovskite surface, while the other one utilized the Lewis acid-base passivation method to passivate the CsPbI₂Br surface with EDA.

3.2.1. Surface Modification of CsPbI₂Br for Improved Performance of Inorganic Perovskite Solar Cells ‡

The main obstacle in achieving highly efficient PSCs lies in the fabrication of a high-quality perovskite absorber layer. Herein, in this study, we present a method for surface

treatment of the CsPbI₂Br layer with IPA. In this method, the perovskite material was synthesized through solution processed method followed by solvent post-treatment, which involves the dipping of fabricated perovskite films in IPA for a specific time. The CsPbI₂Br perovskite film was spin coated on the top of NiO_x by a previously reported method.¹⁵⁶ The schematic illustration for the perovskite treatment with IPA is presented in **Fig. 3.18(a)**. This method involves the dipping of fabricated perovskite films in IPA for a specific time followed by drying at 40 °C.

3.2.1.1. Structural and Morphological Studies

The crystal structure of the IPA-treated CsPbI₂Br films was examined using XRD as shown in **Fig. 3.18(b)**. The diffraction pattern showed peaks at $2\theta = 14.7^\circ$ and 29.7° , which could be assigned to the (100) and (200) crystal planes corresponding to the cubic phase of CsPbI₂Br perovskite.¹²³ XPS was used to investigate the effect of surface treatment on the surface composition of the CsPbI₂Br films (**Fig. 3.18(c)**). Based on the XPS results, the Pb 4f_{7/2} and I 3d_{5/2} peaks exhibited almost similar positions (138.5 eV for Pb and 619 eV for I) and shapes for both pristine and IPA-treated samples indicating that there was no change in surface stoichiometry. However, a slight modification in the C 1s spectra was observed. The IPA-treated perovskite demonstrated less adsorbed carbon in comparison to the pristine CsPbI₂Br. As the XPS spectra reveal the presence of different functional groups resulting from the adsorption of compounds at the active sites and grain boundaries.¹⁷⁵ Here, the reduced carbon absorption in the treated perovskite film suggests the existence of active sites that promote better top layer growth. This, in turn, results in a better interface between the perovskite and the ETL ultimately facilitating efficient charge extraction at the interface as complemented by the PESA and PL studies in the next section.

Further, the surface morphology of perovskite films was investigated using SEM, and the results are shown in **Fig. 3.19(a)**. Both types of perovskites showed compact

‡ Part of this section has been published (reproduced with permissions):

Fatima, K., Haider, M. I., Bashir, A., Qamar, S., Qureshi, A. A., Akhter, Z., & Sultan, M. (2022). Surface modification of CsPbI₂Br for improved performance of inorganic perovskite solar cells. *Physica E: Low-dimensional Systems and Nanostructures*, 142, 115265.

DOI: 10.1016/j.physe.2022.115265

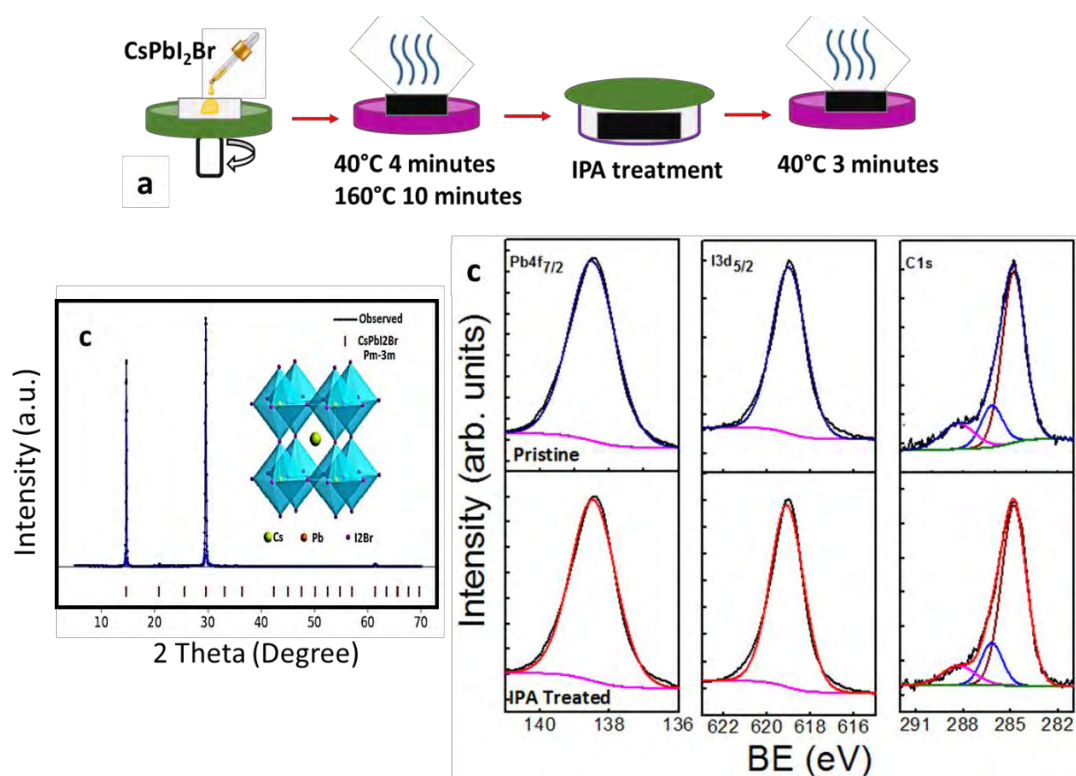


Figure 3.18: (a) Schematic representation of the process for the preparation of the IPA treated CsPbI₂Br film. (b) XRD pattern of the IPA-treated CsPbI₂Br film. (c) High-resolution XPS spectra of the Pb 4f_{7/2}, I 3d_{5/2} and C 1s from the perovskite film surface (upper panel) and with IPA treatment (lower panel).

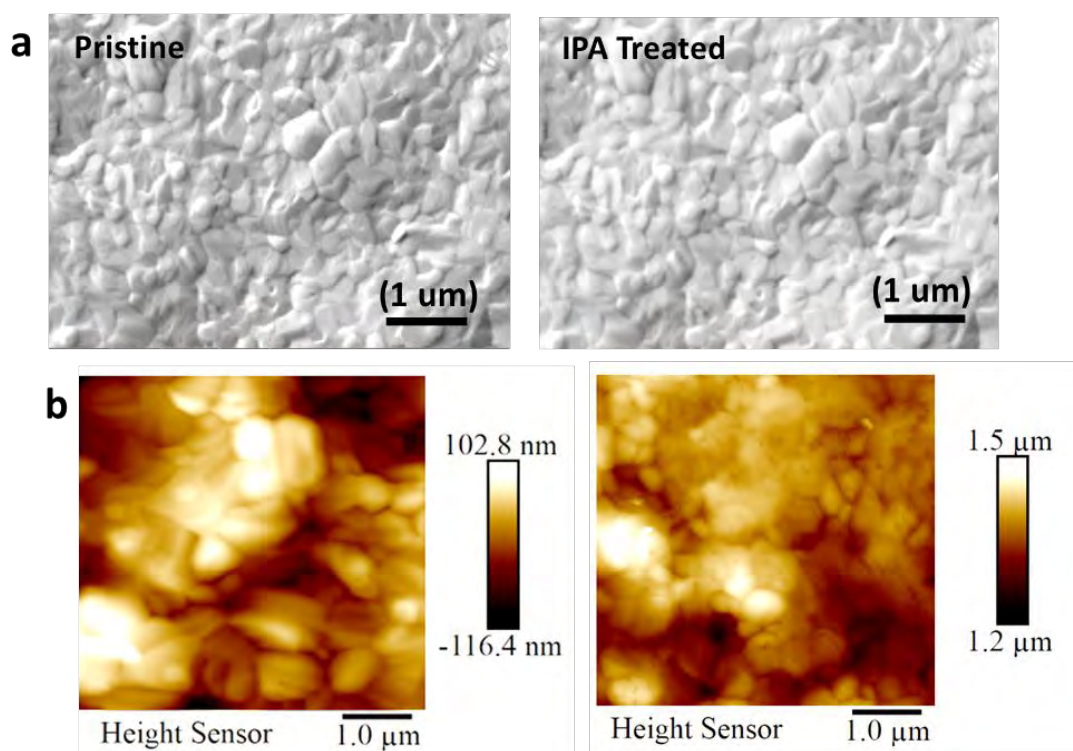


Figure 3.19: (a) Top-down SEM image of pristine and IPA treated film. (b) AFM images of pristine and IPA treated perovskite films.

morphology with irregular grains with no significant difference in the morphology of perovskite upon treatment. **Fig. 3.19(b)** showed the AFM images of the pristine and IPA-treated films. The IPA-treated film exhibited a smoother surface with a smaller root-mean-squared roughness (RMS) of 39.2 nm in comparison to that of the pristine film (RMS 41.6 nm) which was suitable for minimizing the contact resistance.

3.2.1.2. Process Optimization and Device Performance

Furthermore, the perovskite devices were fabricated to see the effect of post-treatment on the performance of the devices. The device performance was optimized by adjusting the dipping time for the post-treatment of CsPbI₂Br perovskite with IPA. The corresponding statistical data of the photovoltaic parameters (**Fig. 3.20 and Table 3.8**) of inorganic PSCs showed a strong dependency on the dipping time. When compared to the pristine sample, devices with 5 minutes of dipping time showed better performance which could be most likely ascribed due to improvement in the quality of the perovskite film.

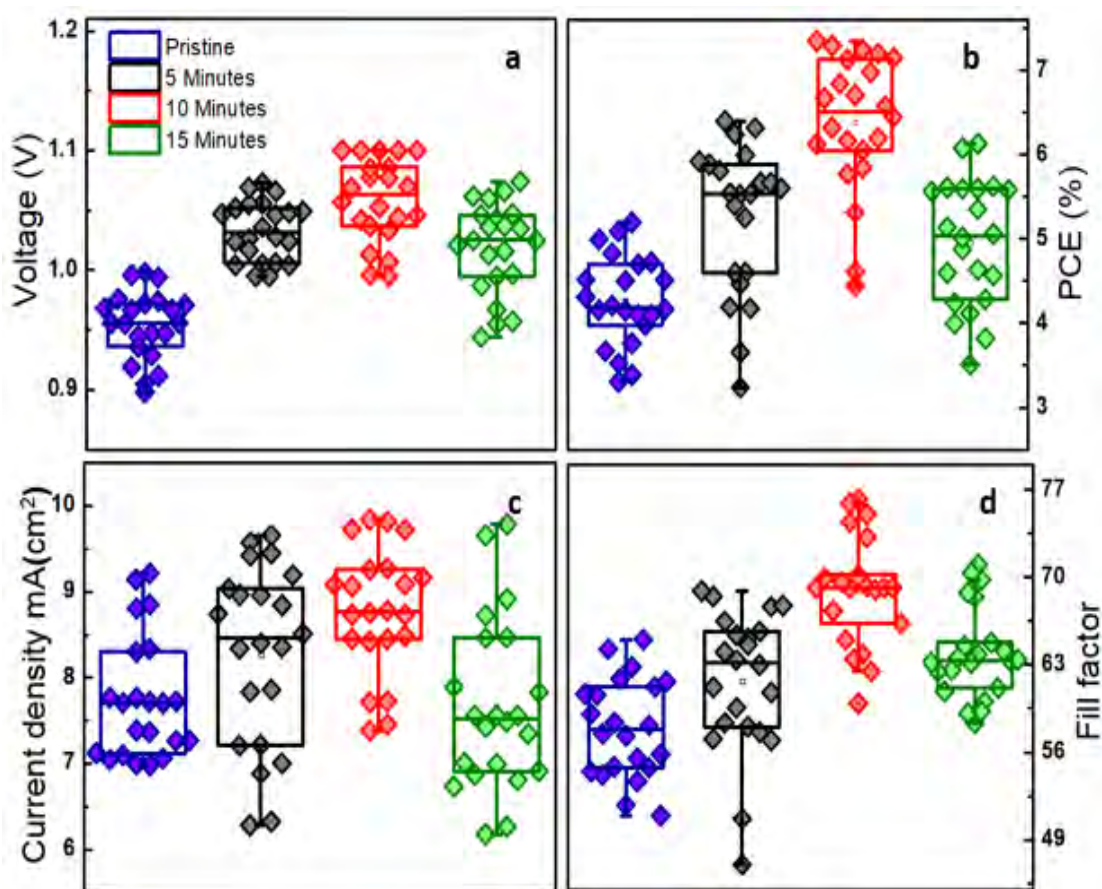


Figure 3.20: Statistical distribution of photovoltaic parameters (eleven devices of each type) for IPA post-treatment for different time.

Table 3.8. Photovoltaic parameters (average \pm std Deviation) of devices with IPA treatment for different time for eleven devices per data point (row 1) and champion device (row 2) under 1 Sun (100 mW/cm^2) illumination.

IPA Treatment minutes	J_{sc} (mA/cm^2)	V_{oc} (V)	FF (%)	PCE (%)	R_s (Ohm/cm^2)
0	7.7 ± 0.7	0.9 ± 0.02	0.58 ± 0.04	4.2 ± 0.5	
	(9.1)	(0.9)	(0.57)	(5.2)	(0.06)
5	8.3 ± 1.0	1.0 ± 0.02	0.62 ± 0.06	5.2 ± 0.9	
	(9.0)	(1.0)	(0.66)	(6.3)	(0.025)
10	8.6 ± 0.8	1.0 ± 0.04	0.68 ± 0.04	6.1 ± 0.9	
	(9.7)	(1.1)	(0.69)	(7.3)	(0.019)
15	7.6 ± 0.9	1.0 ± 0.03	0.64 ± 0.04	4.9 ± 0.7	
	(8.5)	(1.0)	(0.68)	(6.1)	(0.022)

The device performance was further increased by increasing the dipping time up to 10 minutes. The highest PCE (7.3%) was obtained at a dipping time of 10 minutes, which was selected further as the optimal time for further fabrication of devices. By increasing the dipping time further up to 15 minutes a decline in the FF and J_{sc} was observed (**Fig.3.20**). As depicted in **Table 3.8** the improvement of about 200 mV in the V_{oc} (1.10 V) was observed for the PSCs containing 10 mint IPA treated perovskite film as compared to the pristine devices (0.9 V). The improvement observed in the V_{oc} corresponds to efficient charge extraction, which was further evaluated by PL and PESA measurements, discussed later in this section.

Moreover, the IPA-treated device showed lower series resistance ($R_s = 0.019 \text{ Ohm/cm}^2$) compared to the pristine device ($R_s = 0.06 \text{ Ohm/cm}^2$) which led to an improvement in FF and ultimately PCE. The pristine device had a low PCE of 5.2%, a V_{oc} of 0.9 V, a J_{sc} of 9.1 mA cm^{-2} and a FF of 0.57. Notably, the IPA-treated device showed improved photovoltaic parameters (V_{oc} 1.1V, J_{sc} 9.7 mA cm^{-2} , FF 0.69, PCE 7.3%). The reduced hysteresis index (HI = 0.03) in IPA treated device as compared to pristine (HI= 0.13) would be most likely because of lower trap state density in the perovskite layer.¹⁷⁶

3.2.1.3. Photophysical Properties and their Impact on Device Performance

To get insight into improvement in device performance photo-physical properties were recorded by UV-Vis absorption and SSPL spectra of both pristine and IPA-treated

perovskite films. **Fig. 3.21(a)** presents the UV-Vis absorption spectra of the pristine and IPA-treated films. The two films showed the same absorption edge at 656 nm. However, a slight increase in the absorbance was detected for the IPA-treated film which implied that IPA-treated film can absorb more light. The emission spectra (**Fig. 3.21(b)**) showed that the emission peak of IPA-treated film is slightly red-shifted than that of the pristine perovskite film. This means that IPA treatment slightly altered the light absorption behavior of perovskite film which can contribute to improve the performance of PSC.

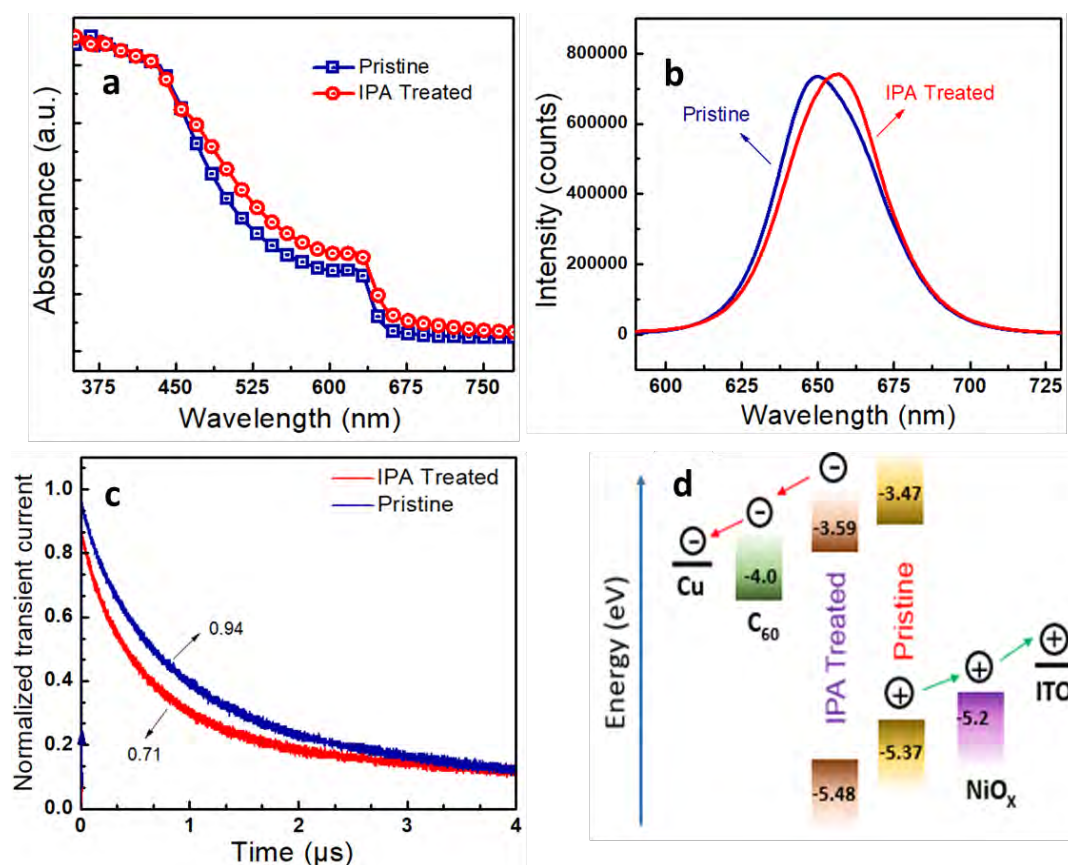


Figure 3.21: (a) UV-Vis absorption spectra. (b) SSPL spectra of pristine and IPA-treated perovskite on glass. (c) TPC measurements of pristine and IPA-treated devices. (d) Energy level diagram of each layer in the fabricated PSC stack.

The improved device performance was further analyzed by calculating carrier dynamics in the complete device stack using transient photocurrent (TPC) measurements as shown in **Fig. 3.21 (c)**. The results showed that rapid photocurrent decay is observed in the IPA-treated devices as compared to the pristine devices which confirms the better charge extraction capability of IPA-treated films. The obtained decay time for IPA treated device and pristine device is 0.71 and 0.94 μs , respectively. The IPA-treated device showed rapid photocurrent decay, well explaining the trend with the highest J_{sc} observed in **Fig. 3.20(c)**.

The SSPL and TRPL measurements were conducted further for the pristine and IPA-treated CsPbI₂Br films with the configuration of glass/ITO/NiO_x/CsPbI₂Br. The results are demonstrated in **Fig. 3.22(a and b)**.

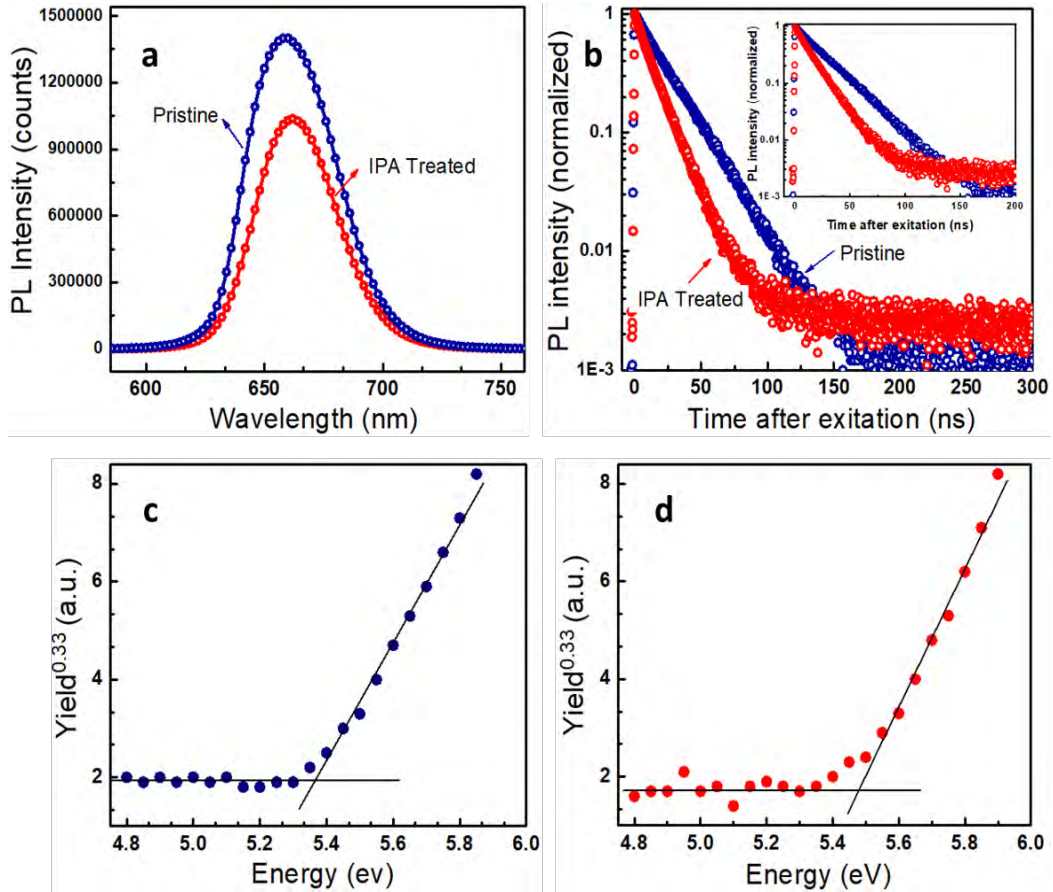


Figure 3.22: (a) SSPL and (b) TRPL spectra of the pristine and IPA-treated perovskite films on ITO/NiO_x. (c) PESA measurements of pristine and (d) IPA-treated thin films.

It is supposed that the higher PL quenching (i.e., lower PL intensity) corresponds to more efficient charge injection (or separation) from the light absorber material to the charge transport layer.¹⁷⁷ IPA treatment on perovskite surface remarkably reduced the PL intensity, indicating reduced defect density and enhanced hole extraction capability by the same HTL as compared to pristine perovskite film. Meanwhile, the TRPL measurement also showed a coherent result by PL decay lifetimes. **Fig. 3.22(b)** indicated PL decay curves which were further evaluated by a bi-exponential rate law:

$$f(t) = A_1 \exp(-t/\tau_1) + A_2 \exp(-t/\tau_2) \quad (3.1)$$

Where A_1 and A_2 represent the relative amplitudes, while τ_1 and τ_2 indicate the fast and slow recombination lifetimes respectively.¹⁷⁸ In perovskite/HTL samples, τ_1 is

associated with the process of charge extraction by HTL from perovskite, while τ_2 is ascribed to the trap-assisted non-radiative recombinations.¹⁷⁹ According to the TRPL fitting results, the pristine CsPbI₂Br/NiO_x sample had a τ_1 value of 24.5 ns while the IPA-treated CsPbI₂Br/NiO_x had a τ_1 value of 6.4 ns, indicating a more efficient extraction of charges at the NiO_x and IPA treated CsPbI₂Br interface. Furthermore, the IPA-treated CsPbI₂Br/NiO_x exhibited a larger τ_2 (15.4 ns) than pristine CsPbI₂Br/NiO_x (8.2 ns) demonstrating fewer defects which are in accordance with the result of SSPL.

To determine the VBM values, the PESA measurements of pristine and IPA-treated CsPbI₂Br based perovskite films was performed in the air. The energy level diagram of different layers used for the fabrication of PSCs is shown in **Fig. 3.21(d)**. The calculated VBM for pristine and IPA-treated CsPbI₂Br films was -5.37 and -5.48 eV as shown in **Fig. 3.22(c and d)**. The CBM values for pristine and IPA-treated perovskite are -3.47 and -3.59 eV which were determined from PESA and PL spectroscopy. The band edge positions of NiO_x and C₆₀ are taken from the literature.^{172,173} The CBM of IPA-treated CsPbI₂Br is slightly lower and nearer to the conduction band of C₆₀ as compared to pristine CsPbI₂Br which also effectively promotes efficient electron extraction. Interestingly, these results are also in excellent agreement with the results shown by TPC measurements.

3.2.1.4. Photovoltaic Performance and EQE Measurement

The J-V curves of the champion PSCs fabricated by the Pristine and IPA-treated CsPbI₂Br films under 100 mWcm⁻² illuminations are shown in **Fig. 3.23(a)**, and the corresponding photovoltaic parameters are summarized in **Table 3.9**. The best pristine device exhibited a low PCE of 8.2%, with a Voc of 1.00 V, a Jsc of 12.7 mA cm⁻², and a FF of 0.64. Notably, all the photovoltaic parameters for the IPA-treated PSC significantly improved (Voc 1.14 V, Jsc 13.0 mA cm⁻², FF 0.66), leading to a higher PCE of 9.7%.

EQE measurements were also carried out for best pristine and IPA-treated PSCs as shown in **Fig. 3.23(b)**. The IPA-treated PSC showed higher EQE values ranging from 350 nm to 650 nm with a maximal value of 87% as compared to the pristine device. The J_{SC} EQE calculated by integrating the EQE spectra yielded a J_{SC} of 12.9 mA cm⁻², and 13.5 mA cm⁻² for pristine and IPA-treated devices, respectively matching well with the J_{SC} (12.7 mA cm⁻² and 13 mA cm⁻²) obtained from J-V curves (**Fig. 3.23(a)**). This

significant enhancement in the performance of the devices treated with IPA is ascribed to the collective effects of improved charge collection property of the CsPbI₂Br films.

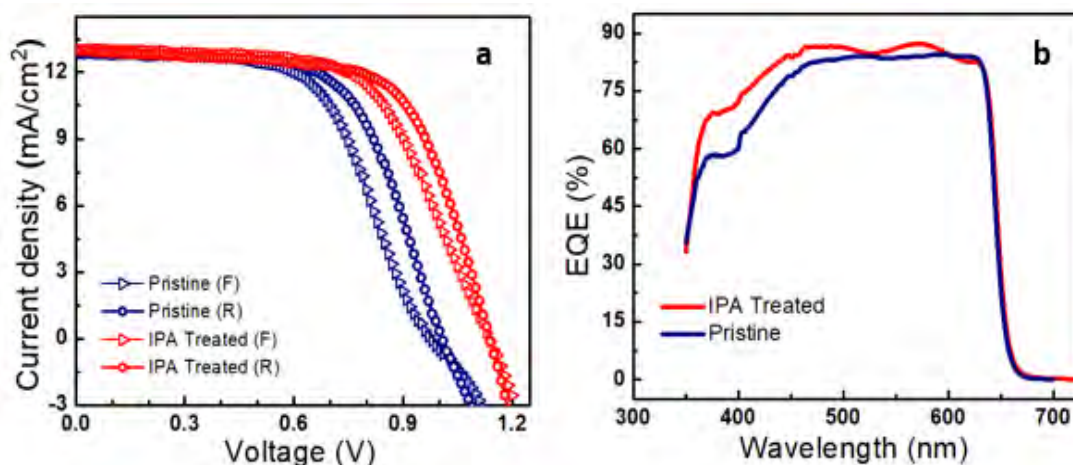


Figure 3.23: (a) Current density-voltage curves of the champion pristine and IPA treated cells measured at 1 Sun (100 mW/cm²) illumination. (b) EQE spectra of the best performing cells.

3.2.1.5. Device Stability

The PCE and J_{SC} of fabricated devices were further confirmed by MPPT for 300s (MPPT was conducted when the devices exhibited highest efficiency). **Fig. 3.24(a)** illustrates the photocurrent density and the corresponding stabilized PCEs. The performance of the fabricated PSCs remains unchanged even after continuous light soaking for 300 seconds, indicating that the stability of the device is not affected by the solvent treatment. After performing MPPT, the J-V curves of the CsPbI₂Br based PSCs were measured and depicted in **Fig. 3.24(b)**. The IPA-treated device showed a PCE of 9.8 %, a J_{SC} of 12.9 mA/cm² with a V_{OC} of 1.1 V and a FF of 0.68 in forward scan and a PCE of 10.0 %, a J_{SC} of 12.9 mA/cm² with a V_{OC} of 1.1 V and a FF of 0.69 in reverse scan. The IPA-treated device exhibited significantly improved efficiency and reduced hysteresis compared to the pristine device (**Table 3.9**). This improvement could be attributed to the decreased defect density and efficient electron extraction. The stability of pristine and IPA-treated PSCs as a function of storage time was also recorded. The devices were stored in the glovebox and measured under standard AM 1.5 illumination. The normalized PCE of the unencapsulated devices is shown in **Fig. 3.24(c)**. Both devices showed a similar trend. First, the device efficiency initially increased and remained unchanged 160 hours demonstrating that IPA post-treatment led to improved device performance without compromising stability.

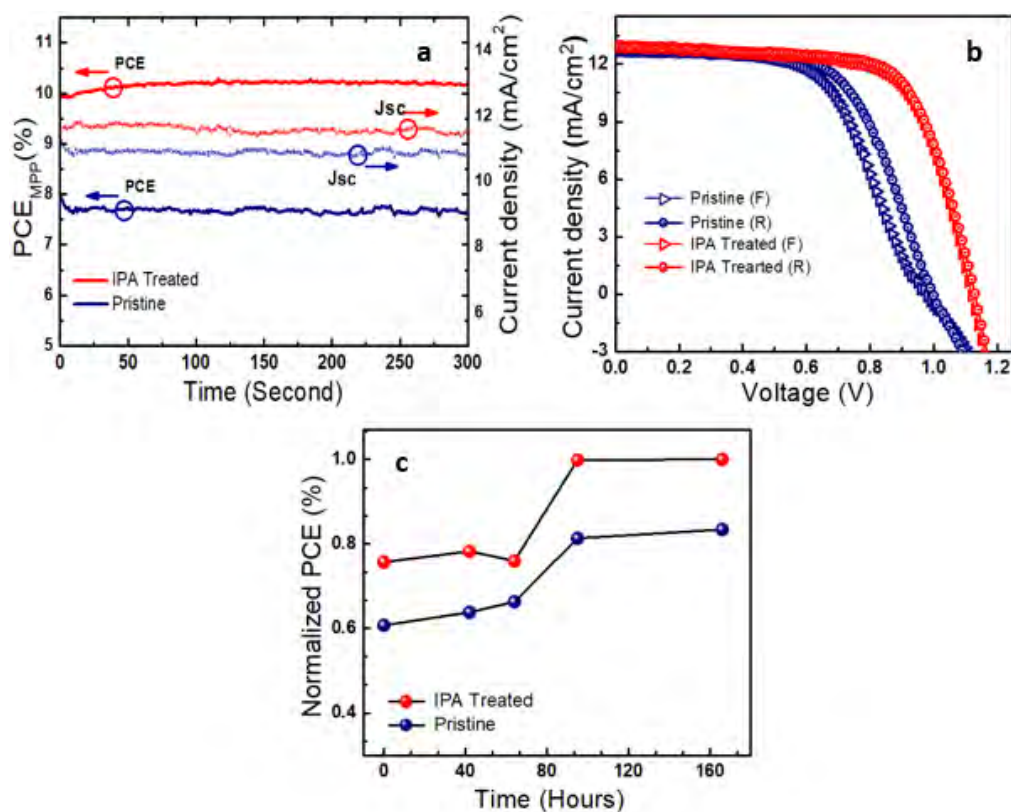


Figure 3.24: (a) Stabilized J_{sc} and PCE at MPP. (b) J-V curves of devices after MPPT. (c) Normalized PCEs of the pristine and IPA-treated PSCs as a function of storage time in the glovebox.

Table 3.9. Photovoltaic parameters of forward (F) and reverse (R) scan of champion pristine and IPA treated device measured before and after MPPT.

PSC device		J_{sc} (mA/cm ²)	V_{oc} (V)	FF (%)	PCE (%)	R_s (Ohm/cm ²)	HI
Pristine Before	(F)	12.9	0.97	0.60	7.4	(0.027)	0.1
	(R)	12.7	1.00	0.64	8.2	(0.025)	
After	(F)	12.70	0.97	0.59	7.2	(0.027)	0.08
	(R)	12.75	0.98	0.62	7.8	(0.025)	
IPA treated Before	(F)	13.0	1.13	0.62	9.1	(0.027)	0.06
	(R)	13.0	1.14	0.66	9.7	(0.016)	
After	(F)	12.9	1.11	0.68	9.8	(0.013)	0.02
	(R)	12.9	1.13	0.69	10.0	(0.013)	

Thus, a simple approach of surface treatment for CsPbI₂Br film was established which not only passivates perovskite defects but also facilitate the electron transfer from perovskite to ETL, leading to higher photovoltaic performance.

3.2.2. Amine-based Passivating Material to Improve the Performance of CsPbI₂Br Based Perovskite Solar Cells

This part demonstrate a defect post-passivating method to increase the performance of CsPbI₂Br based PSC having the architecture of ITO/NiO_x/CsPbI₂Br/EDA/C₆₀/LiF/Cu. The selected passivating material for CsPbI₂Br films is an amine-based material. The CsPbI₂Br films were prepared by a one-step spin-coating method as described in the device fabrication section. Afterward, a 0.009% solution of EDA in chlorobenzene was spin-coated on the top of the perovskite film.

3.2.2.1. Structural Analysis

The CsPbI₂Br films were subjected to XRD measurements to investigate the effect of EDA treatment on the crystallinity and phase purity of the perovskite.

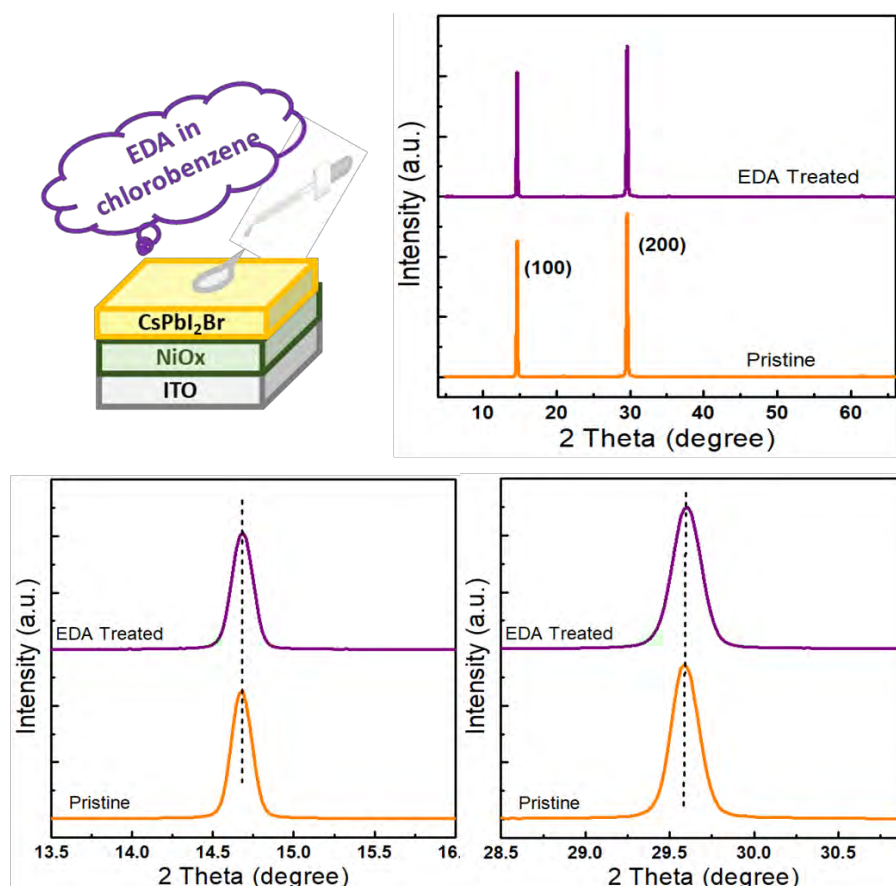


Figure 3.25: XRD pattern of the pristine and EDA treated CsPbI₂Br thin films.

As shown in **Fig. 3.25** both types of perovskites displayed intense diffraction peaks at 14.7° and 29.6° corresponding to the (100) and (200) lattice planes of the perovskite film. There is no prominent change in the peak position of perovskite films with or without treatment, indicating that the EDA molecule are not diffusing within the crystal

lattice of perovskite but only exist at the grain boundaries (GBs) or surfaces.

3.2.2.2. Morphological Studies

The surface morphology of the fabricated perovskite films was investigated by top-view SEM analysis. As shown in **Fig. 3.26(a)**, SEM images showed similar morphology with irregular grains.

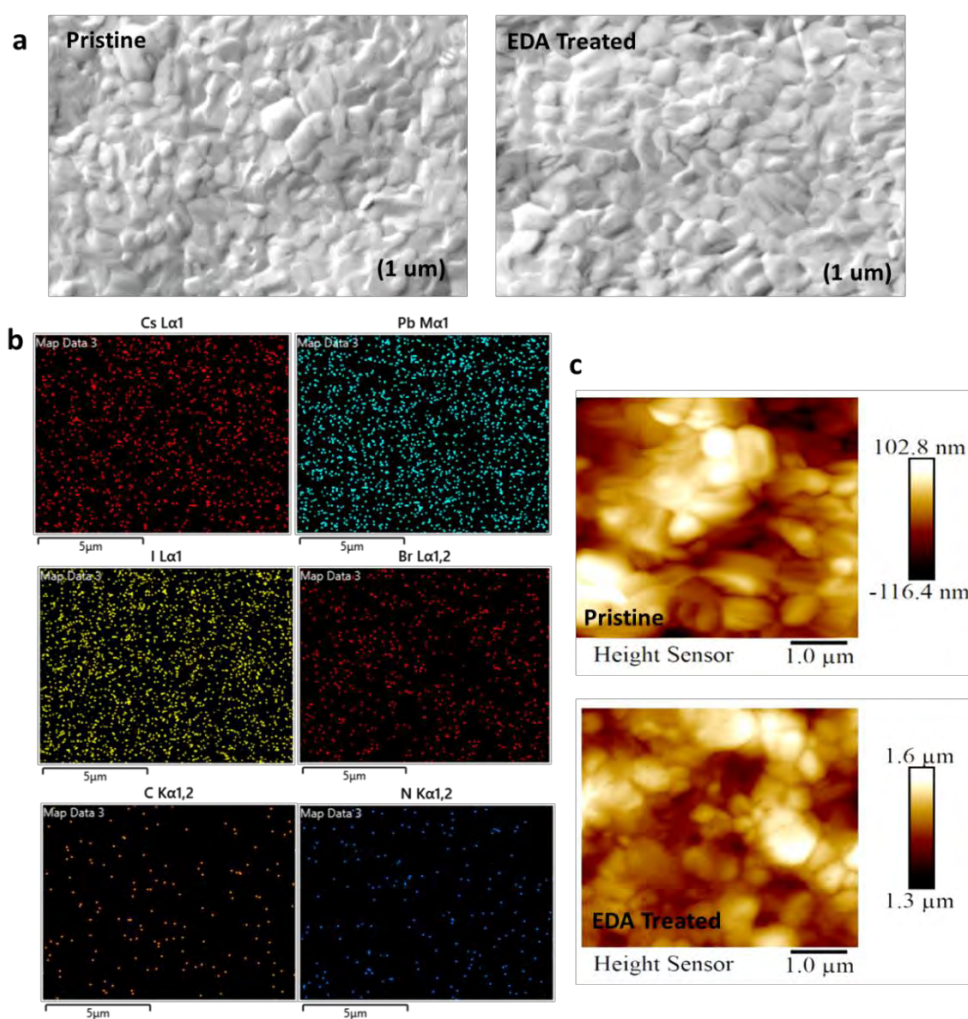


Figure 3.26: (a) Top-down SEM image (b) EDX elemental mapping of EDA treated film. (c) AFM images of pristine and EDA treated film.

To determine the distribution of the EDA through the perovskite film, EDX mapping on EDA-treated perovskite film was conducted as shown in **Fig. 3.26(b)**. The homogeneous distribution of Cs, Pb, I, and Br in the perovskite layer indicates the uniform distribution of perovskite elements. Notably, the presence of C and N elements in treated perovskite, is an element marker for EDA, while it is absent in the pristine perovskite. C and N elements are present throughout the entire treated perovskite layer, suggesting the existence of EDA on the perovskite layer. Furthermore, as EDA cannot

be incorporated into the perovskite lattice, as evidenced by XRD analysis, the molecule is most likely located at the surface or grain boundaries of the CsPbI₂Br film. AFM analysis also displayed no change in the morphology of perovskites as shown in Fig. 3.26(c) and revealed that passivation could result in a smoother film as shown by smaller RMS (33.8 nm) of EDA treated perovskite compared to pristine perovskite (RMS = 41.6 nm) which will help in efficient charge extraction.¹⁶⁴

3.2.2.3. X-ray Photoelectron Spectroscopic (XPS) Analysis

XPS is conducted for pristine and EDA-treated perovskite to investigate the interaction between CsPbI₂Br and EDA (Fig. 3.27).

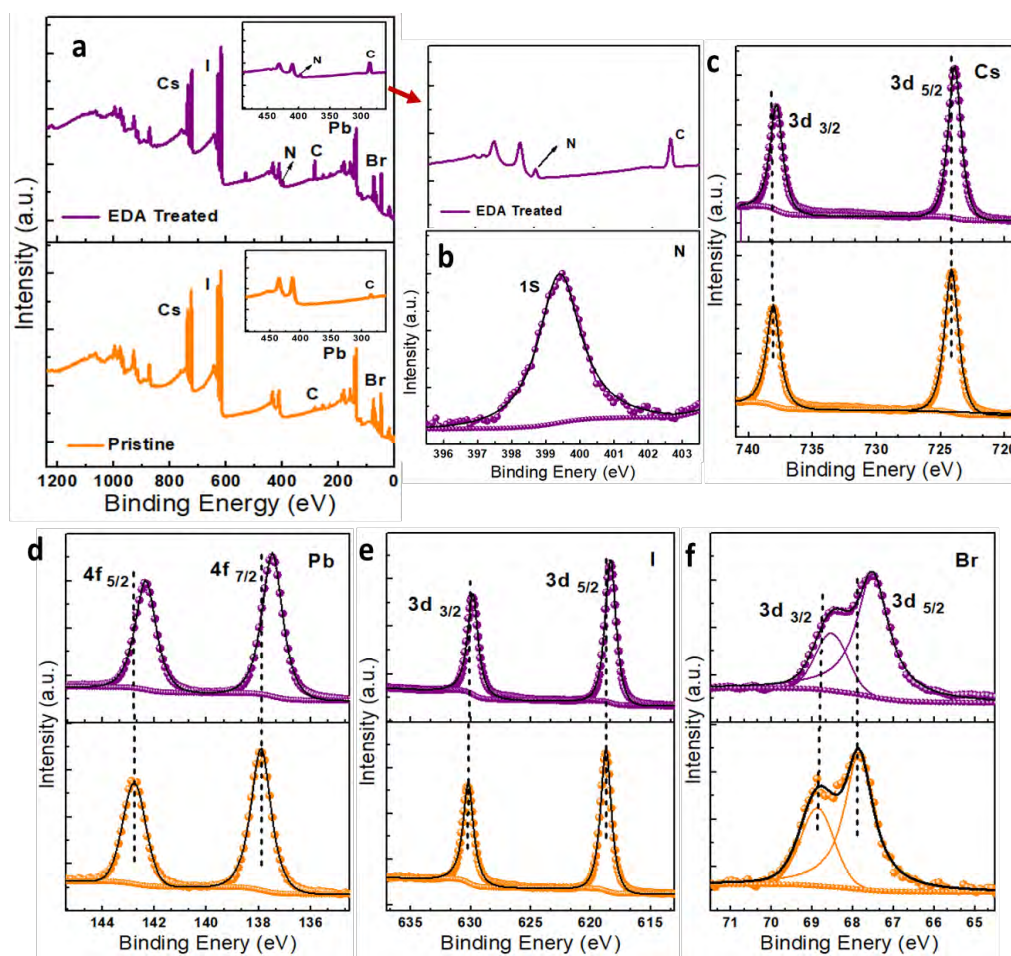


Figure 3.27: a) XPS survey spectra of pristine and EDA-treated CsPbI₂Br films. (b-f) Corresponding high-resolution XPS spectra of the N 1s, Cs 3d, Pb 4f, I 3d and Br 3d core levels, respectively.

The existence of EDA can be proved by the presence of N 1s peak and considerably higher C 1s peak at 284.6 eV in treated perovskite. Beside that, the binding energies of Pb 4f peaks in treated perovskite shifted to low binding energy confirming the interaction between uncoordinated Pb²⁺ and EDA which are typically identified as

recombination sites. Furthermore, the XPS peaks of Cs, I and Br 3d also showed similar variations which could be attributed to the increase in electron density on CsPbI₂Br surface, which originates from the transfer of electrons from N atoms in the amino group of the EDA to perovskite.

3.2.2.4. Photophysical Properties

To get insight into photophysical properties UV-Vis absorption and PL spectroscopy were carried out. The UV-Vis absorbance spectrum (**Fig. 3.28(a)**) depicts that the perovskite film absorbance was enhanced after EDA treatment.

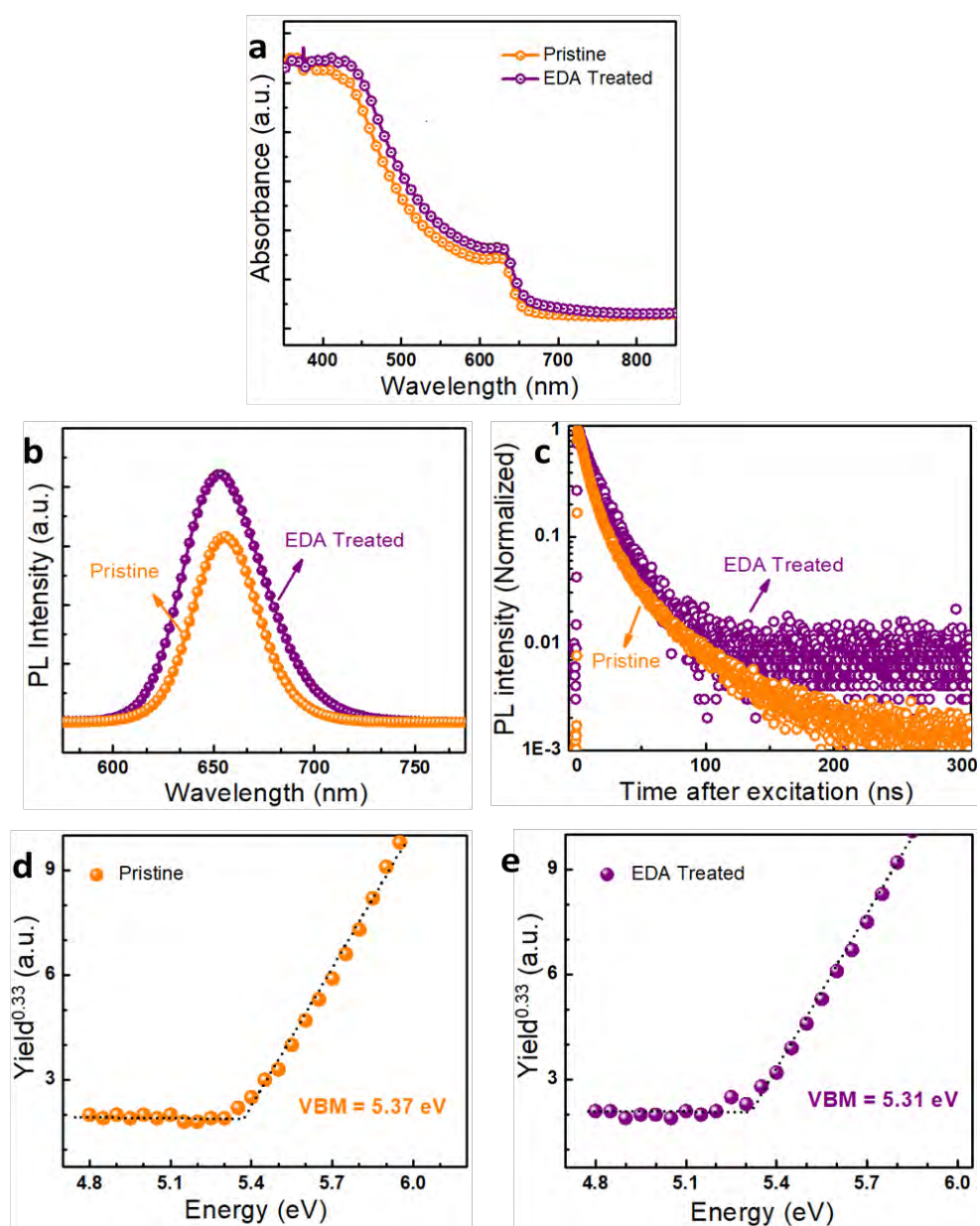


Figure 3.28: (a) UV-Visible absorption spectra (b) SSPL (c) TRPL spectra of perovskite films on glass. (d) PESA measurements of pristine and (e) EDA treated thin films.

The effect of EDA treatment on recombination dynamics of CsPbI₂Br films was investigated through SSPL and TRPL of the perovskite films on a glass substrate. Typically, higher PL intensity imply a reduction in non-radiative recombination.¹⁸⁰ Furthermore, a slight blueshift was also discerned along with enhanced PL intensity which also suggests defect passivation after EDA treatment.^{181–183} Secondly the TRPL spectra (**Fig. 3.28(c)**) revealed a longer carrier lifetime of the perovskite film subjected to EDA treatment. The corresponding TRPL fitting parameters are listed in **Table 3.10**. The τ_1 increased to 7.7 ns for treated perovskite film compared to 6.7 ns for the pristine film which manifests reduced nonradiative recombination at the interface and fewer defects in EDA treated perovskite.

Table 3.10. TRPL fitting parameters obtained by fitting the TRPL curve through the bi-exponential decay function.

Parameters	τ_1	τ_2	A ₁	A ₂
Pristine	6.7 ± 0.02	26.9 ± 0.20	0.8	0.2
EDA Treated	7.7 ± 0.44	18.3 ± 0.46	0.4	0.6

PESA measurements were carried out to study the effect of passivation on the surface band structure. As shown in **Fig. 3.28(d and e)** the calculated VBM values for pristine and treated perovskite are -5.37 eV and -5.31 eV respectively. This difference may lead to the efficient hole extraction from perovskite to NiO_x HTL in PSCs, thus feasibly minimizing hole recombination at the perovskite/HTL interface.

3.2.2.5. Device Performance and Process Optimization

The effect of EDA passivation on photovoltaic parameters was then studied by fabricating an inverted PSCs having architecture (ITO/NiO_x/CsPbI₂Br/EDA/C₆₀/LiF/Cu). The performance of the devices was evaluated, and the corresponding statistical distribution of photovoltaic parameters are summarized in **Table 3.11** and **Fig. 3.29**. The device without EDA passivation demonstrated an average V_{OC} of 0.97 V, a J_{SC} of 11.0 mAcm⁻², a FF of 0.55, and a PCE of 5.9% under 100 mWcm⁻² irradiation in the reverse scan direction. The photovoltaic parameters increased with increasing EDA concentration. With 0.009% EDA, solar cells exhibited the highest average PCE of 7.3 %, with a V_{OC} of 1.04 V, a J_{SC} of 11.9 mAcm⁻² and a FF of 0.57. The improvement in V_{OC} and FF for the passivated devices indicated that the perovskite surface defects have

been successfully passivated by EDA. With a further increase of the EDA concentration to 0.015%, the V_{OC} and FF exhibited a slight decrease, probably due of increase in internal series resistance because of insulating nature of EDA (Table 3.11) which also retards the charge transfer at the interface.¹⁸¹

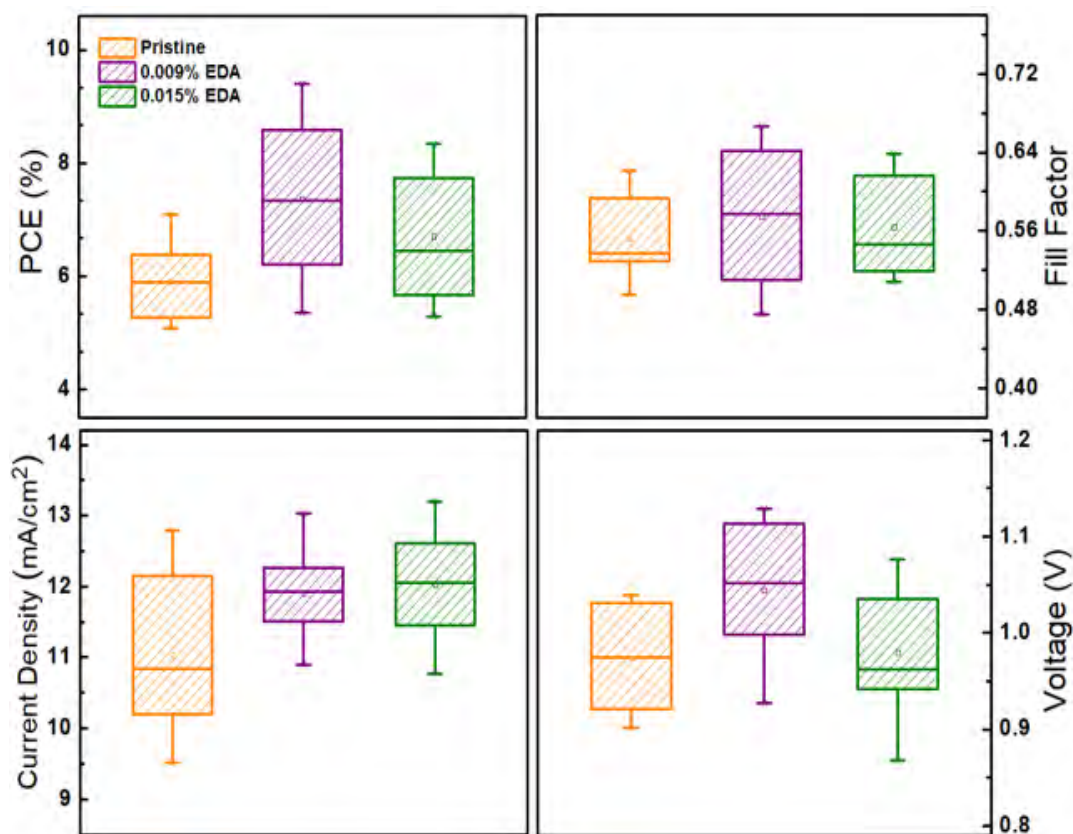


Figure 3.29: Statistical distribution of photovoltaic parameters (six devices of each type) for EDA treatment for different times.

Table 3.11. Photovoltaic parameters (average \pm std Deviation) of EDA treated devices for six devices per data point (row 1) and champion device (row 2) extracted from J-V measurements under 1 Sun (100 mW/cm^2) illumination.

EDA (%)	J_{sc} (mA/cm^2)	V_{oc} (V)	FF (%)	PCE (%)	R_s (Ohm/cm^2)
0	11.0 ± 1.14 (12.8)	0.97 ± 0.05 (1.03)	0.55 ± 0.03 (0.53)	5.9 ± 0.63 (7.1)	(0.028)
0.009%	11.9 ± 0.59 (12.5)	1.04 ± 0.07 (1.11)	0.57 ± 0.07 (0.66)	7.3 ± 1.41 (9.4)	(0.022)
0.015%	12.0 ± 0.76 (13.1)	0.97 ± 0.06 (0.97)	0.56 ± 0.05 (0.60)	6.7 ± 1.14 (8.3)	(0.029)

Based on the results from PESA measurements (Fig. 3.28(d and e)) energy level diagram of different layers in PSCs is constructed as depicted in Fig. 3.30(a). The J-V characteristics of champion pristine and EDA treated CsPbI₂Br based PSCs under 1 Sun (100 mW/cm²) illumination conditions are shown in Fig. 3.30(b). The pristine device has a low PCE of 7.1%, a V_{OC} of 1.03 V, with a J_{SC} of 12.8 mA cm⁻² and a FF of 0.53. Notably, the EDA treated device demonstrated improved photovoltaic parameters (V_{OC} 1.11 V, J_{SC} 12.5 mA cm⁻², FF 0.66) that results in a higher PCE of 9.4%. This improvement in the V_{OC} corresponds to defect passivation and efficient charge extraction, which is further evaluated by TPC measurements, later discussed in this section. Additionally, the EDA treated device exhibited lower series resistance (R_s = 0.022 Ohm/cm²) in comparison to the pristine device (R_s = 0.28 Ohm/cm²) which led to an enhancement in FF and PCE.

3.2.2.6. Transient Photocurrent (TPC) Measurements

The enhanced device performance by EDA treatment was further analyzed using TPC measurements which investigate the charge carrier extraction ability in the complete device stack as shown in Fig. 3.30(c).

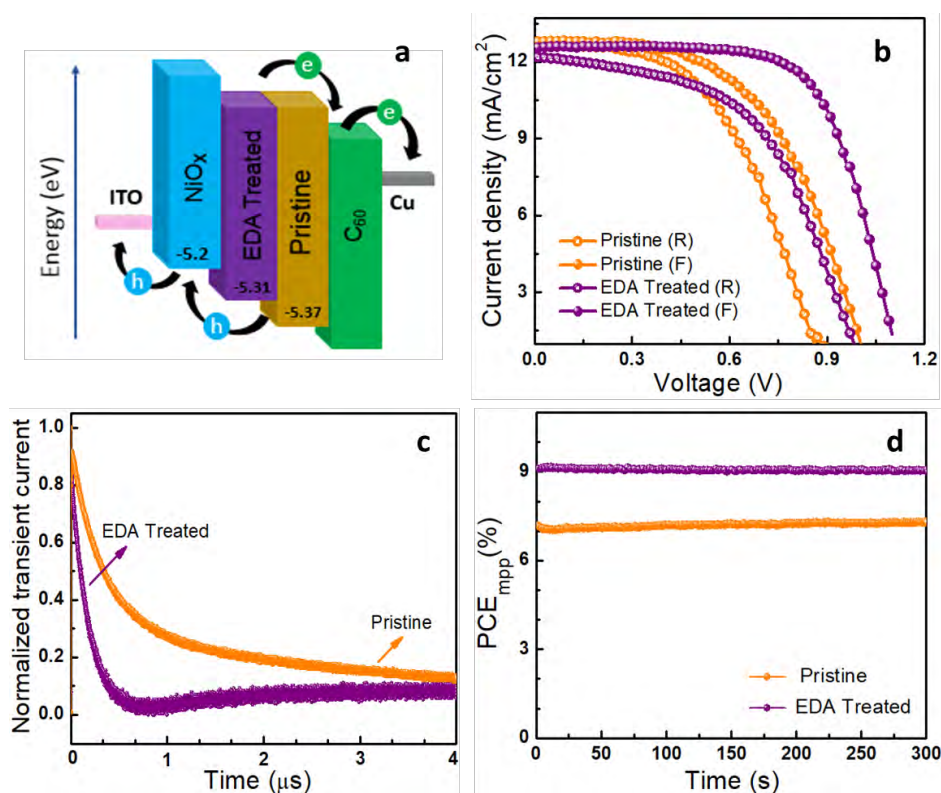


Figure 3.30: (a) Energy level diagram for fabricated PSCs. (b) J-V curves of the champion pristine and EDA treated cells measured at 1 Sun illumination. (c) TPC measurements of devices. (d) Stabilized PCE at MPP.

The photocurrent decay curve provides the correlation between the device performance and charge dynamics at short circuit current conditions. The TPC measurement demonstrated rapid photocurrent decay (short decay time) in the case of EDA treated device compared to the pristine device. This rapid decay indicates a better charge extraction ability for EDA treated device than the pristine which agrees with the high J_{sc} and FF values for the treated device. These results are consistent with PL and PESA measurements thus again affirming that passivation facilitates the charge extraction efficiency and leads to superior performance of PSCs.

3.2.2.7. Maximum Power-Point (MPP) Tracking

To further validate the performance of the PSCs, MPP tracking was carried out for both types of PSCs. The MPP tracking profiles (**Fig. 3.30(d)**) showed that fabricated PSCs retain their performance after continuous light soaking for 300 s showing that EDA treatment did not affect the stability of the device. The PCE values measured through MPP tracking of best devices are 7% and 9% for pristine and EDA treated devices respectively, which are in accordance with the PCE values obtained from J-V curves.

Thus, in summary, a simple and effective approach to improve the performance of PSCs by surface passivation was demonstrated. The simplest amine based passivating material EDA was used which neutralizes charge and prolongs the charge carrier lifetime within the device. As a result, the fabricated PSCs with EDA passivation demonstrated remarkably improved performance than that of the reference device.

3.3. Hybrid Harvester Device: Synergistic Solar and Mechanical Energy Conversion for Sustainable Energy Harvesting

To develop an effective strategy to simultaneously harvest multiple types of environmental energies, the concept of a hybrid energy harvester was proposed. This idea incorporates the photovoltaic and piezoelectric effect in a single device for solar and mechanical energy harvesting, to enable the efficient and complementary use of energy resources. Moreover, the development of a photovoltaic (PV) derived hybrid power system is the potential solution to mitigate the reliance on the weather for electricity production which is the main limitation of solar cells. Herein, a hybrid device was developed via the integration of a PSC and PENG which can harvest both solar energy and mechanical energy. The fabricated device has an architecture of PET/ITO/ZnO nanorods/IPPVP/spiro-OMeTAD/Au.

For the fabrication of the PSC/PENG hybrid device, an ITO-coated PET substrate was used. First, a ZnO seed layer was deposited on the top of the PET/ITO substrate by a spin coating method. Then, ZnO nanorods were synthesized on the top of ZnO seed layer. Subsequently, perovskite and spiro-OMeTAD layers were spin-coated on ZnO nanorods to form a p-i-n structure. Gold electrodes were deposited by thermal evaporation on the spiro-OMeTAD as the top electrode. Then, the flat copper strips were bonded to the PET/ITO and gold electrodes using conductive silver epoxy, followed by soldering of copper wires to the copper strips. Finally, the device was encapsulated in a lamination pouch by using a hot press. Detail of the device fabrication procedure is given in **section 2.3.2**.

As the measurement of hybrid harvester device were carried outside the glovebox in ambient condition so a perovskite with high moisture tolerance was needed. In the previous **section (3.1.1)** it was explained that slight change in the stoichiometry of CsPbI₂Br can enhance the ambient stability along with improved device performance. To further increase the phase stability of the resulting perovskite (non-stoichiometric (IP)) a different strategy was adopted which involve the addition of polymer into the perovskite. The polyvinylpyrrolidone (PVP) polymer was selected owing to its ability to increase the ambient stability of perovskite.¹⁸⁴⁻¹⁸⁶ This method involves the addition of different weight percent (1%, 1.5% and 2%) of PVP into the perovskite precursor solution followed by the fabrication of perovskite film by spin coating method as given in **section 2.3.2.3**.

3.3.1. Stability Measurements of Perovskite Films

To examine the effect of polymer on the phase stability of perovskite the IP and PVP incorporated perovskite films were exposed to ambient conditions (at room temperature, average humidity of 60-70%) and the results are shown in **Fig. 3.31(a)**. The IP film showed a change from the perovskite to the non-perovskite phase after being exposed to ambient conditions. However, PVP-incorporated perovskites (IPPVP) exhibited enhanced phase stability and with the increase in PVP percentage, it increased further demonstrating that the PVP addition can improve the phase stability of perovskite film. This enhanced phase stability could be attributed to the hydrophobicity of the PVP polymer and its strong interaction with the perovskite. Additionally, PVP molecules can absorb water and build a solid moisture barrier around the perovskite grains thus allowing only a very small amount of water to pass.¹⁸⁵

3.3.2. X-ray Diffraction (XRD) analysis

XRD measurements were performed to investigate the structure of the perovskite films with the addition of PVP, and the resultant pattern is shown in **Fig. 3.31(b)**.

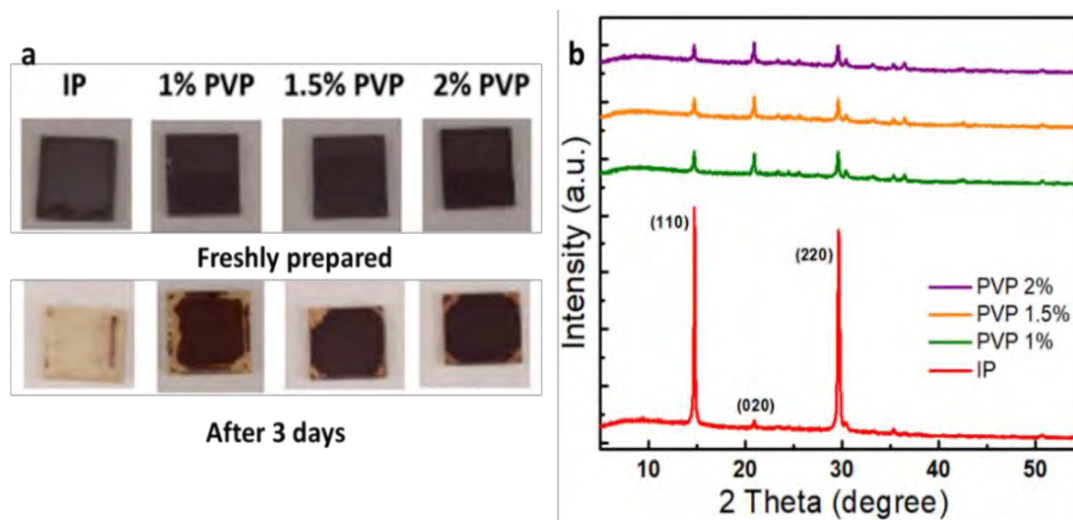


Figure 3.31: (a) Comparison of the air stability of the IP and IPPVP perovskite films. (b) XRD patterns of perovskite thin films.

For the controlled IP film, two prominent peaks at 14.7° and 29.7° correspond to (100) and (200) planes of a cubic perovskite phase, demonstrating the preferred growth orientation and high crystallinity of the perovskite.¹²³ However, with PVP addition to the perovskite several additional peaks have emerged which depicted that PVP incorporation changed the growth kinetics and crystallization of the perovskite. The crystallite size was calculated by using the Scherrer formula and found to be 47.90 nm (IP), 41.6 nm (IPPVP 1%), 40.8 nm, (IPPVP 1.5%) and 38.9 nm (IPPVP 2%). The crystallinity and crystallite size of the perovskite decreased with the addition of PVP and was found to be minimum in IPPVP 2%. Moreover, by the addition of PVP the intensity of the peaks at 14.7° and 29.7° significantly decreased while the intensity of the peak at 20.9° increased indicating that the interaction of PVP and perovskite resulted in an ordered arrangement of perovskite crystal.

3.3.3. UV-Visible Absorption and SEM Studies

The UV-Vis absorption spectra of pristine and PVP-incorporated perovskite films were investigated to analyze their light absorption ability and the corresponding absorbance spectra are shown in **Fig. 3.32(a)**. All perovskites (pristine and PVP-incorporated) have a comparable absorption edge with an absorption peak around 640 nm demonstrating the negligible effect of PVP on perovskite's electrical structure. This outcome is

understandable because PVP, being a non-conjugated polymer, does not exhibit absorption in the visible region. While the absorption of the PVP-incorporated perovskite is higher which is due to the increase in the thickness of the perovskite film with the addition of PVP as PVP addition increases the viscosity of perovskite precursor solution. The corresponding bandgaps of the pristine and PVP-incorporated perovskite films (**Fig. 3.32(b)**) showed slight variation, indicating the negligible effect of PVP on the optical bandgap.

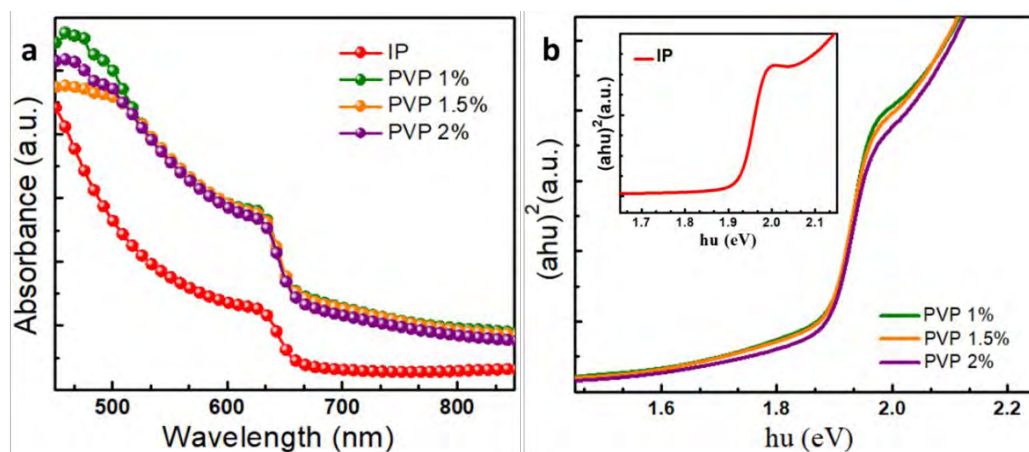


Figure 3.32: (a) UV-Visible absorption spectra. (b) Optical band gap spectra of IP and PVP incorporated perovskite thin films.

Top-view SEM images were used to study the surface morphology of IP and IPPVP perovskite films. As given in **section 3.1.1 Fig. 3.4(a)** the IP perovskite film showed compact morphology with irregular grains while in the case of PVP-incorporated perovskite **Fig. 3.33(a and b)** the grain size enlarged. However, the gaps between grains appeared to be visible and can be increased by further increasing the amount of PVP. It can cause undesirable interfacial charge recombination, and an increased number of shunting paths, leading to inferior photovoltaic performance of PSC. Additionally, the conductivity of PVP is poor,¹⁸⁷ so the higher concentration of PVP can damage the charge carrier mobility inside the perovskite layer and impair the performance of PSC. Thus IPPVP 1.5% was selected for device fabrication to provide a trade-off between phase stability and efficiency. **Fig. 3.33(c and d)** displayed the top and side view SEM image of IPPVP 1.5% on ZnO nanorods. Side view SEM images showed that perovskite film is thick enough to cover the ZnO nanorods which is important for the efficient operation of PSC. Moreover, EDX mapping **Fig. 3.33(e)** confirmed the presence and uniform distribution of PVP within the perovskite layer.

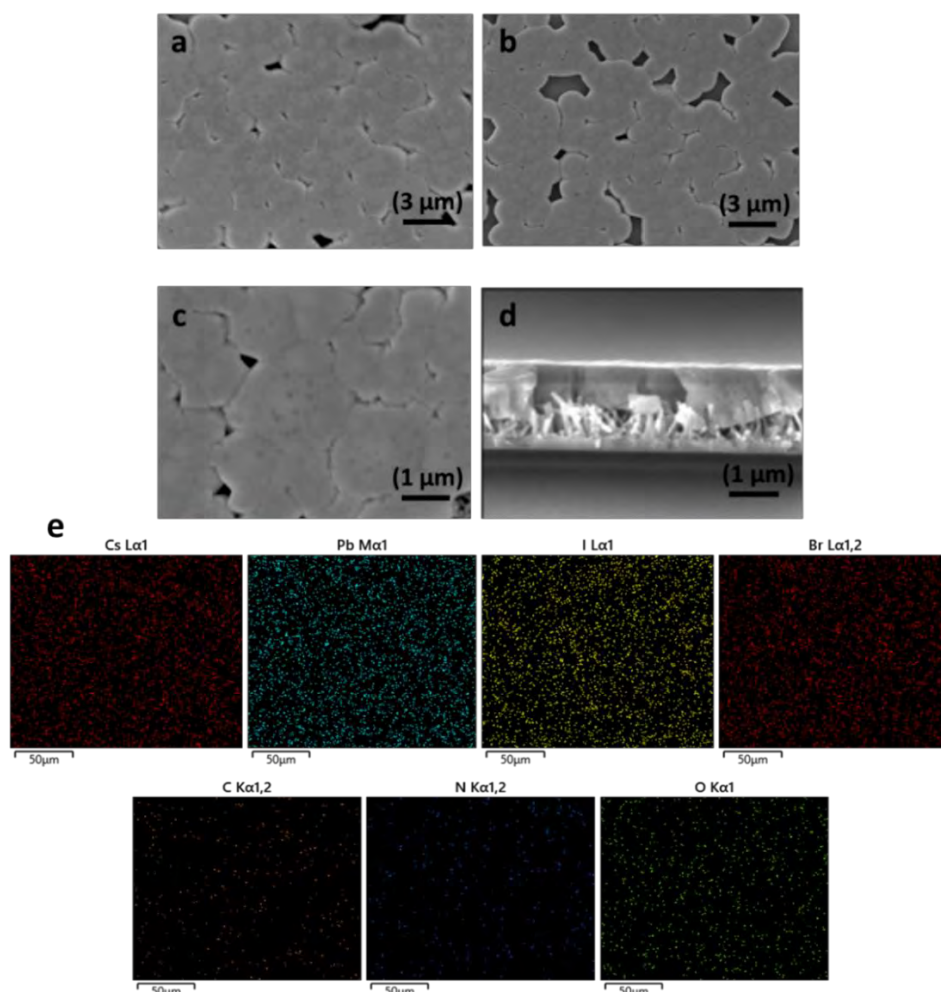


Figure 3.33: Top view SEM images on glass/ITO substrate (a) IPPVP 1.5% (b) IPPVP 2%. (c) Top view and (d) Side view SEM image of IPPVP 1.5% on PET/ITO/ZnO nanorods. (e) EDX elemental mapping of IPPVP 1.5% perovskite film on glass/ITO substrate.

3.3.4. X-ray Photoelectron Spectroscopic (XPS) Analysis

To further understand the effect of PVP on the chemical environment of perovskite the XPS analysis was carried out and the resultant spectra are shown in **Fig. 3.34**. The corresponding survey spectrum is shown in **Fig. 3.34(a)** which showed all the characteristic peaks of Cs 3d, Pb 4f, I 3d and Br 3d confirming the composition of the IP perovskite films. However, the appearance of the N 1s, along with higher intensity C and O 1s signals in the IPPVP perovskite film indicated the presence of PVP. Additionally, the C 1s spectrum (**Fig. 3.34(h)**) of IPPVP showed clear signals of N–C and O=C further confirming the existence of PVP in the final perovskite. Meanwhile, owing to the electron-donating properties of the C=O groups of PVP, the XPS peaks of Pb 4f_{5/2} and 4f_{7/2} slightly shifted toward lower binding energy demonstrating the

interaction between uncoordinated Pb^{2+} ions and PVP, which are often recognized as recombination sites.^{188,189}

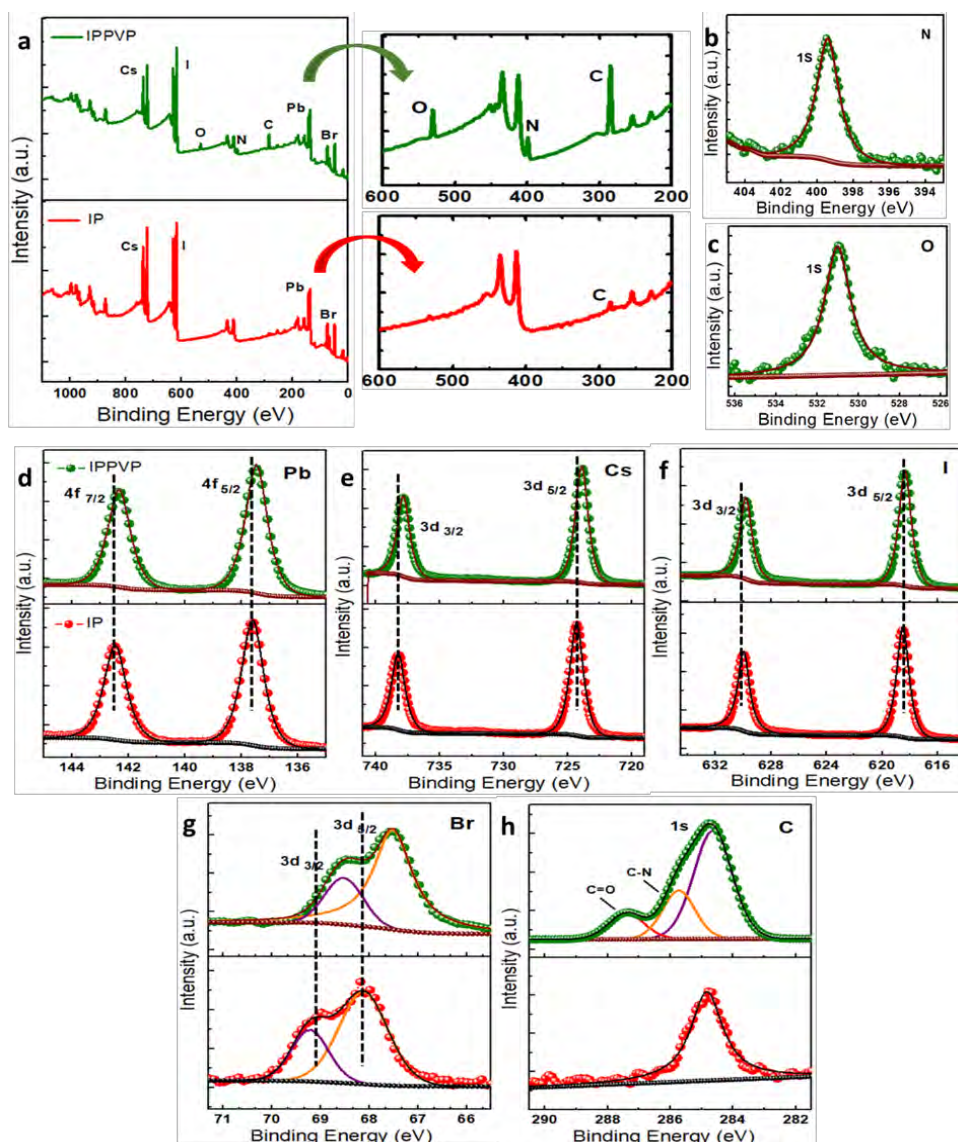


Figure 3.34: (a) XPS survey spectra of IP and IPPVP 1.5% perovskite thin films, (b) N 1s, (c) O 1s, (d) Pb 4f, (e) Cs 3d, (f) I 3d, (g) Br 3d and (h) C 1s spectra.

In addition, the XPS peaks of Cs 3d, I 3d and Br 3d also showed similar pattern, again confirming the chemical interaction between PVP and the perovskite lattice instead of being physically adsorbed on the surface.

3.3.5. Hybrid Device Performance

The hybrid device was fabricated with the architecture of PET/ITO/ZnO nanorods/IPPVP 1.5%/spiro/Au shown in **Fig. 3.35(a)**. To operate the hybrid system, we tested the PSC and PENG separately. The characteristic J-V curves of the fabricated device are shown in **Fig. 3.35(b)**.

The photovoltaic parameters calculated from J-V curve showed that the device achieved a PCE of 2.27%, with a J_{SC} of 12.6 mA/cm², a V_{OC} of 0.69 V and a FF of 0.26 in the forward scan and a PCE of 2.32% with a J_{SC} of 12.9 mA/cm², a V_{OC} of 0.69 V, and a FF of 0.26 in the reverse scan with negligible hysteresis. Moreover, the device exhibited a R_s of 53.7 and 49.5 Ohm/cm² in the forward and reverse scan respectively. This high value of R_s is responsible for low FF of the device as shown by J-V curve.

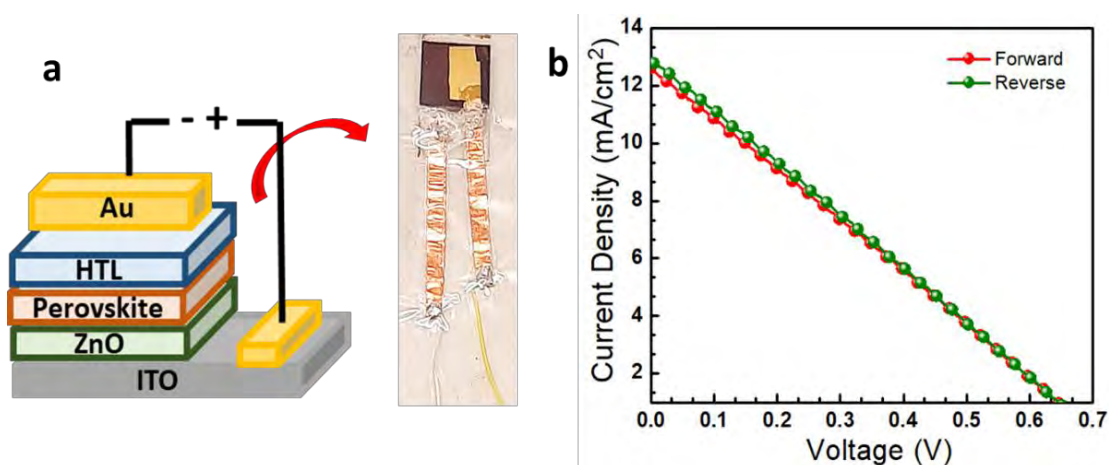


Figure 3.35: (a) Architecture of the fabricated hybrid device. (b) J-V curves of the PSC (active area of 0.25 cm²) measured under 1 Sun (100 mW/cm²) illumination.

The performance of the PENG was measured using a permanent magnetic shaker (**Fig. 3.36(a)**), by employing a mass-spring system to apply controlled and repeatable strain to the device. The nanogenerator was affixed to a metal cantilever having a tip mass of 30 g, operating at different resonant frequencies. **Fig. 3.36(b)** showed the fabricated device tested at frequencies ranging from 27 to 33 Hz. These results indicated that with the increase in shaking frequency the output voltage of the device also increases. This aligns with expectations for a cantilever system, as it reaches to its resonant frequency. At this point, significantly higher displacements and strains are observed, leading to enhanced performance of the nanogenerator. The nanogenerator signal at the resonant frequency of 31 Hz is displayed in **Fig. 3.36(c)**. Under this condition the PENG exhibited an open circuit voltage vary between 1.4 V to -1.5 V. This observation confirms the successful mechanical energy harvesting ability of the fabricated device. When the nanogenerator was bent, the strain was induced along the ZnO nanorods, resulting in the piezoelectric effect and subsequent charge displacement, ultimately leading to the measured voltage. However, once the charge was fully screened, the net surface charge diminished.¹⁵⁷

Furthermore, to test the practical implementation of the harvested energy the device was connected to external resistive loads (100 Ω to 10 M Ω) to measure the maximum output power. **Fig. 3.36(d)** showed the output power of this device under shaking and tapping mode (to further investigate the effect of impacting force the same device was tested by tapping the device with insulating material along with shaking) and produced a maximum output power of 0.35 $\mu\text{W}/\text{cm}^2$ for shaking and 0.79 μW for tapping at 10 and 9 M Ω resistance respectively at a resonant frequency of 31Hz. These results showed that output power increases as the impacting force increases.

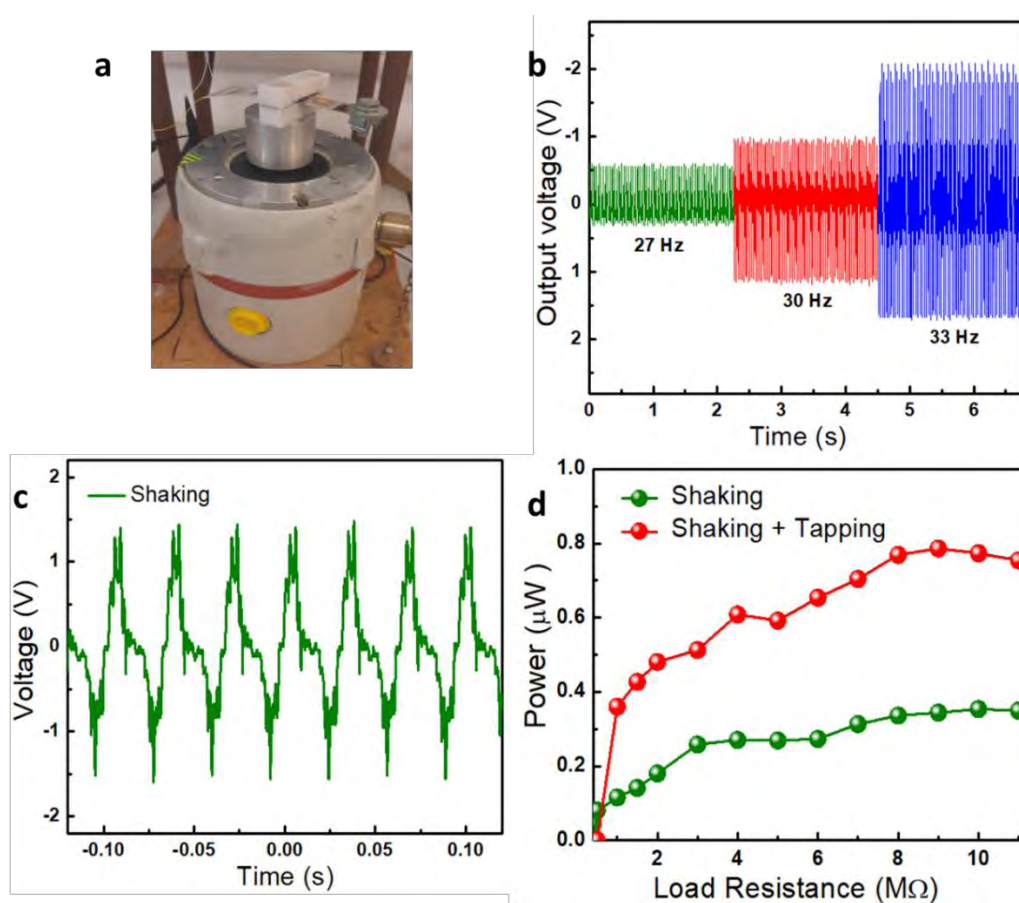


Figure 3.36: (a) Magnetic shaker to test PENG performance. (b) Voltage-time scan of PENG nanogenerator by shaking at 27 Hz, 30 Hz and 33 Hz. (c) Voltage-time scan of PENG by shaking at 31 Hz on a cantilever. (d) The output power of device shaking and shaking + tapping at 31 Hz.

In summary, we have developed a PSC/PENG hybrid system in a single device and demonstrated their use in solar and mechanical energy conversion for sustainable energy harvesting. Thus, this work presents an important accomplishment in the field of renewable energy generation by successfully combining PSC/PENG hybrid systems in a single device.

Conclusions

Organic-inorganic hybrid lead halide perovskite solar cells have amassed immense research attention among photovoltaic technologies. However, the poor thermal stability of their volatile organic cations becomes a major obstacle to their commercialization. Recent research proposes that by utilizing inorganic cations such as Cs^+ to replace volatile organic ions, the environmental tolerance of PSCs can be enhanced. Thus, among Cs based perovskites CsPbI_2Br perovskite offers a tradeoff between light absorption and phase stability and has been regarded as the most practical photoactive absorber material. In this work, we have demonstrated different strategies to improve the stability and performance of CsPbI_2Br based PSCs. The results are summarized as follows:

In the first section, the effect of change in the stoichiometry of CsPbI_2Br perovskite on device performance and stability was investigated by employing both stoichiometric and non-stoichiometric perovskite as absorber layer in PSC. The non-stoichiometric perovskite exhibited enhanced stability and more favorable energetics for charge extraction, lower non-radiative recombination, and better photovoltaic characteristics than its stoichiometric counterpart. The performance of non-stoichiometric devices was further improved by the optimization of charge transport layers. Comparing the performance of devices, it was observed that devices fabricated with solution-processed NiO_x outperformed those with sputtered NiO_x films. Additionally, on the ETL side, the 20 nm C_{60} demonstrated to be capable of effectively enhancing charge extraction and reducing leakage loss. This led to an optimum champion device that showed a PCE of 7.5% with a V_{OC} of 1.02 V, J_{SC} of 12.7 mA/cm^2 and a FF of 0.58.

Afterward B-site doping strategy was used to improve the PCE of non-stoichiometric perovskite based PSCs. For that, an appropriate amount of CuBr_2 salt was directly added to the non-stoichiometric $\text{CsPb}_{1-x}\text{I}_{2-x}\text{Br}$ perovskite precursor solution. As the ionic radius of Cu^{2+} (0.72 Å) is shorter than that of Pb^{2+} (1.19 Å), so it can partially replace the Pb^{2+} ions in the crystal lattice of $\text{CsPb}_{1-x}\text{I}_{2-x}\text{Br}$ perovskite and can enhance formation energy. The structural, photophysical and morphological analysis confirmed the presence of Cu^{2+} and demonstrated that an optimal amount of Cu^{2+} can enhance the optoelectronic properties, reduce the defects and trap states in perovskite film thus aiding charge separation and preventing undesirable charge carrier recombination.

Advancing from the merits discussed earlier, a maximum PCE of 8.4% was obtained with an IPCu-based device. Thus, this work offers an effective strategy to improve the performance of PSCs and open up a new route for the fabrication of efficient PSCs.

In the second section, surface treatment of CsPbI₂Br perovskite was done by using two different strategies. One was the surface treatment of the CsPbI₂Br perovskite film with green solvent isopropanol (IPA) while another was the defect post-passivation via Lewis acid base passivation method using amine-based passivation material. The IPA treated CsPbI₂Br absorber layer showed reduced defect density and, has energetically more favorable energy level alignment with the C₆₀ ETL which enables the efficient charge transfer and mitigates the energy loss at the interface of CsPbI₂Br/C₆₀. The resultant PSC led to a 30% improvement in the photovoltaic performance with a maximum PCE of 10%. In addition, the devices exhibited reduced hysteresis and good stability without any sign of degradation for 160 hours.

In case of Lewis acid base passivation, the simplest amine based passivated material EDA was used which formed a bond with uncoordinated lead atoms of CsPbI₂Br perovskite by its nitrogen atoms. This passivation neutralized charge, reduced the surface trap states and prolonged the charge carrier lifetime within the PSC. Additionally, EDA passivation also shifted the perovskite layer energy band edge in the positive direction thus facilitating the interfacial hole transfer. Consequently, the PSCs fabricated with EDA passivation exhibited significantly improved V_{OC} and FF and a champion PCE of 9.4%, higher than that of reference device (7.3%) under 100 mWcm⁻² illumination. As a result, this study offers an effective strategy to fabricate high-quality CsPbI₂Br films that can be employed not only in PSCs but also for other optoelectronic devices.

In the third section, a PSC/PENG hybrid system was developed in a single device and demonstrated their use in solar and mechanical energy conversion for sustainable energy harvesting. A normal device with an architecture of PET/ITO/ZnO nanorods/IPPVP/spiro-OMeTAD/Au was selected where the perovskite absorber layer (IPPVP) absorbed the solar energy and the piezoelectric nature of ZnO nanorods acted as a mechanical energy harvester unit. For a single PSC unit, a V_{OC} of 0.69 V and a J_{SC} of 12.91 mA cm⁻² was achieved, corresponding to an overall PCE of 2.31%. The PENG can take advantage of different motions, to deliver an output power of up to 0.79 μW. Thus, this study presents a significant achievement in the realm of renewable energy

generation by successfully integrating PSC/PENG hybrid systems into a single device. This groundbreaking development paves the way for scaling up renewable energy production, even in varying weather conditions. Furthermore, these results suggest a new pathway for the development of cost-effective and high-performance flexible optoelectronic devices.

Future Recommendations

Based on the findings and limitations identified in this research, the following future recommendations are proposed to further advance the field of inorganic perovskite based PSCs.

- Modification of the perovskite layer through doping or partial incorporation of metal ions that can enhance the intrinsic stability to withstand worse environmental conditions.
- Fabrication of perovskite layer by antisolvent methods using green anti-solvents that will improve the perovskite layer crystallization through efficient evaporation of solvent. As a result, larger grain size with reduced defect states can be obtained.
- Interface engineering for efficient charge transport through different interfaces can also be done either using suitable modifiers or introducing inexpensive inorganic CTLs, or alloying them for better energy-level alignment.
- Despite significant advancement in all-inorganic PSCs, there are still few reports on flexible and large area all-inorganic PSCs, so this research domain can also be investigated.
- Use of different modifiers and perovskite material in hybrid energy harvester to further improve the performance of hybrid harvester devices.

References

- (1) Romitti, Y.; Sue Wing, I. Heterogeneous Climate Change Impacts on Electricity Demand in World Cities circa Mid-Century. *Sci. Rep.* **2022**, *12* (1), 4280.
- (2) Shahsavari, A.; Akbari, M. Potential of Solar Energy in Developing Countries for Reducing Energy-Related Emissions. *Renew. Sustain. Energy Rev.* **2018**, *90*, 275–291.
- (3) Armaroli, N.; Balzani, V. The Future of Energy Supply: Challenges and Opportunities. *Angew. Chemie Int. Ed.* **2007**, *46* (1-2), 52–66.
- (4) Roy, P.; Sinha, N. K.; Tiwari, S.; Khare, A. A Review on Perovskite Solar Cells: Evolution of Architecture, Fabrication Techniques, Commercialization Issues and Status. *Sol. Energy* **2020**, *198*, 665–688.
- (5) Sebastian, N. Limiting Approach to Generalized Gamma Bessel Model via Fractional Calculus and Its Applications in Various Disciplines. *Axioms* **2015**, *4* (3), 385–399.
- (6) Anaya, M.; Lozano, G.; Calvo, M. E.; Míguez, H. ABX₃ Perovskites for Tandem Solar Cells. *Joule* **2017**, *1* (4), 769–793.
- (7) Jordan, P. G. *Solar Energy Markets*; Elsevier **2014**.
- (8) Chapin, D. M.; Fuller, C. S.; Pearson, G. L. A New Silicon P-n Junction Photocell for Converting Solar Radiation into Electrical Power. *J. Appl. Phys.* **1954**, *25* (5), 676–677.
- (9) Lincot, D. The New Paradigm of Photovoltaics: From Powering Satellites to Powering Humanity. *Comptes Rendus Phys.* **2017**, *18* (7–8), 381–390.
- (10) Pockett, A. Characterization of Perovskite Solar Cells. Doctoral dissertation, University of Bath 2016.
- (11) Green, M. A. Corrigendum to ‘Solar Cell Efficiency Tables (Version 49)’[Prog. Photovolt: Res. Appl. 2017; 25: 3–13]. *Prog. Photovoltaics Res. Appl.* **2017**, *25* (4), 333–334.
- (12) Sharma, S.; Jain, K. K.; Sharma, A. Solar Cells: In Research and Applications—a Review. *Mater. Sci. Appl.* **2015**, *6* (12), 1145.
- (13) Mahapatra, A.; Kumar, S.; Kumar, P.; Pradhan, B. Recent Progress in Perovskite Solar Cells: Challenges from Efficiency to Stability. *Mater. Today Chem.* **2022**, *23*, 100686.
- (14) Park, S.; Lee, C.; Kim, T.; Ko, Y.; Jun, Y. Direct Interface Engineering Using Dopant of Hole Transport Layer for Efficient Inorganic Perovskite Solar Cells. *Mater. Today Chem.* **2023**, *30*, 101551.
- (15) Chilvery, A. K.; Batra, A. K.; Yang, B.; Xiao, K.; Guggilla, P.; Aggarwal, M. D.; Surabhi, R.; Lal, R. B.; Currie, J. R.; Penn, B. G. Perovskites: Transforming Photovoltaics, a Mini-Review. *J. Photonics Energy* **2015**, *5* (1), 57402.
- (16) Green, M. A.; Ho-Baillie, A.; Snaith, H. J. The Emergence of Perovskite Solar Cells. *Nat. Photonics* **2014**, *8* (7), 506–514.
- (17) Di Giacomo, F.; Fakharuddin, A.; Jose, R.; Brown, T. M. Progress, Challenges

- and Perspectives in Flexible Perovskite Solar Cells. *Energy Environ. Sci.* **2016**, *9* (10), 3007–3035.
- (18) Xiao, J.; Liu, L.; Zhang, D.; De Marco, N.; Lee, J.; Lin, O.; Chen, Q.; Yang, Y. The Emergence of the Mixed Perovskites and Their Applications as Solar Cells. *Adv. Energy Mater.* **2017**, *7* (20), 1700491.
- (19) Zhu, Z.; Sun, Q.; Zhang, Z.; Dai, J.; Xing, G.; Li, S.; Huang, X.; Huang, W. Metal Halide Perovskites: Stability and Sensing-Ability. *J. Mater. Chem. C* **2018**, *6* (38), 10121–10137.
- (20) Park, J. H.; Seo, J.; Park, S.; Shin, S. S.; Kim, Y. C.; Jeon, N. J.; Shin, H.; Ahn, T. K.; Noh, J. H.; Yoon, S. C. Efficient $\text{CH}_3\text{NH}_3\text{PbI}_3$ Perovskite Solar Cells Employing Nanostructured P-type NiO Electrode Formed by a Pulsed Laser Deposition. *Adv. Mater.* **2015**, *27* (27), 4013–4019.
- (21) Almora, O.; Vaillant-Roca, L.; Garcia-Belmonte, G. Perovskite Solar Cells: A Brief Introduction and Some Remarks. *Rev. Cuba. Fis.* **2017**, *34* (1), 58–68.
- (22) Li, Z.; Yang, M.; Park, J.-S.; Wei, S.-H.; Berry, J. J.; Zhu, K. Stabilizing Perovskite Structures by Tuning Tolerance Factor: Formation of Formamidinium and Cesium Lead Iodide Solid-State Alloys. *Chem. Mater.* **2016**, *28* (1), 284–292.
- (23) Sato, T.; Takagi, S.; Deledda, S.; Hauback, B. C.; Orimo, S. Extending the Applicability of the Goldschmidt Tolerance Factor to Arbitrary Ionic Compounds. *Sci. Rep.* **2016**, *6* (1), 1–10.
- (24) Travis, W.; Glover, E. N. K.; Bronstein, H.; Scanlon, D. O.; Palgrave, R. G. On the Application of the Tolerance Factor to Inorganic and Hybrid Halide Perovskites: A Revised System. *Chem. Sci.* **2016**, *7* (7), 4548–4556.
- (25) Steele, J. A.; Jin, H.; Dovgaliuk, I.; Berger, R. F.; Braechevelt, T.; Yuan, H.; Martin, C.; Solano, E.; Lejaeghere, K.; Rogge, S. M. J. Thermal Unequilibrium of Strained Black CsPbI_3 Thin Films. *Science*. **2019**, *365* (6454), 679–684.
- (26) Stoumpos, C. C.; Malliakas, C. D.; Kanatzidis, M. G. Semiconducting Tin and Lead Iodide Perovskites with Organic Cations: Phase Transitions, High Mobilities, and near-Infrared Photoluminescent Properties. *Inorg. Chem.* **2013**, *52* (15), 9019–9038.
- (27) Luo, B.; Li, F.; Xu, K.; Guo, Y.; Liu, Y.; Xia, Z.; Zhang, J. Z. B-Site Doped Lead Halide Perovskites: Synthesis, Band Engineering, Photophysics, and Light Emission Applications. *J. Mater. Chem. C* **2019**, *7* (10), 2781–2808.
- (28) Li, C.; Lu, X.; Ding, W.; Feng, L.; Gao, Y.; Guo, Z. Formability of ABX_3 (X = F, Cl, Br, I) Halide Perovskites. *Acta Crystallogr. Sect. B Struct. Sci.* **2008**, *64* (6), 702–707.
- (29) Berry, J.; Buonassisi, T.; Egger, D. A.; Hodes, G.; Kronik, L.; Loo, Y.; Lubomirsky, I.; Marder, S. R.; Mastai, Y.; Miller, J. S. Hybrid Organic–Inorganic Perovskites (HOIPs): Opportunities and Challenges. *Adv. Mater.* **2015**, *27* (35), 5102–5112.
- (30) Wei, H.; Fang, Y.; Mulligan, P.; Chuirazzi, W.; Fang, H.-H.; Wang, C.; Ecker, B. R.; Gao, Y.; Loi, M. A.; Cao, L. Sensitive X-Ray Detectors Made of Methylammonium Lead Tribromide Perovskite Single Crystals. *Nat. Photonics*

- 2016, *10* (5), 333–339.
- (31) Cho, H.; Jeong, S.-H.; Park, M.-H.; Kim, Y.-H.; Wolf, C.; Lee, C.-L.; Heo, J. H.; Sadhanala, A.; Myoung, N.; Yoo, S. Overcoming the Electroluminescence Efficiency Limitations of Perovskite Light-Emitting Diodes. *Science* **2015**, *350* (6265), 1222–1225.
- (32) Xing, G.; Mathews, N.; Lim, S. S.; Yantara, N.; Liu, X.; Sabba, D.; Grätzel, M.; Mhaisalkar, S.; Sum, T. C. Low-Temperature Solution-Processed Wavelength-Tunable Perovskites for Lasing. *Nat. Mater.* **2014**, *13* (5), 476–480.
- (33) Iftikhar, F. J.; Wali, Q.; Yang, S.; Iqbal, Y.; Jose, R.; Munir, S.; Gondal, I. A.; Khan, M. E. Structural and Optoelectronic Properties of Hybrid Halide Perovskites for Solar Cells. *Org. Electron.* **2021**, *91*, 106077.
- (34) De Wolf, S.; Holovsky, J.; Moon, S.-J.; Loper, P.; Niesen, B.; Ledinsky, M.; Haug, F. J.; Yum, J. H.; Ballif, C. Organometallic Halide Perovskites: Sharp Optical Absorption Edge and its Relation to Photovoltaic Performance. *J. Phys. Chem. Lett.* **2014**, *5* (6), 1035–1039.
- (35) Yin, W. J.; Shi, T.; Yan, Y. Unusual Defect Physics in CH₃NH₃PbI₃ Perovskite Solar Cell Absorber. *Appl. Phys. Lett.* **2014**, *104* (6), 63903.
- (36) Vak, D.; Hwang, K.; Faulks, A.; Jung, Y.; Clark, N.; Kim, D.; Wilson, G. J.; Watkins, S. E. 3D Printer Based Slot-die Coater as a Lab-to-fab Translation Tool for Solution-processed Solar Cells. *Adv. Energy Mater.* **2015**, *5* (4), 1401539.
- (37) Dualeh, A.; Tétreault, N.; Moehl, T.; Gao, P.; Nazeeruddin, M. K.; Grätzel, M. Effect of Annealing Temperature on Film Morphology of Organic–Inorganic Hybrid Perovskite Solid-state Solar Cells. *Adv. Funct. Mater.* **2014**, *24* (21), 3250–3258.
- (38) Bera, A. M.; Wargulski, D. R.; Unold, T. High Efficient Perovskite Solar Cell Material CH₃NH₃PbI₃: Synthesis of Films and Their Characterization. In *AIP Conference Proceedings*; AIP Publishing LLC, **2018**, 1942, 140038.
- (39) Pang, S.; Hu, H.; Zhang, J.; Lv, S.; Yu, Y.; Wei, F.; Qin, T.; Xu, H.; Liu, Z.; Cui, G. NH₂CHNH₂PbI₃: An Alternative Organolead Iodide Perovskite Sensitizer for Mesoscopic Solar Cells. *Chem. Mater.* **2014**, *26* (3), 1485–1491.
- (40) Liu, M.; Johnston, M. B.; Snaith, H. J. Efficient Planar Heterojunction Perovskite Solar Cells by Vapour Deposition. *Nature* **2013**, *501* (7467), 395–398.
- (41) Chen, Q.; Zhou, H.; Hong, Z.; Luo, S.; Duan, H. S.; Wang, H. H.; Liu, Y.; Li, G.; Yang, Y. Planar Heterojunction Perovskite Solar Cells via Vapor-Assisted Solution Process. *J. Am. Chem. Soc.* **2014**, *136* (2), 622–625.
- (42) Hou, C. H.; Nie, W. Perovskite Thin Film Growth Techniques. In *Metal-Halide Perovskite Semiconductors: From Physical Properties to Opto-electronic Devices and X-ray Sensors*. Springer, **2023**, 17–25.
- (43) Grätzel, M. Solar Energy Conversion by Dye-Sensitized Photovoltaic Cells. *Inorg. Chem.* **2005**, *44* (20), 6841–6851.
- (44) Salim, T.; Sun, S.; Abe, Y.; Krishna, A.; Grimsdale, A. C.; Lam, Y. M. Perovskite-Based Solar Cells: Impact of Morphology and Device Architecture on Device Performance. *J. Mater. Chem. A* **2015**, *3* (17), 8943–8969.

- (45) Xing, G.; Mathews, N.; Sun, S.; Lim, S. S.; Lam, Y. M.; Grätzel, M.; Mhaisalkar, S.; Sum, T. C. Long-Range Balanced Electron-and Hole-Transport Lengths in Organic-Inorganic $\text{CH}_3\text{NH}_3\text{PbI}_3$. *Science* **2013**, *342* (6156), 344–347.
- (46) Eperon, G. E.; Burlakov, V. M.; Docampo, P.; Goriely, A.; Snaith, H. J. Morphological Control for High Performance, Solution-processed Planar Heterojunction Perovskite Solar Cells. *Adv. Funct. Mater.* **2014**, *24* (1), 151–157.
- (47) Chu, Z.; Yang, M.; Schulz, P.; Wu, D.; Ma, X.; Seifert, E.; Sun, L.; Li, X.; Zhu, K.; Lai, K. Impact of Grain Boundaries on Efficiency and Stability of Organic-Inorganic Trihalide Perovskites. *Nat. Commun.* **2017**, *8* (1), 2230.
- (48) Nie, W.; Tsai, H.; Asadpour, R.; Blancon, J.-C.; Neukirch, A. J.; Gupta, G.; Crochet, J. J.; Chhowalla, M.; Tretiak, S.; Alam, M. A. High-Efficiency Solution-Processed Perovskite Solar Cells with Millimeter-Scale Grains. *Science* **2015**, *347* (6221), 522–525.
- (49) Bi, C.; Yuan, Y.; Fang, Y.; Huang, J. Low-temperature Fabrication of Efficient Wide-bandgap Organolead Trihalide Perovskite Solar Cells. *Adv. Energy Mater.* **2015**, *5* (6), 1401616.
- (50) Shao, Y.; Xiao, Z.; Bi, C.; Yuan, Y.; Huang, J. Origin and Elimination of Photocurrent Hysteresis by Fullerene Passivation in $\text{CH}_3\text{NH}_3\text{PbI}_3$ Planar Heterojunction Solar Cells. *Nat. Commun.* **2014**, *5* (1), 5784.
- (51) Liu, T.; Chen, K.; Hu, Q.; Zhu, R.; Gong, Q. Inverted Perovskite Solar Cells: Progresses and Perspectives. *Adv. Energy Mater.* **2016**, *6* (17), 1600457.
- (52) Guo, Y.; Lei, H.; Xiong, L.; Li, B.; Fang, G. An Integrated Organic–Inorganic Hole Transport Layer for Efficient and Stable Perovskite Solar Cells. *J. Mater. Chem. A* **2018**, *6* (5), 2157–2165.
- (53) Huang, L.; Sun, X.; Li, C.; Xu, J.; Xu, R.; Du, Y.; Ni, J.; Cai, H.; Li, J.; Hu, Z. UV-Sintered Low-Temperature Solution-Processed SnO_2 as Robust Electron Transport Layer for Efficient Planar Heterojunction Perovskite Solar Cells. *ACS Appl. Mater. Interfaces* **2017**, *9* (26), 21909–21920.
- (54) Tseng, Z. L.; Chiang, C. H.; Wu, C. G. Surface Engineering of ZnO Thin Film for High Efficiency Planar Perovskite Solar Cells. *Sci. Rep.* **2015**, *5* (1), 13211.
- (55) Wang, L.; Fu, W.; Gu, Z.; Fan, C.; Yang, X.; Li, H.; Chen, H. Low Temperature Solution Processed Planar Heterojunction Perovskite Solar Cells with a CdSe Nanocrystal as an Electron Transport/Extraction Layer. *J. Mater. Chem. C* **2014**, *2* (43), 9087–9090.
- (56) Singh, R.; Giri, A.; Pal, M.; Thiyagarajan, K.; Kwak, J.; Lee, J. J.; Jeong, U.; Cho, K. Perovskite Solar Cells with an MoS_2 Electron Transport Layer. *J. Mater. Chem. A* **2019**, *7* (12), 7151–7158.
- (57) Gheno, A.; Pham, T. T. T.; Di Bin, C.; Bouclé, J.; Ratier, B.; Vedraïne, S. Printable WO_3 Electron Transporting Layer for Perovskite Solar Cells: Influence on Device Performance and Stability. *Sol. Energy Mater. Sol. Cells* **2017**, *161*, 347–354.
- (58) Priyadarshi, A.; Bashir, A.; Gunawan, J. T.; Haur, L. J.; Bruno, A.; Akhter, Z.; Mathews, N.; Mhaisalkar, S. G. Simplified Architecture of a Fully Printable

- Perovskite Solar Cell Using a Thick Zirconia Layer. *Energy Technol.* **2017**, *5* (10), 1866–1872.
- (59) Hou, Q.; Ren, J.; Chen, H.; Yang, P.; Shao, Q.; Zhao, M.; Zhao, X.; He, H.; Wang, N.; Luo, Q. Synergistic Hematite-fullerene Electron-extracting Layers for Improved Efficiency and Stability in Perovskite Solar Cells. *ChemElectroChem* **2018**, *5* (5), 726–731.
- (60) Kim, H. S.; Lee, C. R.; Im, J. H.; Lee, K. B.; Moehl, T.; Marchioro, A.; Moon, S.-J.; Humphry-Baker, R.; Yum, J.-H.; Moser, J. E. Lead Iodide Perovskite Sensitized All-Solid-State Submicron Thin Film Mesoscopic Solar Cell with Efficiency Exceeding 9%. *Sci. Rep.* **2012**, *2* (1), 1–7.
- (61) Di Giacomo, F.; Razza, S.; Matteocci, F.; D’Epifanio, A.; Licoccia, S.; Brown, T. M.; Di Carlo, A. High Efficiency $\text{CH}_3\text{NH}_3\text{PbI}_{(3-x)}\text{Cl}_x$ Perovskite Solar Cells with Poly (3-Hexylthiophene) Hole Transport Layer. *J. Power Sources* **2014**, *251*, 152–156.
- (62) Jung, M.; Kim, Y. C.; Jeon, N. J.; Yang, W. S.; Seo, J.; Noh, J. H.; Il Seok, S. Thermal Stability of CuSCN Hole Conductor-based Perovskite Solar Cells. *ChemSusChem* **2016**, *9* (18), 2592–2596.
- (63) Shalan, A. E.; Oshikiri, T.; Narra, S.; Elshanawany, M. M.; Ueno, K.; Wu, H. P.; Nakamura, K.; Shi, X.; Diao, E. W. G.; Misawa, H. Cobalt Oxide (CoO_x) as an Efficient Hole-Extracting Layer for High-Performance Inverted Planar Perovskite Solar Cells. *ACS Appl. Mater. Interfaces* **2016**, *8* (49), 33592–33600.
- (64) Hu, L.; Li, M.; Yang, K.; Xiong, Z.; Yang, B.; Wang, M.; Tang, X.; Zang, Z.; Liu, X.; Li, B. PEDOT: PSS Monolayers to Enhance the Hole Extraction and Stability of Perovskite Solar Cells. *J. Mater. Chem. A* **2018**, *6* (34), 16583–16589.
- (65) Xie, F.; Chen, C. C.; Wu, Y.; Li, X.; Cai, M.; Liu, X.; Yang, X.; Han, L. Vertical Recrystallization for Highly Efficient and Stable Formamidinium-Based Inverted-Structure Perovskite Solar Cells. *Energy Environ. Sci.* **2017**, *10* (9), 1942–1949.
- (66) Huang, A.; Lei, L.; Zhu, J.; Yu, Y.; Liu, Y.; Yang, S.; Bao, S.; Cao, X.; Jin, P. Fast Fabrication of a Stable Perovskite Solar Cell with an Ultrathin Effective Novel Inorganic Hole Transport Layer. *Langmuir* **2017**, *33* (15), 3624–3634.
- (67) Zhao, Q.; Wu, R.; Zhang, Z.; Xiong, J.; He, Z.; Fan, B.; Dai, Z.; Yang, B.; Xue, X.; Cai, P. Achieving Efficient Inverted Planar Perovskite Solar Cells with Nondoped PTAA as a Hole Transport Layer. *Org. Electron.* **2019**, *71*, 106–112.
- (68) You, J.; Hong, Z.; Yang, Y.; Chen, Q.; Cai, M.; Song, T. B.; Chen, C. C.; Lu, S.; Liu, Y.; Zhou, H. Low-Temperature Solution-Processed Perovskite Solar Cells with High Efficiency and Flexibility. *ACS Nano* **2014**, *8* (2), 1674–1680.
- (69) Sun, W.; Li, Y.; Ye, S.; Rao, H.; Yan, W.; Peng, H.; Li, Y.; Liu, Z.; Wang, S.; Chen, Z. High-Performance Inverted Planar Heterojunction Perovskite Solar Cells Based on a Solution-Processed CuOx Hole Transport Layer. *Nanoscale* **2016**, *8* (20), 10806–10813.
- (70) Ponseca Jr, C. S.; Savenije, T. J.; Abdellah, M.; Zheng, K.; Yartsev, A.; Pascher, T.; Harlang, T.; Chabera, P.; Pullerits, T.; Stepanov, A. Organometal Halide Perovskite Solar Cell Materials Rationalized: Ultrafast Charge Generation, High

- and Microsecond-Long Balanced Mobilities, and Slow Recombination. *J. Am. Chem. Soc.* **2014**, *136* (14), 5189–5192.
- (71) Stranks, S. D.; Eperon, G. E.; Grancini, G.; Menelaou, C.; Alcocer, M. J. P.; Leijtens, T.; Herz, L. M.; Petrozza, A.; Snaith, H. J. Electron-Hole Diffusion Lengths Exceeding 1 Micrometer in an Organometal Trihalide Perovskite Absorber. *Science* **2013**, *342* (6156), 341–344.
- (72) Shi, J.; Li, Y.; Li, Y.; Li, D.; Luo, Y.; Wu, H.; Meng, Q. From Ultrafast to Ultraslow: Charge-Carrier Dynamics of Perovskite Solar Cells. *Joule* **2018**, *2* (5), 879–901.
- (73) Shah, J. Phonon Dynamics. Ultrafast Spectroscopy of Semiconductors and Semiconductor Nanostructures; *Springer*, **1999**, 193–224.
- (74) Rossi, F.; Kuhn, T. Theory of Ultrafast Phenomena in Photoexcited Semiconductors. *Rev. Mod. Phys.* **2002**, *74* (3), 895.
- (75) Singh, J. Excitation Energy Transfer Processes in Condensed Matter: Theory and Applications. *Springer Science & Business Media*, **2013**.
- (76) Hegedus, S.; Luque, A. Handbook of Photovoltaic Science and Engineering; *John Wiley & Sons*, **2011**.
- (77) Sze, S. M.; Ng, K. K. Pn Junctions. *Phys. Semicond. Devices* **2006**, *2*, 80–89.
- (78) Dong, Q.; Fang, Y.; Shao, Y.; Mulligan, P.; Qiu, J.; Cao, L.; Huang, J. Electron-Hole Diffusion Lengths >175 nm in Solution-Grown CH₃NH₃PbI₃ Single Crystals. *Science* **2015**, *347* (6225), 967–970.
- (79) Brenner, T. M.; Egger, D. A.; Kronik, L.; Hodes, G.; Cahen, D. Hybrid Organic—Inorganic Perovskites: Low-Cost Semiconductors with Intriguing Charge-Transport Properties. *Nat. Rev. Mater.* **2016**, *1* (1), 1–16.
- (80) Herz, L. M. Charge-Carrier Dynamics in Organic-Inorganic Metal Halide Perovskites. *Annu. Rev. Phys. Chem.* **2016**, *67*, 65–89.
- (81) Tress, W.; Marinova, N.; Inganäs, O.; Nazeeruddin, M. K.; Zakeeruddin, S. M.; Graetzel, M. Predicting the Open-circuit Voltage of CH₃NH₃PbI₃ Perovskite Solar Cells Using Electroluminescence and Photovoltaic Quantum Efficiency Spectra: The Role of Radiative and Non-radiative Recombination. *Adv. Energy Mater.* **2015**, *5* (3), 1400812.
- (82) Seif, J. P. Window Layers for Silicon Heterojunction Solar Cells, *EPFL* **2015**.
- (83) Bernede, J. C. Organic Photovoltaic Cells: History, Principle and Techniques. *J. Chil. Chem. Soc.* **2008**, *53* (3), 1549–1564.
- (84) Nelson, J. A. The Physics of Solar Cells. *World Scientific Publishing Company*, **2003**.
- (85) Kojima, A.; Teshima, K.; Shirai, Y.; Miyasaka, T. Organometal Halide Perovskites as Visible-Light Sensitizers for Photovoltaic Cells. *J. Am. Chem. Soc.* **2009**, *131* (17), 6050–6051.
- (86) Grätzel, M. The Light and Shade of Perovskite Solar Cells. *Nat. Mater.* **2014**, *13* (9), 838–842.
- (87) Brunetti, B.; Cavallo, C.; Ciccioli, A.; Gigli, G.; Latini, A. On the Thermal and Thermodynamic (in) Stability of Methylammonium Lead Halide Perovskites.

- Sci. Rep.* **2016**, *6* (1), 1–10.
- (88) Kulbak, M.; Cahen, D.; Hodes, G. How Important Is the Organic Part of Lead Halide Perovskite Photovoltaic Cells? Efficient CsPbBr₃ Cells. *J. Phys. Chem. Lett.* **2015**, *6* (13), 2452–2456.
- (89) Hu, Y.; Aygüler, M. F.; Petrus, M. L.; Bein, T.; Docampo, P. Impact of Rubidium and Cesium Cations on the Moisture Stability of Multiple-Cation Mixed-Halide Perovskites. *ACS Energy Lett.* **2017**, *2* (10), 2212–2218.
- (90) Stoumpos, C.C.; Malliakas, C.D.; Peters, J.A.; Liu, Z.; Sebastian, M.; Im, J.; Chasapis, T.C.; Wibowo, A.C.; Chung, D.Y.; Freeman, A.J.; Wessels, B.W. Crystal Growth of the Perovskite Semiconductor CsPbBr₃: a New Material for High-Energy Radiation Detection. *Cryst. Growth Des.* **2013**, *13*, 2722–2727 .
- (91) Choi, H.; Jeong, J.; Kim, H. B.; Kim, S.; Walker, B.; Kim, G. H.; Kim, J. Y. Cesium-Doped Methylammonium Lead Iodide Perovskite Light Absorber for Hybrid Solar Cells. *Nano Energy* **2014**, *7*, 80–85.
- (92) Lai, M.; Kong, Q.; Bischak, C. G.; Yu, Y.; Dou, L.; Eaton, S. W.; Ginsberg, N. S.; Yang, P. Structural, Optical, and Electrical Properties of Phase-Controlled Cesium Lead Iodide Nanowires. *Nano Res.* **2017**, *10* (4), 1107–1114.
- (93) Eperon, G. E.; Paternò, G. M.; Sutton, R. J.; Zampetti, A.; Haghighirad, A. A.; Cacialli, F.; Snaith, H. J. Inorganic Caesium Lead Iodide Perovskite Solar Cells. *J. Mater. Chem. A* **2015**, *3* (39), 19688–19695.
- (94) Hu, Y.; Bai, F.; Liu, X.; Ji, Q.; Miao, X.; Qiu, T.; Zhang, S. Bismuth Incorporation Stabilized A-CsPbI₃ for Fully Inorganic Perovskite Solar Cells. *ACS Energy Lett.* **2017**, *2*(10), 2219–2227.
- (95) Voloshinovskii, A.; Myagkota, S.; Levitskii, R. Luminescence of Ferroelastic CsPbCl₃ Nanocrystals. *Ferroelectrics* **2005**, *317* (1), 119–123.
- (96) Dastidar, S.; Egger, D. A.; Tan, L. Z.; Cromer, S. B.; Dillon, A. D.; Liu, S.; Kronik, L.; Rappe, A. M.; Fafarman, A. T. High Chloride Doping Levels Stabilize the Perovskite Phase of Cesium Lead Iodide. *Nano Lett.* **2016**, *16* (6), 3563–3570.
- (97) Protesescu, L.; Yakunin, S.; Bodnarchuk, M. I.; Krieg, F.; Caputo, R.; Hendon, C. H.; Yang, R. X.; Walsh, A.; Kovalenko, M. V. Nanocrystals of Cesium Lead Halide Perovskites (CsPbX₃, X= Cl, Br, and I): Novel Optoelectronic Materials Showing Bright Emission with Wide Color Gamut. *Nano Lett.* **2015**, *15* (6), 3692–3696.
- (98) Kulbak, M.; Gupta, S.; Kedem, N.; Levine, I.; Bendikov, T.; Hodes, G.; Cahen, D. Cesium Enhances Long-Term Stability of Lead Bromide Perovskite-Based Solar Cells. *J. Phys. Chem. Lett.* **2016**, *7* (1), 167–172.
- (99) Lau, C. F. J.; Deng, X.; Ma, Q.; Zheng, J.; Yun, J. S.; Green, M. A.; Huang, S.; Ho-Baillie, A. W. Y. CsPbIBr₂ Perovskite Solar Cell by Spray-Assisted Deposition. *ACS Energy Lett.* **2016**, *1* (3), 573–577.
- (100) Sutton, R. J.; Eperon, G. E.; Miranda, L.; Parrott, E. S.; Kamino, B.A.; Patel, J.B.; Snaith, H.J. Bandgap-Tunable Cesium Lead Halide Perovskites with high Thermal Stability for Efficient Solar Cells. *Adv. Energy Mater* **2016**, *6*, 1–6.
- (101) Kennedy, C. L.; Hill, A. H.; Massaro, E. S.; Grumstrup, E. M. Ultrafast Excited-

- State Transport and Decay Dynamics in Cesium Lead Mixed Halide Perovskites. *ACS Energy Lett.* **2017**, *2* (7), 1501–1506.
- (102) Nam, J. K.; Jung, M. S.; Chai, S. U.; Choi, Y. J.; Kim, D.; Park, J. H. Unveiling the Crystal Formation of Cesium Lead Mixed-Halide Perovskites for Efficient and Stable Solar Cells. *J. Phys. Chem. Lett.* **2017**, *8* (13), 2936–2940.
- (103) Bremner, S. P.; Levy, M. Y.; Honsberg, C. B. Analysis of Tandem Solar Cell Efficiencies under AM1.5G Spectrum Using a Rapid Flux Calculation Method. *Photovol: Res; Appl*, **2008**, *16*(3), 225-233.
- (104) Niezgoda, J. S.; Foley, B. J.; Chen, A. Z.; Choi, J. J. Improved Charge Collection in Highly Efficient CsPbBr₂ Solar Cells with Light-Induced Dealloying. *ACS Energy Lett.* **2017**, *2* (5), 1043–1049.
- (105) Berdiyrov, G. R.; Kachmar, A.; El-Mellouhi, F.; Carignano, M. A.; El-Amine Madjet, M. Role of Cations on the Electronic Transport and Optical Properties of Lead-Iodide Perovskites. *J. Phys. Chem. C* **2016**, *120* (30), 16259–16270.
- (106) Sutton, R. J.; Eperon, G. E.; Miranda, L.; Parrott, E. S.; Kamino, B. A.; Patel, J. B.; Hörantner, M. T.; Johnston, M. B.; Haghighirad, A. A.; Moore, D. T. Bandgap-tunable Cesium Lead Halide Perovskites with High Thermal Stability for Efficient Solar Cells. *Adv. Energy Mater.* **2016**, *6* (8), 1502458.
- (107) Yang, Z.; Surrente, A.; Galkowski, K.; Miyata, A.; Portugall, O.; Sutton, R. J.; Haghighirad, A. A.; Snaith, H. J.; Maude, D. K.; Plochocka, P. Impact of the Halide Cage on the Electronic Properties of Fully Inorganic Cesium Lead Halide Perovskites. *ACS Energy Lett.* **2017**, *2* (7), 1621–1627.
- (108) Yang, Z.; Surrente, A.; Galkowski, K.; Bruyant, N.; Maude, D. K.; Haghighirad, A. A.; Snaith, H. J.; Plochocka, P.; Nicholas, R. J. Unraveling the Exciton Binding Energy and the Dielectric Constant in Single-Crystal Methylammonium Lead Triiodide Perovskite. *J. Phys. Chem. Lett.* **2017**, *8* (8), 1851–1855.
- (109) Lau, C. F. J.; Zhang, M.; Deng, X.; Zheng, J.; Bing, J.; Ma, Q.; Kim, J.; Hu, L.; Green, M. A.; Huang, S. Strontium-Doped Low-Temperature-Processed CsPbI₂Br Perovskite Solar Cells. *ACS Energy Lett.* **2017**, *2* (10), 2319–2325.
- (110) Shang, M. H.; Zhang, J.; Zhang, P.; Yang, Z.; Zheng, J.; Haque, M. A.; Yang, W.; Wei, S. H.; Wu, T. Stable Bandgap-Tunable Hybrid Perovskites with Alloyed Pb–Ba Cations for High-Performance Photovoltaic Applications. *J. Phys. Chem. Lett.* **2018**, *10* (1), 59–66.
- (111) Kubicki, D. J.; Prochowicz, D.; Hofstetter, A.; Zakeeruddin, S. M.; Grätzel, M.; Emsley, L. Phase Segregation in Cs-, Rb- and K-Doped Mixed-Cation (MA)_x(FA)_{1-x}PbI₃ Hybrid Perovskites from Solid-State NMR. *J. Am. Chem. Soc.* **2017**, *139* (40), 14173–14180.
- (112) Liang, J.; Zhao, P.; Wang, C.; Wang, Y.; Hu, Y.; Zhu, G.; Ma, L.; Liu, J.; Jin, Z. CsPb_{0.9}Sn_{0.1}IBr₂ Based All-Inorganic Perovskite Solar Cells with Exceptional Efficiency and Stability. *J. Am. Chem. Soc.* **2017**, *139* (40), 14009–14012.
- (113) Yi, C.; Luo, J.; Meloni, S.; Boziki, A.; Ashari-Astani, N.; Grätzel, C.; Zakeeruddin, S. M.; Rötthlisberger, U.; Grätzel, M. Entropic Stabilization of Mixed A-Cation ABX₃ Metal Halide Perovskites for High Performance Perovskite Solar Cells. *Energy Environ. Sci.* **2016**, *9* (2), 656–662.

- (114) Saliba, M.; Matsui, T.; Seo, J. Y.; Domanski, K.; Correa-Baena, J. P.; Nazeeruddin, M. K.; Zakeeruddin, S. M.; Tress, W.; Abate, A.; Hagfeldt, A. Cesium-Containing Triple Cation Perovskite Solar Cells: Improved Stability, Reproducibility and High Efficiency. *Energy Environ. Sci.* **2016**, *9* (6), 1989–1997.
- (115) Swarnkar, A.; Mir, W. J.; Nag, A. Can B-Site Doping or Alloying Improve Thermal-and Phase-Stability of All-Inorganic CsPbX₃ (X= Cl, Br, I) Perovskites? *ACS Energy Lett.* **2018**, *3* (2), 286–289.
- (116) Yang, F.; Hirotani, D.; Kapil, G.; Kamarudin, M. A.; Ng, C. H.; Zhang, Y.; Shen, Q.; Hayase, S. All-Inorganic CsPb_{1-x}GexI₂Br Perovskite with Enhanced Phase Stability and Photovoltaic Performance. *Angew. Chemie* **2018**, *130* (39), 12927–12931.
- (117) Xiang, W.; Wang, Z.; Kubicki, D. J.; Tress, W.; Luo, J.; Prochowicz, D.; Akin, S.; Emsley, L.; Zhou, J.; Dietler, G. Europium-Doped CsPbI₂Br for Stable and Highly Efficient Inorganic Perovskite Solar Cells. *Joule* **2019**, *3* (1), 205–214.
- (118) Sanchez, S.; Christoph, N.; Grobety, B.; Phung, N.; Steiner, U.; Saliba, M.; Abate, A. Efficient and Stable Inorganic Perovskite Solar Cells Manufactured by Pulsed Flash Infrared Annealing. *Adv. Energy Mater.* **2018**, *8* (30), 1802060.
- (119) Fu, L.; Zhang, Y.; Chang, B.; Li, B.; Zhou, S.; Zhang, L.; Yin, L. A Fluorine-Modulated Bulk-Phase Heterojunction and Tolerance Factor for Enhanced Performance and Structure Stability of Cesium Lead Halide Perovskite Solar Cells. *J. Mater. Chem. A* **2018**, *6* (27), 13263–13270.
- (120) Subhani, W. S.; Wang, K.; Du, M.; Liu, S. F. Goldschmidt-Rule-Deviated Perovskite CsPbIBr₂ by Barium Substitution for Efficient Solar Cells. *Nano energy* **2019**, *61*, 165–172.
- (121) Slotcavage, D. J.; Karunadasa, H. I.; McGehee, M. D. Light-Induced Phase Segregation in Halide-Perovskite Absorbers. *ACS Energy Lett.* **2016**, *1* (6), 1199–1205.
- (122) DeQuilettes, D. W.; Zhang, W.; Burlakov, V. M.; Graham, D. J.; Leijtens, T.; Osherov, A.; Bulović, V.; Snaith, H. J.; Ginger, D. S.; Stranks, S. D. Photo-Induced Halide Redistribution in Organic–Inorganic Perovskite Films. *Nat. Commun.* **2016**, *7* (1), 11683.
- (123) Beal, R. E.; Slotcavage, D. J.; Leijtens, T.; Bowring, A. R.; Belisle, R. A.; Nguyen, W. H.; Burkhard, G. F.; Hoke, E. T.; McGehee, M. D. Cesium Lead Halide Perovskites with Improved Stability for Tandem Solar Cells. *J. Phys. Chem. Lett.* **2016**, *7* (5), 746–751.
- (124) Zhou, W.; Zhao, Y.; Zhou, X.; Fu, R.; Li, Q.; Zhao, Y.; Liu, K.; Yu, D.; Zhao, Q. Light-Independent Ionic Transport in Inorganic Perovskite and Ultrastable Cs-Based Perovskite Solar Cells. *J. Phys. Chem. Lett.* **2017**, *8* (17), 4122–4128.
- (125) Bischak, C. G.; Hetherington, C. L.; Wu, H.; Aloni, S.; Ogletree, D. F.; Limmer, D. T.; Ginsberg, N. S. Origin of Reversible Photoinduced Phase Separation in Hybrid Perovskites. *Nano Lett.* **2017**, *17* (2), 1028–1033.
- (126) McMeekin, D. P.; Sadoughi, G.; Rehman, W.; Eperon, G. E.; Saliba, M.; Hörantner, M. T.; Haghighirad, A.; Sakai, N.; Korte, L.; Rech, B. A Mixed-Cation Lead Mixed-Halide Perovskite Absorber for Tandem Solar Cells. *Science*

- 2016**, 351 (6269), 151–155.
- (127) Juarez-Perez, E. J.; Sanchez, R. S.; Badia, L.; Garcia-Belmonte, G.; Kang, Y. S.; Mora-Sero, I.; Bisquert, J. Photoinduced Giant Dielectric Constant in Lead Halide Perovskite Solar Cells. *J. Phys. Chem. Lett.* **2014**, 5 (13), 2390–2394.
- (128) Zhao, Y.; Wei, J.; Li, H.; Yan, Y.; Zhou, W.; Yu, D.; Zhao, Q. A Polymer Scaffold for Self-Healing Perovskite Solar Cells. *Nat. Commun.* **2016**, 7 (1), 10228.
- (129) Zhao, Y. C.; Zhou, W. K.; Zhou, X.; Liu, K. H.; Yu, D. P.; Zhao, Q. Quantification of Light-Enhanced Ionic Transport in Lead Iodide Perovskite Thin Films and Its Solar Cell Applications. *Light Sci. Appl.* **2017**, 6 (5), e16243–e16243.
- (130) Li, W.; Rothmann, M. U.; Liu, A.; Wang, Z.; Zhang, Y.; Pascoe, A. R.; Lu, J.; Jiang, L.; Chen, Y.; Huang, F. Phase Segregation Enhanced Ion Movement in Efficient Inorganic CsPbI₂Br₂ Solar Cells. *Adv. Energy Mater.* **2017**, 7(20), 1700946.
- (131) Wang, X.; Ling, Y.; Lian, X.; Xin, Y.; Dhungana, K. B.; Perez-Orive, F.; Knox, J.; Chen, Z.; Zhou, Y.; Beery, D. Suppressed Phase Separation of Mixed-Halide Perovskites Confined in Endotaxial Matrices. *Nat. Commun.* **2019**, 10 (1), 695.
- (132) Zhu, H.; Miyata, K.; Fu, Y.; Wang, J.; Joshi, P. P.; Niesner, D.; Williams, K. W.; Jin, S.; Zhu, X. Y. Screening in Crystalline Liquids Protects Energetic Carriers in Hybrid Perovskites. *Science* **2016**, 353 (6306), 1409–1413.
- (133) Mariotti, S.; Hutter, O. S.; Phillips, L. J.; Yates, P. J.; Kundu, B.; Durose, K. Stability and Performance of CsPbI₂Br Thin Films and Solar Cell Devices. *ACS Appl. Mater. Interfaces* **2018**, 10 (4), 3750–3760.
- (134) Yang, J.; Luo, Y.; Bao, Q.; Li, Y.; Tang, J. Recent Advances in Energetics and Stability of Metal Halide Perovskites for Optoelectronic Applications. *Adv. Mater. Interfaces* **2019**, 6 (3), 1801351.
- (135) Xue, Q.; Bai, Y.; Liu, M.; Xia, R.; Hu, Z.; Chen, Z.; Jiang, X.; Huang, F.; Yang, S.; Matsuo, Y. Dual Interfacial Modifications Enable High Performance Semitransparent Perovskite Solar Cells with Large Open Circuit Voltage and Fill Factor. *Adv. Energy Mater.* **2017**, 7 (9), 1602333.
- (136) Ryu, S.; Noh, J. H.; Jeon, N. J.; Kim, Y. C.; Yang, W. S.; Seo, J.; Seok, S. II. Voltage Output of Efficient Perovskite Solar Cells with High Open-Circuit Voltage and Fill Factor. *Energy Environ. Sci.* **2014**, 7 (8), 2614–2618.
- (137) Li, H.; Tong, G.; Chen, T.; Zhu, H.; Li, G.; Chang, Y.; Wang, L.; Jiang, Y. Interface Engineering Using a Perovskite Derivative Phase for Efficient and Stable CsPbBr₃ Solar Cells. *J. Mater. Chem. A* **2018**, 6 (29), 14255–14261.
- (138) Zhang, J.; Jin, Z.; Liang, L.; Wang, H.; Bai, D.; Bian, H.; Wang, K.; Wang, Q.; Yuan, N.; Ding, J. Iodine-optimized Interface for Inorganic CsPbI₂Br Perovskite Solar Cell to Attain High Stabilized Efficiency Exceeding 14%. *Adv. Sci.* **2018**, 5 (12), 1801123.
- (139) Yan, L.; Xue, Q.; Liu, M.; Zhu, Z.; Tian, J.; Li, Z.; Chen, Z.; Chen, Z.; Yan, H.; Yip, H. Interface Engineering for All-inorganic CsPbI₂Br Perovskite Solar Cells with Efficiency over 14%. *Adv. Mater.* **2018**, 30 (33), 1802509.

- (140) Lin, J.; Lai, M.; Dou, L.; Kley, C. S.; Chen, H.; Peng, F.; Sun, J.; Lu, D.; Hawks, S. A.; Xie, C. Thermochromic Halide Perovskite Solar Cells. *Nat. Mater.* **2018**, *17* (3), 261–267.
- (141) Li, B.; Zhang, Y.; Fu, L.; Yu, T.; Zhou, S.; Zhang, L.; Yin, L. Surface Passivation Engineering Strategy to Fully-Inorganic Cubic CsPbI₃ Perovskites for High-Performance Solar Cells. *Nat. Commun.* **2018**, *9* (1), 1–8.
- (142) Yuan, J.; Zhang, L.; Bi, C.; Wang, M.; Tian, J. Surface Trap States Passivation for High-performance Inorganic Perovskite Solar Cells. *Sol. Rrl* **2018**, *2* (10), 1800188.
- (143) Wang, Y.; Dar, M. I.; Ono, L. K.; Zhang, T.; Kan, M.; Li, Y.; Zhang, L.; Wang, X.; Yang, Y.; Gao, X. Thermodynamically Stabilized β -CsPbI₃-Based Perovskite Solar Cells with Efficiencies > 18%. *Science*. **2019**, *365* (6453), 591–595.
- (144) Halme, J.; Mäkinen, P. Theoretical Efficiency Limits of Ideal Coloured Opaque Photovoltaics. *Energy Environ. Sci.* **2019**, *12* (4), 1274–1285.
- (145) Grånäs, O.; Vinichenko, D.; Kaxiras, E. Establishing the Limits of Efficiency of Perovskite Solar Cells from First Principles Modeling. *Sci. Rep.* **2016**, *6* (1), 1–6.
- (146) Hutter, E. M.; Sutton, R. J.; Chandrashekar, S.; Abdi-Jalebi, M.; Stranks, S. D.; Snaith, H. J.; Savenije, T. J. Vapour-Deposited Cesium Lead Iodide Perovskites: Microsecond Charge Carrier Lifetimes and Enhanced Photovoltaic Performance. *ACS Energy Lett.* **2017**, *2* (8), 1901–1908.
- (147) Li, B.; Zhang, Y.; Zhang, L.; Yin, L. PbCl₂-Tuned Inorganic Cubic CsPbBr₃ (Cl) Perovskite Solar Cells with Enhanced Electron Lifetime, Diffusion Length and Photovoltaic Performance. *J. Power Sources* **2017**, *360*, 11–20.
- (148) Wang, Z. L. Nanopiezotronics. *Adv. Mater.* **2007**, *19* (6), 889–892.
- (149) Zhang, C.; Fan, W.; Wang, S.; Wang, Q.; Zhang, Y.; Dong, K. Recent Progress of Wearable Piezoelectric Nanogenerators. *ACS Appl. Electron. Mater.* **2021**, *3* (6), 2449–2467.
- (150) Fan, F. R.; Tang, W.; Wang, Z. L. Flexible Nanogenerators for Energy Harvesting and Self-powered Electronics. *Adv. Mater.* **2016**, *28* (22), 4283–4305.
- (151) Wang, Z. L.; Zhu, G.; Yang, Y.; Wang, S.; Pan, C. Progress in Nanogenerators for Portable Electronics. *Mater. today* **2012**, *15* (12), 532–543.
- (152) Xu, C.; Wang, X.; Wang, Z. L. Nanowire Structured Hybrid Cell for Concurrently Scavenging Solar and Mechanical Energies. *J. Am. Chem. Soc.* **2009**, *131* (16), 5866–5872.
- (153) Mishra, A.; Bhatt, N.; Bajpai, A. K. Nanostructured Superhydrophobic Coatings for Solar Panel Applications. In *Nanomaterials-Based Coatings*; Elsevier, 2019; pp 397–424.
- (154) Dler, A. J. Thin Film Deposition Processes. *Int. J. Mod. Phys. Appl.* **2015**, *1* (4), 193–199.
- (155) Park, S. I.; Quan, Y. J.; Kim, S. H.; Kim, H.; Kim, S.; Chun, D. M.; Lee, C. S.; Taya, M.; Chu, W. S.; Ahn, S.-H. A Review on Fabrication Processes for

- Electrochromic Devices. *Int. J. Precis. Eng. Manuf. Technol.* **2016**, *3*, 397–421.
- (156) Fatima, K.; Haider, M. I.; Fakhruddin, A.; Akhter, Z.; Sultan, M.; Schmidt-Mende, L. Performance Enhancement of CsPbI₂Br Perovskite Solar Cells via Stoichiometric Control and Interface Engineering. *Sol. Energy* **2020**, *211*, 654–660.
- (157) He, Q.; Li, X.; Zhang, J.; Zhang, H.; Briscoe, J. P–N Junction-Based ZnO Wearable Textile Nanogenerator for Biomechanical Energy Harvesting. *Nano Energy* **2021**, *85*, 105938.
- (158) Giessibl F.; Sugawara Y.; Morita S.; Hosoi H.; Sueoka K.; Mukasa K.; Sasahara A.; Onishi H. Noncontact Atomic Force Microscopy and Related Topics. Springer Handbook of Nanotechnology; Springer, **2002**.
- (159) Zimmermann, E.; Wong, K. K.; Müller, M.; Hu, H.; Ehrenreich, P.; Kohlstädt, M.; Würfel, U.; Mastroianni, S.; Mathiazhagan, G.; Hinsch, A. Characterization of Perovskite Solar Cells: Towards a Reliable Measurement Protocol. *APL Mater.* **2016**, *4* (9), 91901.
- (160) Atourki, L.; Vega, E.; Marí, B.; Mollar, M.; Ahsaine, H. A.; Bouabid, K.; Ihlal, A. MAPbI₂_{0.9-x}Br_xCl_{0.1} Hybrid Halide Perovskites: Shedding Light on the Effect of Chloride and Bromide Ions on Structural and Photoluminescence Properties. *Appl. Surf. Sci.* **2016**, *390*, 744–750.
- (161) Liu, C.; Li, W.; Zhang, C.; Ma, Y.; Fan, J.; Mai, Y. All-Inorganic CsPbI₂Br Perovskite Solar Cells with High Efficiency Exceeding 13%. *J. Am. Chem. Soc.* **2018**, *140* (11), 3825–3828.
- (162) Nawaz, A.; Erdinc, A. K.; Gultekin, B.; Tayyib, M.; Zafer, C.; Wang, K.; Akram, M. N.; Wong, K. K.; Hussain, S.; Schmidt-Mende, L. Insights into Optoelectronic Properties of Anti-Solvent Treated Perovskite Films. *J. Mater. Sci. Mater. Electron.* **2017**, *28* (20), 15630–15636.
- (163) Ma, Q.; Huang, S.; Chen, S.; Zhang, M.; Lau, C. F. J.; Lockrey, M. N.; Mulmudi, H. K.; Shan, Y.; Yao, J.; Zheng, J. The Effect of Stoichiometry on the Stability of Inorganic Cesium Lead Mixed-Halide Perovskites Solar Cells. *J. Phys. Chem. C* **2017**, *121* (36), 19642–19649.
- (164) Du, Z.; Xiang, H.; Xie, A.; Ran, R.; Zhou, W.; Wang, W.; Shao, Z. Monovalent Copper Cation Doping Enables High-Performance CsPbI₂Br₂-Based All-Inorganic Perovskite Solar Cells. *Nanomaterials* **2022**, *12* (23), 4317.
- (165) Yin, G.; Zhao, H.; Jiang, H.; Yuan, S.; Niu, T.; Zhao, K.; Liu, Z.; Liu, S. Precursor Engineering for All-inorganic CsPbI₂Br Perovskite Solar Cells with 14.78% Efficiency. *Adv. Funct. Mater.* **2018**, *28* (39), 1803269.
- (166) Islam, M. B.; Yanagida, M.; Shirai, Y.; Nabetani, Y.; Miyano, K. NiO_x Hole Transport Layer for Perovskite Solar Cells with Improved Stability and Reproducibility. *ACS omega* **2017**, *2* (5), 2291–2299.
- (167) Liu, D.; Wang, Q.; Traverse, C. J.; Yang, C.; Young, M.; Kuttipillai, P. S.; Lunt, S. Y.; Hamann, T. W.; Lunt, R. R. Impact of Ultrathin C₆₀ on Perovskite Photovoltaic Devices. *ACS Nano* **2018**, *12* (1), 876–883.
- (168) Hu, H.; Wong, K. K.; Kollek, T.; Hanusch, F.; Polarz, S.; Docampo, P.; Schmidt-Mende, L. Highly Efficient Reproducible Perovskite Solar Cells Prepared by

- Low-Temperature Processing. *Molecules* **2016**, *21* (4), 542.
- (169) Zhu, W.; Chai, W.; Zhang, Z.; Chen, D.; Chang, J.; Liu, S.; Zhang, J.; Zhang, C.; Hao, Y. Interfacial TiO₂ Atomic Layer Deposition Triggers Simultaneous Crystallization Control and Band Alignment for Efficient CsPbIBr₂ Perovskite Solar Cell. *Org. Electron.* **2019**, *74*, 103–109.
- (170) Chiba, T.; Hayashi, Y.; Ebe, H.; Hoshi, K.; Sato, J.; Sato, S.; Pu, Y.-J.; Ohisa, S.; Kido, J. Anion-Exchange Red Perovskite Quantum Dots with Ammonium Iodine Salts for Highly Efficient Light-Emitting Devices. *Nat. Photonics* **2018**, *12* (11), 681–687.
- (171) Liu, P.; Yang, X.; Chen, Y.; Xiang, H.; Wang, W.; Ran, R.; Zhou, W.; Shao, Z. Promoting the Efficiency and Stability of CsPbIBr₂-Based All-Inorganic Perovskite Solar Cells through a Functional Cu²⁺ Doping Strategy. *ACS Appl. Mater. Interfaces* **2020**, *12* (21), 23984–23994.
- (172) Hu, C.; Bai, Y.; Xiao, S.; Zhang, T.; Meng, X.; Ng, W. K.; Yang, Y.; Wong, K. S.; Chen, H.; Yang, S. Tuning the A-Site Cation Composition of FA Perovskites for Efficient and Stable NiO-Based p-i-n Perovskite Solar Cells. *J. Mater. Chem. A* **2017**, *5* (41), 21858–21865.
- (173) Chen, M.; Guan, R.; Yang, S. Hybrids of Fullerenes and 2D Nanomaterials. *Adv. Sci.* **2019**, *6* (1), 1800941.
- (174) Quillettes, D. W.; Vorpahl, S. M.; Stranks, S. D.; Nagaoka, H.; Eperon, G. E.; Ziffer, M. E.; Snaith, H. J.; Ginger, D. S. Impact of Microstructure on Local Carrier Lifetime in Perovskite Solar Cells. *Science* **2015**, *348*(6235), 683–686.
- (175) Ganesan, K.; Ghosh, S.; Krishna, N. G.; Ilango, S.; Kamruddin, M.; Tyagi, A. K. A Comparative Study on Defect Estimation Using XPS and Raman Spectroscopy in Few Layer Nanographitic Structures. *Phys. Chem. Chem. Phys.* **2016**, *18* (32), 22160–22167.
- (176) Wan, X.; Yu, Z.; Tian, W.; Huang, F.; Jin, S.; Yang, X.; Cheng, Y.-B.; Hagfeldt, A.; Sun, L. Efficient and Stable Planar All-Inorganic Perovskite Solar Cells Based on High-Quality CsPbBr₃ Films with Controllable Morphology. *J. Energy Chem.* **2020**, *46*, 8–15.
- (177) Du, Y.; Xin, C.; Huang, W.; Shi, B.; Ding, Y.; Wei, C.; Zhao, Y.; Li, Y.; Zhang, X. Polymeric Surface Modification of NiO_x-Based Inverted Planar Perovskite Solar Cells with Enhanced Performance. *ACS Sustain. Chem. Eng.* **2018**, *6* (12), 16806–16812.
- (178) Zhao, J. S.; Wang, H. Y.; Yu, M.; Hao, M. Y.; Yuan, S.; Qin, Y.; Fu, L.-M.; Zhang, J.-P.; Ai, X.-C. Charge Carrier Recombination Dynamics in a Bi-Cationic Perovskite Solar Cell. *Phys. Chem. Chem. Phys.* **2019**, *21* (10), 5409–5415.
- (179) Jin, Z.; Guo, Y.; Yuan, S.; Zhao, J. S.; Liang, X. M.; Qin, Y.; Zhang, J. P.; Ai, X. C. Modification of NiO_x Hole Transport Layer for Acceleration of Charge Extraction in Inverted Perovskite Solar Cells. *RSC Adv.* **2020**, *10* (21), 12289–12296.
- (180) Deng, X.; Cao, Z.; Li, C.; Wang, S.; Hao, F. Benzotriazole Derivative Inhibits Nonradiative Recombination and Improves the UV-Stability of Inverted MAPbI₃ Perovskite Solar Cells. *J. Energy Chem.* **2022**, *65*, 592–599.

- (181) Gu, X.; Xiang, W.; Tian, Q.; Liu, S. Rational Surface-Defect Control via Designed Passivation for High-Efficiency Inorganic Perovskite Solar Cells. *Angew. Chemie* **2021**, *133*(43), 23348–23354.
- (182) Zhao, B.; Jin, S. F.; Huang, S.; Liu, N.; Ma, J. Y.; Xue, D. J.; Han, Q.; Ding, J.; Ge, Q. Q.; Feng, Y. Thermodynamically Stable Orthorhombic γ -CsPbI₃ Thin Films for High-Performance Photovoltaics. *J. Am. Chem. Soc.* **2018**, *140* (37), 11716–11725.
- (183) Liu, S. C.; Li, Z.; Yang, Y.; Wang, X.; Chen, Y. X.; Xue, D. J.; Hu, J. S. Investigation of Oxygen Passivation for High-Performance All-Inorganic Perovskite Solar Cells. *J. Am. Chem. Soc.* **2019**, *141* (45), 18075–18082.
- (184) Yi, F.; Guo, Q.; Zheng, D.; Zhuang, R.; Zhang, J.; Tang, Q.; Duan, J. Multifunctional Polymer Capping Frameworks Enable High-Efficiency and Stable All-Inorganic Perovskite Solar Cells. *ACS Appl. Energy Mater.* **2022**, *5* (5), 6432–6441.
- (185) Ullah, S.; Yang, P.; Wang, J.; Liu, L.; Yang, S. E.; Xia, T.; Chen, Y. Low-Temperature Processing of Polyvinylpyrrolidone Modified CsPbI₂Br Perovskite Films for High-Performance Solar Cells. *J. Solid State Chem.* **2022**, *305*, 122656.
- (186) Niu, Y.; He, D.; Zhang, Z.; Zhu, J.; Gavin, T.; Falaras, P.; Hu, L. Improved Crystallinity and Self-Healing Effects in Perovskite Solar Cells via Functional Incorporation of Polyvinylpyrrolidone. *J. Energy Chem.* **2022**, *68*, 12–18.
- (187) Zhang, M.; Wu, F.; Chi, D.; Shi, K.; Huang, S. High-Efficiency Perovskite Solar Cells with Poly (vinylpyrrolidone)-Doped SnO₂ as an Electron Transport Layer. *Mater. Adv.* **2020**, *1* (4), 617–624.
- (188) Han, T. H.; Lee, J. W.; Choi, C.; Tan, S.; Lee, C.; Zhao, Y.; Dai, Z.; De Marco, N.; Lee, S. J.; Bae, S.-H. Perovskite-Polymer Composite Cross-Linker Approach for Highly-Stable and Efficient Perovskite Solar Cells. *Nat. Commun.* **2019**, *10* (1), 520.
- (189) Hwang, I.; Jeong, I.; Lee, J.; Ko, M. J.; Yong, K. Enhancing Stability of Perovskite Solar Cells to Moisture by the Facile Hydrophobic Passivation. *ACS Appl. Mater. Interfaces* **2015**, *7*(31), 17330–17336.